batteries

MDPI

Review

Electro-Chemo-Mechanical Coupling in All-Solid-State Lithium Metal Batteries: From Stress Generation to Failure Mitigation

Qichanghao Li [1,2], Ying Li [1], Zihao Wang [3], Kyu-Young Park [4], Simon Fleischmann [5], Hidemi Kato [2] and Eric Jianfeng Cheng [1,*]

[1] Advanced Institute for Materials Research (AIMR), Tohoku University, Sendai 980-8577, Japan
[2] Institute for Materials Research, Tohoku University, Sendai 980-8577, Japan
[3] Fracture and Reliability Research Institute, Department of Finemechanics, Tohoku University, Sendai 980-8579, Japan
[4] Department of Materials Science and Engineering, Pohang University of Science and Technology (POSTECH), Pohang 37673, Republic of Korea
[5] Helmholtz Institute Ulm (HIU), Karlsruhe Institute of Technology (KIT), 89081 Ulm, Germany
* Correspondence: ericonium@tohoku.ac.jp

Abstract

All-solid-state lithium metal batteries (ASSLMBs) promise enhanced safety and high energy density, yet their solid–solid interfaces create mechanical constraints absent from conventional liquid-electrolyte cells. Electrochemical reactions, ion transport, and interfacial reactions generate lattice strain, volume change, and heterogeneous stress; in turn, stress redistributes ionic and electronic transport, reaction kinetics, and local current density. This bidirectional electro-chemo-mechanical coupling drives particle cracking, interfacial debonding, contact loss, void formation, lithium-filament penetration, and ultimately capacity decay or short circuiting. In this review, we establish a multiscale framework connecting the origins of stress to electrochemical consequences and failure across the crystal, particle, electrode, interface, and cell levels. We critically examine cathode deformation, lithium plating and stripping, stack-pressure evolution, thermal mismatch, and defect-assisted fracture, together with operando imaging, stress sensing, and multiphysics modeling approaches used to resolve these processes. We further assess mitigation strategies based on low-strain electrodes, mechanically compatible composite cathodes, defect-tolerant solid electrolytes, adaptive interphases, regulated stack pressure, and cell architecture. Finally, we identify the need for quantitative failure criteria, multimodal operando characterization, and standardized testing under practical conditions to accelerate durable, high-energy ASSLMBs.

Keywords: all-solid-state lithium metal batteries; electro-chemo-mechanical coupling; solid electrolytes; interfacial degradation; mechanical failure; lithium dendrites; stack pressure

Check for updates

Academic Editor: Chunwen Sun

Received: 18 August 2026
Revised: 14 September 2026
Accepted: 18 September 2026
Published: 3 October 2026

Copyright: © 2026 by the authors. Licensee MDPI, Basel, Switzerland. This article is an open access article distributed under the terms and conditions of the Creative Commons Attribution (CC BY) license.

1. Introduction

The growing demand for electric vehicles, portable electronics, and large-scale energy storage has driven the development of rechargeable batteries with higher energy density, improved safety, and longer service life [1]. Conventional lithium-ion (Li-ion) batteries based on flammable liquid electrolytes have achieved remarkable commercial success, but their further development is increasingly constrained by safety concerns, limited electrochemical stability, and the difficulty of incorporating high-capacity electrodes such as Li metal [2]. All-solid-state lithium metal batteries (ASSLMBs) have therefore attracted

considerable attention as a promising next-generation energy-storage technology. By replacing liquid electrolytes with nonflammable solid electrolytes (SEs), ASSLMBs offer the potential for improved safety and higher energy density, particularly when combined with Li-metal anodes and high-capacity cathodes [3–6].

Despite these advantages, the replacement of a liquid electrolyte with a SE fundamentally changes the mechanical environment inside the battery [7]. In liquid-electrolyte systems, the electrolyte can wet newly formed surfaces and fill interfacial gaps, thereby helping to maintain ionic contact between the electrodes and electrolyte. In contrast, SEs in ASSLMBs cannot readily accommodate the dimensional and morphological changes of electrodes during cycling [8]. Once particle cracking, interfacial debonding, or void formation occurs, local solid–solid contact is difficult to restore [9]. Consequently, stress and deformation arising from electrode volume changes, Li plating and stripping, mechanical mismatch between constituent materials, and external mechanical constraints can continuously alter interfacial contact and transport networks within the cell, becoming critical factors that limit the long-term stability of ASSLMBs [3,10].

More importantly, mechanical behavior in ASSLMBs does not occur independently of electrochemical processes but is dynamically coupled with electrochemical reactions and mass transport [11,12], as shown in Figure 1. On the one hand, ion insertion and extraction, Li plating and stripping, and interfacial reactions induce lattice strain, volume changes, and local stress evolution [13]. On the other hand, the resulting stress, deformation, and fracture can, in turn, redistribute interfacial contact, ionic and electronic transport, local current density, and reaction kinetics, thereby affecting subsequent electrochemical processes [14,15]. This bidirectional feedback spans multiple length scales, from lattice distortion and defect evolution at the atomic scale, through fracture and contact evolution at the particle scale, to structural deformation and pressure evolution at the electrode and cell scales. Understanding such coupled behavior is therefore essential for elucidating performance degradation and failure in ASSLMBs.

Accordingly, the study of ASSLMBs must extend beyond conventional perspectives centered primarily on ionic conductivity, electrochemical stability, and interfacial chemistry by incorporating mechanical properties, interfacial contact, and their evolution during cycling into a unified electrochemical–mechanical framework [16,17]. Recent advances in operando and in situ characterization, three-dimensional (3D) imaging, stress monitoring, and multiscale modeling have provided new opportunities to directly probe structural and stress evolution across multiple length scales [18–20]. Meanwhile, materials modification, interface engineering, electrode microstructure optimization, and cell-level mechanical design have emerged as promising approaches to mitigating electro-chemo–mechanical degradation [21,22]. A systematic understanding of the origin and evolution of stress and its interactions with electrochemical processes is therefore crucial for elucidating failure mechanisms and developing effective strategies to improve the performance and durability of ASSLMBs.

This review focuses on electro-chemo-mechanical coupling in ASSLMBs, with particular emphasis on its mechanical origins and its role in structural degradation, interfacial evolution, and cell failure. Section 2 discusses the major origins of stress, including cathode volume changes, chemo-mechanical mismatch within composite cathodes, Li plating and stripping, external stack pressure, and thermally induced stress. Section 3 examines how stress affects electrochemical behavior at the cathode and anode sides, together with the effects of external loading and coupled interfacial evolution. Section 4 summarizes the principal electro-chemo-mechanical failure mechanisms, including composite-cathode degradation, Li-dendrite growth and penetration through SEs, and contact loss at buried interfaces. Section 5 reviews advanced characterization techniques for resolving structural

evolution, Li deposition, and internal stress across multiple length scales, while Section 6 critically assesses mitigation strategies at the material, interface, electrode, and cell levels, emphasizing both their benefits and the associated trade-offs in ionic transport, mechanical stability, energy density, processing complexity, and practical cell operation. Section 7 discusses emerging AI-assisted approaches for failure prediction, interface optimization, multimodal characterization, and closed-loop electro-chemo-mechanical design. By connecting the origins of stress with their electrochemical consequences, failure mechanisms, characterization approaches, and mitigation strategies, this review aims to provide a unified and critical framework for understanding and mitigating electro-chemo-mechanical failure in ASSLMBs and to guide the rational design of high-performance and durable solid-state batteries.

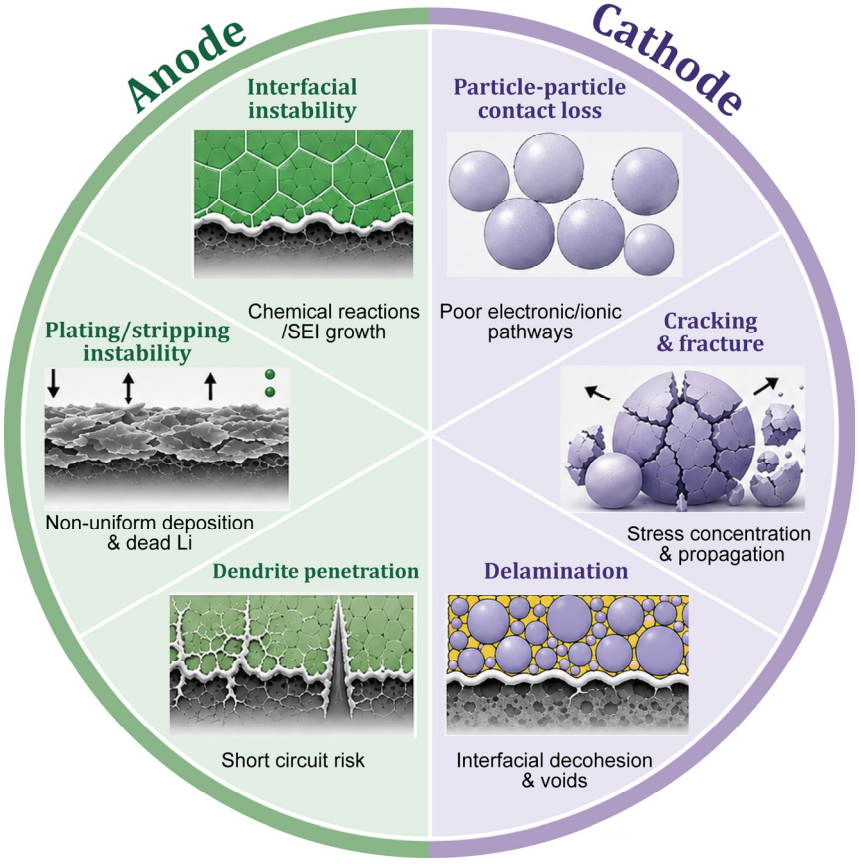


Figure 1. Electro-chemo-mechanical coupling and interfacial failure in ASSLMBs.

2. Origin of Electro-Chemo-Mechanical Coupling in ASSLMBs

Replacing liquid electrolytes with SEs substantially improves the safety of ASSLMBs and offers the potential for higher energy density. However, the relatively high stiffness of SEs restricts the free deformation of electrode materials during cycling. As a result, electrochemically induced volume changes and interfacial evolution are more readily converted into internal stresses. Differences in mechanical properties, microstructure, and thermal expansion among the electrodes, SE, and interfacial phases further contribute to stress generation and accumulation over multiple length scales [23].

Stress in ASSLMBs can arise from several sources—as detailed in Table 1—including the volume changes of cathode materials during lithiation and delithiation, chemo-mechanical mismatch between the cathode material and SE within composite electrodes, local stress evolution during Li plating and stripping, changes in solid–solid contact under external stack pressure, and thermally induced stresses caused by temperature gradients.

These stresses affect interfacial contact, ion transport, and electrochemical reaction kinetics, and may therefore promote defect formation and interfacial failure. Understanding how stresses of different origins develop and evolve is essential for clarifying electro-chemo-mechanical coupling in ASSLMBs and improving their cycling stability.

Table 1. Origins of stress generation in ASSLMBs.

Stress Source	Driving Mechanism	Dominant Scale	Representative Consequences
Cathode volume change	Li insertion/extraction–induced lattice expansion/contraction	Particle	Particle cracking, structural degradation
Composite cathode mismatch	Mechanical-property mismatch among active materials, SE, and additives	Electrode	Interfacial debonding, stress concentration, contact loss
Li plating/stripping	Heterogeneous Li deposition and stripping	Interface	Li filament growth, void formation
Stack pressure	External compressive loading and stress redistribution	Cell	Interfacial contact evolution, creep deformation
Thermally induced stress	Thermal expansion mismatch and temperature gradients	Cell	Thermal cracking, delamination

2.1. Volume Changes of Cathode Materials

During cycling, reversible Li insertion and extraction in cathode materials are accompanied by redox reactions of the transition-metal (TM) ions. These reactions alter the crystal structure and cause the cathode to expand or contract. In comparison, the volume change of a SE caused by Li-ion migration is generally negligible because of its rigid ceramic framework [24,25]. In liquid-electrolyte batteries, electrode deformation can be accommodated to some extent by the fluid electrolyte. In ASSLMBs, however, the rigid constraint imposed by the SE prevents the volume change of the cathode material from being readily released. Instead, it is converted into interfacial stress and localized strain, making cathode volume change one of the most direct mechanical driving forces in the electrode–electrolyte system.

Table 2 summarizes the phase transitions, volume changes, primary sources of stress, and mechanical degradation issues associated with common commercial cathode materials during electrochemical processes. These data highlight the significant differences in electro-chemo-mechanical responses among cathode materials with varying crystal structures. The crystal structure of a cathode material largely determines how its volume evolves during electrochemical cycling [26]. The following section discusses the volume-change mechanisms of several representative intercalation cathodes.

Table 2. Representative cathode materials and their electro-chemo-mechanical characteristics.

Cathode	Structure	Phase Transition	Volume Change by Charging	Dominant Stress Origin	Mechanical Degradation	Ref.
LCO	Layered	H1-H2-H3	+2%	CoO_2 layer contraction	Cracking	[27,28]
NCM111	Layered	H1-M-H2-H3	−3.4%	Moderate anisotropic strain	Cracking	[29,30]
NCM811	Layered	Strong H2-H3	−6%	c-axis contraction	Intergranular fracture	[31,32]
LNO	Layered	Strong H2-H3	−9% (non-monotonic)	Ni-O contraction	Collapse/Cracking	[33,34]
LMO	Spinel	Cubic/Tetragonal	−1.5%	Mn^{3+} distortion	Fracture/Mn dissolution	[35,36]
o-LNMO (ordered)	Spinel	Two-phase/Solid-solution transition	−3%	High-voltage strain	Interface degradation	[37,38]
LFP	Olivine	LFP/FP	−6.8%	Coherency stress	Phase-boundary stress	[39,40]

2.1.1. Layered Structures

$LiNi_xCo_yMn_zO_2$ (NCM) materials are typical layered oxide cathodes with an α-$NaFeO_2$-type O3 structure and the space group (R-3m). They belong to the $LiMO_2$ family of layered TM oxides. At a given upper cutoff voltage, Ni-rich NCM generally enables greater Li utilization and therefore reaches a more deeply delithiated state than lower-Ni compositions. Consequently, $LiNi_{0.8}Mn_{0.1}Co_{0.1}O_2$ (NCM811) undergoes a substantially larger state-of-charge (SOC)-dependent lattice change than $LiNi_{0.33}Mn_{0.33}Co_{0.33}O_2$ (NCM111) under otherwise comparable cycling conditions, which contributes to its more pronounced chemo-mechanical instability [41,42]. Kondrakov et al. [30] systematically compared the structural evolution and mechanical degradation of low-Ni NCM111 and Ni-rich NCM811. In situ X-ray diffraction (XRD) measurements showed that, over the voltage range of 3.0–4.3 V (vs. Li/Li^+), NCM811 exhibited a unit-cell volume change of up to 5.1%, compared with only 1.2% for NCM111 (Figure 2a). The main difference appeared at Li contents below x(Li) < 0.5. In NCM811, the c-axis parameter decreased sharply from 14.467 Å to 14.030 Å. This non-monotonic contraction was mainly attributed to a reduction in the effective negative charge of the oxygen anions, which weakened electrostatic repulsion between adjacent oxygen layers. At the same time, continuous contraction of the a-axis and the TM–O bonds produced a strongly anisotropic lattice response. By contrast, the c-axis parameter of NCM111 reached a maximum near x(Li) = 0.5 and decreased only slightly thereafter. The anisotropic microstrain parameters further showed that NCM811 underwent substantial cyclic strain accumulation during delithiation. Within secondary particles, anisotropic lattice strain, together with spatially heterogeneous delithiation arising from finite Li-ion transport kinetics, can generate heterogeneous internal stress fields. The resulting stress concentrations promote intragranular and intergranular cracking, while the newly exposed surfaces facilitate electrolyte penetration and interfacial side reactions, thereby accelerating structural degradation and capacity fading [43].

Trevisanello et al. [44] used focused ion beam combined with scanning electron microscopy (FIB-SEM) to examine the morphological evolution of polycrystalline NCM particles during the first charge. Once the charging voltage exceeded 3.8 V, serrated microcracks gradually formed along the grain boundaries, indicating pronounced intergranular fracture (Figure 2b). The cracks originated inside the particles and were mainly associated with tensile stresses generated by Li-concentration gradients, together with local stress concentrations caused by the anisotropic lattice changes of differently oriented primary grains. At an early stage, cracking may increase the electrochemically active surface area and shorten Li-diffusion paths, which can improve rate performance. Over prolonged cycling, however, progressive cracking of polycrystalline particles severely compromises structural integrity and cycling stability.

$Li_{1-x}CoO_2$ (LCO) and $Li_{1-x}NiO_2$ (LNO) also show markedly different volume-evolution behavior [33,45,46]. For x < 0.75, the volume of LCO changes almost monotonically during delithiation, whereas LNO undergoes pronounced non-monotonic contraction. Both materials initially show slight expansion along the c-axis because of increased electrostatic repulsion between adjacent layers. Their overall volume responses differ mainly because of the different changes in the in-plane a/b lattice parameters: LCO undergoes only a small in-plane change, whereas LNO contracts substantially. This difference is mainly associated with the Jahn–Teller activity of Ni^{3+}. The orbitally degenerate electronic configuration of Ni^{3+} gives rise to local Jahn–Teller distortions during delithiation. Coupling between these distortions and Li vacancies can gradually produce long-range ordered distortions, resulting in pronounced anisotropic contraction within the NiO_2 layers. This in-plane contraction can exceed the expansion along the c-axis, leading to an overall decrease in cell volume. Co^{3+}, in contrast, does not exhibit a strong Jahn–Teller distortion, and the

structural evolution of LCO is therefore more uniform and stable. In layered cathodes, the mechanical response may also originate from local changes in the stacking sequence rather than solely from changes in the lattice parameters. Slab gliding and stacking transitions can introduce local shear deformation, stacking faults, and lattice incompatibility, which may generate additional stress concentrations and contribute to particle-level mechanical degradation [47,48].

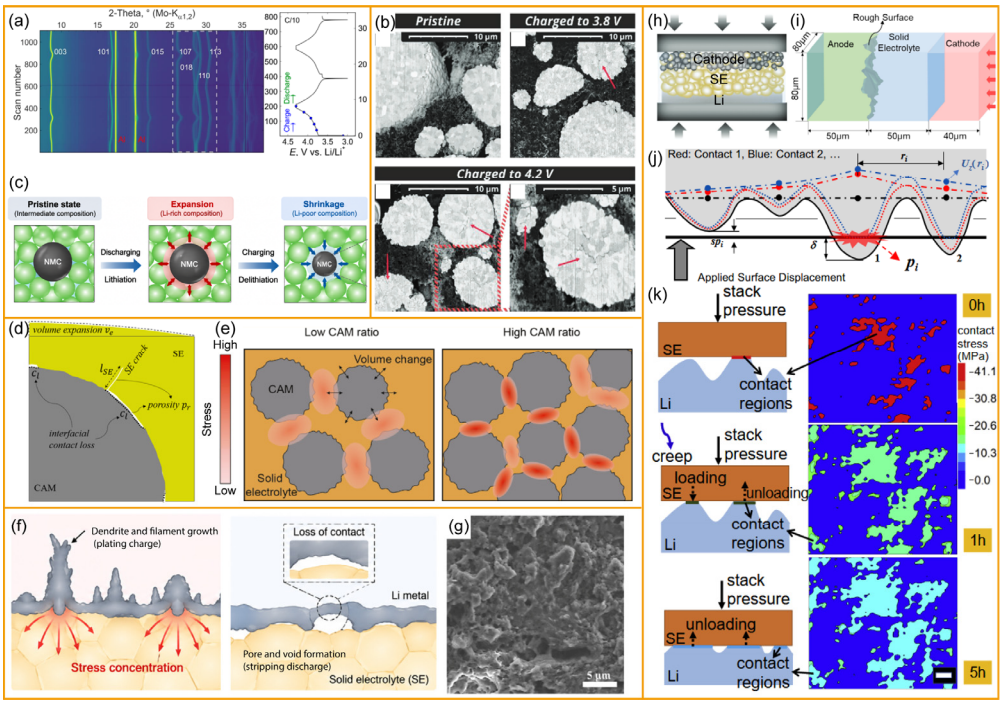


Figure 2. Chemo-mechanical origins of stress evolution in ASSLMBs. (**a**–**c**) Structural evolution and stress generation in cathode materials during lithiation/delithiation, including composition-dependent lattice changes, particle cracking induced by anisotropic deformation, and different stress-evolution pathways associated with cathode volume changes. (**a**) Reproduced with permission from Ref. [30]. Copyright 2017 American Chemical Society. (**b**) Reproduced from Ref. [44] under the terms of the CC BY-NC-ND 4.0 license. Copyright 2021, Wiley-VCH GmbH. (**c**) Adapted from Ref. [49]. Copyright 2023 ASME. (**d**,**e**) Chemo-mechanical interactions within composite cathodes, showing stress development at the cathode/SE interface and the effect of cathode loading on local stress distribution and stress concentration. (**d**) Reproduced with permission from Ref. [50]. Copyright 2023 American Chemical Society. (**e**) Reproduced with permission from Ref. [51]. Copyright 2025 American Chemical Society. (**f**,**g**) Stress evolution associated with Li plating and stripping, including heterogeneous Li deposition, stripping-induced interfacial void formation, and the accumulation of residual strain during repeated cycling. (**g**) Reproduced from Ref. [52] under the CC BY-NC 3.0 license. Copyright 2025, the authors. Published by the Royal Society of Chemistry. (**h**–**k**) Effects of external stack pressure and solid–solid contact mechanics, illustrating pressure-dependent interfacial behavior, the evolution of microscopic contact regions, and Li creep-mediated redistribution of interfacial contact stress. (**h**) Reproduced with permission from Ref. [53]. Copyright 2024 Wiley-VCH GmbH. (**i**) Reproduced with permission from Ref. [54]. Copyright 2025 Elsevier B.V. (**j**) Reproduced from Ref. [55] under the CC BY-NC 4.0 license. Copyright 2025 ASME. (**k**) Reproduced from Ref. [56] under the CC BY-NC-ND license. Copyright 2020, the authors. Published by Elsevier Inc.

2.1.2. Spinel Structures

Spinel cathode materials, such as $LiMn_2O_4$ (LMO) and $LiNi_{0.5}Mn_{1.5}O_4$ (LNMO), exhibit different volume responses during delithiation [57,58]. The volume of LMO changes approximately linearly, whereas Ni-substituted spinels show a more complex nonlinear response because Mn and Ni undergo redox reactions in several successive steps. The ionic

radii therefore change differently at different states of charge, causing the overall lattice response to deviate from simple linear contraction. The volume change is also strongly influenced by the Jahn–Teller distortion associated with Mn^{3+}, rather than being governed solely by changes in ionic radius [59,60]. Ni substitution can suppress the cooperative Jahn–Teller distortion of Mn^{3+}, thereby reducing lattice anisotropy and structural distortion and, consequently, the overall volume change. TM substitution therefore provides an effective means of controlling electronic distortions in spinel structures and limiting the accumulation of volumetric strain. It should also be noted that a relatively modest bulk volume change does not necessarily imply limited mechanical degradation in spinel cathodes. In LMO, Mn dissolution and the accompanying surface reconstruction and irreversible phase evolution can progressively alter the particle morphology and local mechanical environment, thereby coupling chemical degradation with mechanical damage during prolonged cycling [61].

2.1.3. Olivine Structures

Olivine-type phosphate cathodes, such as $LiFePO_4$ (LFP) and related multicomponent compounds, generally undergo relatively gradual and stable volume changes during cycling [62]. The rigid PO_4 tetrahedral framework acts as a structural backbone and remains intact even after complete delithiation. Their volume change therefore arises mainly from contraction of the TM–O bonds upon oxidation of the TM ions. In multi-metal compounds such as $LiFe_{0.5}Mn_{0.5}PO_4$, the stepwise oxidation of Fe and Mn produces stage-dependent lattice contraction [63]. In Mn-containing olivine cathodes, however, oxidation of Mn^{2+} to Jahn–Teller-active Mn^{3+} can introduce pronounced local distortion of the MnO_6 octahedra, producing an additional anisotropic component of the chemical strain beyond the average lattice contraction associated with TM oxidation [64]. The changes in TM–O bond length closely follow the macroscopic volume contraction, indicating that bond contraction is the dominant structural response in these rigid-framework materials.

Overall, the partial molar volume of Li in an intercalation cathode may change continuously during lithiation and delithiation, resulting in different stress-evolution pathways and spatial stress distributions, as illustrated in Figure 2c [49]. The volume response of a cathode material cannot therefore be attributed to a single factor, and changes in ionic radius alone are insufficient to explain its lattice evolution. Instead, the macroscopic volume change is jointly controlled by changes in Coulombic interactions, contraction of TM–O bonds, Jahn–Teller distortions, and the rigidity of the crystal framework. Coulombic interactions are particularly important in flexible-framework materials, whereas TM–O bond contraction dominates the volume response of rigid-framework materials. In compounds containing TM ions with suitable electronic configurations, Jahn–Teller distortions introduce additional anisotropic lattice strain and further modify the local stress distribution. Elemental substitution or doping can modify the electronic structure and suppress cooperative distortions, thereby controlling the volume response, reducing stress concentrations, and improving structural stability.

2.2. Chemo-Mechanical Mismatch Between the Cathode Material and SE in Composite Cathodes

In practical ASSLMBs, the cathode material is usually mixed with approximately 20–50 wt% SE and a certain amount of conductive additive to form continuous ionic and electronic transport pathways. Cathode particles are therefore surrounded by SE particles, conductive carbon, binder, and pores. However, different types of inorganic SEs—including oxides, sulfides, and halides—exhibit markedly different mechanical properties, such as Young's modulus (E) and fracture toughness (K_{Ic}), as summarized in Table 3 [65]. These

intrinsic differences play a critical role in governing stress evolution within the composite cathode as well as the pressure distribution throughout the battery.

Table 3. RT ionic conductivity and mechanical properties of typical inorganic SEs.

Electrolyte	Structure Type	σ-RT ($S \cdot cm^{-1}$)	*E* (GPa)	*G* (GPa)	Poisson's Ratio ν	*H* (GPa)	K_{Ic} ($MPa \cdot m^{1/2}$)	Ref.
$Li_7La_3Zr_2O_{12}$	Garnet	3×10^{-4}	150	60	0.26	6.3	1.25	[66–68]
$Li_{6.4}La_3Zr_{1.4}Ta_{0.6}O_{12}$	Garnet	4.5×10^{-4}	159	63	0.26	11.3	1.51	[69]
$Li_{0.35}La_{0.57}TiO_3$	Perovskite	1×10^{-3}	200	80	0.26	9.2	1	[70–72]
$Li_{1.3}Al_{0.3}Ti_{1.7}(PO_4)_3$	NASICON	1.8×10^{-4}	131	53	0.24	11	1.4	[73]
$Li_{1.5}Al_{0.5}Ge_{1.5}(PO_4)_3$	NASICON	5.0×10^{-4}	141	56	0.25	10.6	0.52	[74]
$75Li_2S–25P_2S_5$	Glass	2.8×10^{-4}	18	7.1	0.30	1.9	0.23	[75–77]
$Li_7P_3S_{11}$	Glass-ceramic	1.7×10^{-2}	21.9	8.1	0.35	–	–	[78,79]
Li_6PS_5Cl	Argyrodite	1.1×10^{-3}	4.7	1.7	0.37	0.9	0.17	[80–82]
$Li_{10}GeP_2S_{12}$	LGPS-type	1.2×10^{-2}	37.2	14.4	0.30	0.5	0.34	[83–86]
Li_3YCl_6	Layered halide	5.1×10^{-4}	38	15	0.27	1.7	–	[87–89]
Li_3InCl_6	Distorted rock-salt	2×10^{-3}	10.5	3.8	0.39	–	–	[90,91]

Note: σ-RT represents the room-temperature (RT) ionic conductivity; *E* represents the Young's modulus; *G* represents the shear modulus; *H* represents the Vickers hardness; K_{Ic} represents the fracture toughness; '–' indicates that it was not specified in the original text.

Within this multiphase microstructure, chemo-mechanical mismatch between the cathode material and SE produces a highly nonuniform stress distribution. This stress distribution can strongly affect stress-dependent reaction kinetics as well as ionic and electronic transport. During cycling, expansion and contraction of the cathode lattice generate substantial mechanical deformation within the composite cathode. This deformation drives pore evolution, loss of interfacial contact, crack formation, and the progressive accumulation of structural defects, eventually leading to electrochemical performance degradation.

Farzanian et al. [50] developed a symmetric two-dimensional (2D) continuum model of a composite cathode at the mesoscale (Figure 2d) and systematically examined how different mechanical properties affect defect evolution. SEs with a low elastic modulus, such as sulfide electrolytes with $E < 20$ GPa, were able to accommodate the volume change of the cathode material and substantially suppress the formation of mechanical defects. In contrast, high-modulus oxide electrolytes, such as $Li_7La_3Zr_2O_{12}$ (LLZO) with E~150 GPa, were more likely to produce severe structural damage.

For a high-modulus electrolyte, however, a relatively low yield strength or ultimate strength may allow plastic flow, which partially accommodates cathode expansion and reduces defect accumulation. The cathode loading and electrochemical state also strongly affect the mechanical evolution of the composite electrode. State of discharge is defined as 100% when the primary NMC particles are discharged to the lithiated state. As the depth of discharge increases, the cathode expands more strongly, leading to greater interfacial contact loss and higher porosity. These defects increase sharply when the depth of discharge exceeds 100%. A high cathode loading above 50 vol% may reduce some forms of contact loss in absolute terms, but it also substantially reduces the ability of the electrolyte phase to accommodate cathode expansion. As a result, the overall electrode expansion can exceed 5%, while the porosity can rise above 1%, further degrading the structural integrity of the composite cathode.

Park et al. [51] investigated the long-term chemo-mechanical behavior of composite cathodes by varying the ratio of NCM811 to Li_6PS_5Cl (LPSC). Although increasing the NCM fraction improves the theoretical energy density, it also restricts ion-transport pathways and lowers cathode utilization, thereby accelerating capacity fading. During prolonged cycling, cathodes with high NCM contents, particularly the 80:20 and 85:15 compositions, exhibited much more severe performance degradation. Synchrotron X-ray tomography (XCT) further

showed that mechanical interactions among cathode particles became stronger at high cathode loadings. At the same time, the lower electrolyte content reduced the ability of the composite electrode to accommodate the volume change of NCM. Microstructure-based mechanical simulations indicated that NCM could undergo a volume change of approximately 10% during discharge, generating substantial internal stresses. Cathodes with higher NCM contents showed both larger stress magnitudes and more pronounced stress concentrations (Figure 2e). For example, the fraction of the 85:15 cathode subjected to stresses above 2 GPa was much larger than that of the 70:30 cathode. This increase was attributed to the greater volume expansion of the cathode material, the lower fraction of the mechanically compliant electrolyte phase, and stronger mechanical constraint between neighboring cathode particles.

Overall, chemo-mechanical interactions between the cathode material and SE are a major factor governing the long-term stability of composite cathodes. Increasing cathode loading is beneficial for energy density, but it also promotes stress accumulation and structural degradation. The resulting cracking, debonding, and reaction heterogeneity contribute directly to capacity fading. To achieve both high energy density and long-term stability, the composite cathode must provide efficient ionic and electronic transport while also incorporating compliant phases or mechanically supportive structures that can relieve local stress concentrations and preserve structural integrity.

2.3. Stress Accumulation During Li Plating and Stripping

Unlike intercalation electrodes, where electrochemical strain originates primarily from lattice expansion and contraction, Li-metal anodes undergo direct mass addition and removal at a mechanically constrained solid–solid interface. Spatial variations in current density, ionic transport, surface morphology, and interfacial contact therefore cause Li plating and stripping to proceed nonuniformly. During plating, preferential Li accumulation at localized active sites produces heterogeneous interfacial displacement and compressive stress. During stripping, insufficient Li replenishment and vacancy accumulation promote void formation, contact loss, and stress redistribution at the remaining contact regions. Repeated plating and stripping can consequently generate irreversible interfacial deformation and residual stress, making the Li/SE interface an important source of localized mechanical loading in ASSLMBs.

From this stress-generation perspective, protruding Li deposits and stripping-induced voids should be regarded as mechanically coupled consequences of nonuniform interfacial mass transfer. Their subsequent effects on local current density and electrochemical kinetics are discussed in Section 3.2, whereas the evolution of these instabilities into Li-filament penetration and short-circuit failure is examined in detail in Section 4.2.

This coupled plating–stripping instability is schematically summarized in Figure 2f. During plating, localized Li accumulation generates interfacial deformation and compressive stress, whereas stripping-induced void formation redistributes the applied load and concentrates current at the remaining contact points [10]. During charging, current focusing can promote the growth of Li dendrites or filaments, which may eventually penetrate the SE and cause an internal short circuit. During discharge, the formation of pores and interfacial voids reduces the contact area and increases the interfacial resistance (R_{int}). The remaining contact regions then carry a higher local current density during subsequent plating, which can further promote dendrite growth. Dendrite formation during plating and void formation during stripping therefore represent two closely related sources of stress accumulation and interfacial instability. Together, they provide the basis for understanding the progressive degradation of the Li–SE interface during repeated cycling.

Zhang et al. [52] used embedded strain sensors to monitor the micromechanical evolution of Li plating and stripping in ASSLMBs in real time. This approach also enabled cell failure to be predicted and mitigated. By comparing the voltage, Coulombic efficiency, and strain responses, they identified three characteristic stages of strain evolution: an initial linear-growth stage, an intermediate steady stage, and an exponential-growth stage immediately before failure. The scanning electron microscopy (SEM) morphology of the Cu foil after 30 Li plating/stripping cycles is shown in Figure 2g. Li plating produced substantial microstrain, whereas stripping released only part of the accumulated stress. Residual strain therefore built up progressively over repeated cycles. Increasing the initial stack pressure from 200 to 3500 kPa shortened the initial strain-growth stage by approximately 50%, reduced the average strain during the steady stage by 47.4%, and substantially extended the cycling life. By contrast, increasing the current density from 0.1 to 0.2 $mA \cdot cm^{-2}$ extended the initial linear-growth stage by approximately a factor of ten and increased the strain in the steady stage by about fourfold, thereby accelerating cell failure.

In addition to Li-metal anodes, high-capacity anode materials such as Si may be used to further increase the energy density of ASSLMBs [92,93]. However, these materials undergo much larger volume expansion and contraction during cycling. Their use may therefore introduce even greater stress accumulation and intensify the mechanical degradation already associated with the anode side of solid-state cells.

Overall, Li plating and stripping generate a dynamically evolving stress field through localized mass accumulation, void formation, contact loss, and incomplete stress relaxation. These mechanically heterogeneous conditions do not merely result from electrochemical operation; they subsequently redistribute current and reaction kinetics at the Li/SE interface. This reverse influence of stress on anode electrochemistry is discussed in Section 3.2.

2.4. External Stack Pressure and Nonuniform Solid–Solid Contact

In ASSLMBs, stack pressure is not only required to maintain the integrity of the multilayer cell structure but also serves as an important mechanical parameter controlling ion transport and interfacial stability. Its 2D and 3D representations are shown in Figure 2h [53] and Figure 2i [54], respectively. An appropriate stack pressure increases the effective solid–solid contact area and reduces interfacial contact resistance [94]. Excessive or spatially nonuniform pressure, however, can cause substantial elastic–plastic deformation and local stress concentration. These effects may promote nonuniform Li deposition, increase the likelihood of dendrite penetration, and ultimately lead to internal short circuiting. The pressure distribution also changes continuously during cycling because of electrode volume changes and material creep. The initially applied pressure therefore does not remain uniform, and solid–solid contact should be regarded as a dynamically evolving condition rather than a fixed interfacial state.

Ahmad et al. [55] emphasized that the performance and stability of ASSLMBs depend strongly on the mechanical contact state of the solid–solid interface. The evolution of interacting asperities at a rough interface is illustrated in Figure 2j. Contact-mechanics models showed that the real contact area during Li stripping depends on both the current density and the applied stack pressure. A higher stack pressure promotes material creep and helps maintain continuous interfacial contact, thereby suppressing the nucleation and growth of voids. Loss of interfacial contact can also appear in electrochemical impedance spectroscopy (EIS) as an additional constriction-related semicircle. The diameter of this semicircle increases as the real contact area decreases and can therefore serve as a diagnostic signature of interfacial degradation. Poor contact between the electrode and SE reduces the effective area available for charge transfer, increases the interfacial impedance, and eventually degrades cell performance.

Zhang et al. [56] further showed that Li metal undergoes substantial creep even at RT. Creep gradually improves the conformal contact between Li and the SE and makes the interfacial contact stress more uniform, thereby reducing the R_{int}. The evolution of the Li–SE interface under creep is illustrated in Figure 2k. Comparison of contact and non-contact regions under different pressures showed that a higher stack pressure strongly enhances Li creep and stabilizes the interface. During stripping, particularly at high current densities, the vacancies left behind by Li removal can accumulate and develop into voids. These voids progressively reduce the effective contact area and destabilize the interface. An appropriate stack pressure can partially suppress void formation and growth and help preserve interfacial continuity. During plating, Li deposits preferentially at existing contact points. At low current densities, creep dominates the interfacial evolution. Newly deposited Li can be rapidly redistributed and flattened, increasing the real contact area. At current densities above 0.005 $mA \cdot cm^{-2}$, however, the deposition rate exceeds the rate of creep relaxation. Li then tends to grow into columnar or otherwise nonuniform structures, increasing interfacial gaps and potentially promoting dendrite formation.

Liu et al. [95] systematically investigated the relationships among external pressure of 0.1, 1, and 10 MPa, SEI structure, and Li deposition morphology. At a low pressure of 0.1 MPa, an organic-rich solid electrolyte interphase (SEI) formed, and Li deposited as highly nonuniform filaments with considerable porosity, resulting in poor electrochemical stability. At an intermediate pressure of 1 MPa, the SEI became more uniform and was enriched in inorganic fluorine-containing species such as LiF. Li deposition was correspondingly denser and more uniform, although local inhomogeneity still appeared at high current densities. At 10 MPa, the Li deposits were the densest and most uniform, and the SEI contained a high fraction of inorganic LiF. However, the excessive pressure mechanically damaged the polyolefin separator and caused internal short circuiting, limiting the practical value of such a high pressure.

When a nearly defect-free pristine graphene seed layer was introduced onto the Cu current collector (CC), deposition behavior similar to that obtained at high pressure could be achieved at only 1 MPa. The pristine graphene was proposed to preferentially adsorb and decompose PF_6^- anions, promoting the formation of an inorganic-rich, particularly LiF-rich, SEI while suppressing side reactions involving organic solvents such as ethylene carbonate (EC) and diethyl carbonate (DEC). Although this study was conducted in an anode-free liquid-electrolyte cell, it illustrates how external pressure can alter interfacial chemistry and deposition morphology. These findings may therefore provide useful guidance for the design of interfaces in ASSLMBs, although their direct applicability to solid–solid interfaces should be interpreted with caution.

2.5. Thermally Induced Stress

In addition to electrochemically induced volume change and external stack pressure, heat generation during battery operation represents another important source of mechanical stress in ASSLMBs [96]. Owing to the relatively low ionic conductivity of SEs, imperfect solid-solid interfacial contact, and interfacial polarization, Joule heating inevitably occurs during charge and discharge [97]. Furthermore, parasitic reactions at the electrode/SE interfaces, lithium plating and stripping, as well as electrolyte decomposition under high-voltage operation continuously release heat, resulting in local temperature gradients throughout the cell [98]. Since most of these electrochemical and chemical reactions follow Arrhenius kinetics, elevated temperatures further accelerate reaction rates, giving rise to additional heat generation and localized thermal accumulation [99].

The generated heat is readily converted into mechanical stress because different battery components possess distinct coefficients of thermal expansion (CTEs) [100,101]. In

composite cathodes, active materials, SSE particles, conductive additives, and polymeric binders exhibit substantially different thermal expansion behaviors. Similarly, large CTE mismatches exist among lithium metal, inorganic SSEs, and CCs. When the temperature changes during cycling or local heat accumulation, these components undergo incompatible thermal deformation, resulting in interfacial stress concentration. For two constrained materials with CTE mismatches, the thermal stress evolving as a consequence can be approximately expressed as

$$\sigma_{th} = \frac{E \cdot \Delta\alpha \cdot \Delta T}{1 - \nu} \quad (1)$$

where E is the Young's modulus, $\Delta\alpha$ is the CTE-mismatch, ΔT is the temperature variation, and ν is Poisson's ratio. This relationship indicates that thermal stress increases with both the elastic modulus and thermal expansion mismatch. Consequently, high-modulus inorganic SSEs, such as oxide electrolytes, are generally more susceptible to thermal stress accumulation than compliant polymer electrolytes because their limited deformability restricts stress relaxation [102].

Thermally induced stress can significantly influence the mechanical integrity of ASSLMBs. The accumulation of thermal stress promotes particle fracture, electrolyte cracking, and interfacial debonding, thereby reducing the effective contact area and increasing interfacial resistance [103,104]. The resulting increase in cell impedance further enhances Joule heating, establishing a positive feedback loop of heat generation–thermal stress–interfacial degradation–impedance growth–additional heat generation. Under severe conditions, lithium dendrite-induced internal short circuits or exothermic reactions between charged cathodes and SEs can rapidly elevate the local temperature, producing transient thermal stresses that accelerate crack propagation and catastrophic mechanical failure [105–107]. Therefore, thermal stress not only constitutes an important source of mechanical loading in ASSLMBs but also provides a critical link between thermal effects and electro-chemo-mechanical degradation.

From a mechanical perspective, thermally induced stress is expected to become increasingly important as ASSLMBs evolve toward higher energy density and thicker electrodes. The combination of large temperature gradients, high-modulus inorganic electrolytes, and mechanically constrained solid-solid interfaces makes thermal stress an unavoidable factor governing interfacial stability and long-term structural reliability.

3. Effects of Stress on Electrochemical Behavior in ASSLMBs

Having discussed the major sources of stress in ASSLMBs, this section focuses on how stress affects electrochemical processes within the cell. Because SEs impose strong mechanical constraints, stresses generated during cycling cannot be readily released. Instead, they alter the structural stability of the electrodes, the state of interfacial contact, and ion-transport behavior. The mutual interaction between mechanical stress and electrochemical reactions gives rise to pronounced electro-chemo-mechanical coupling, which plays a central role in determining the cycling stability and failure behavior of ASSLMBs.

3.1. Effects of Cathode-Side Stress on Electrochemical Behavior

On the cathode side, stress affects electrochemical behavior not only by altering interfacial contact but also by changing the structural integrity of cathode particles and the available Li-ion transport pathways. Particle size, morphology, and the mechanical evolution of the cathode during cycling can therefore have a major influence on Li-ion diffusion and electrode reaction kinetics.

The size and geometry of cathode particles strongly influence Li-ion diffusion and the corresponding impedance response. According to the finite-space diffusion model, the characteristic time constant of lithium diffusion is determined by

$$\tau_{Li} = \frac{{L_{Li}}^2}{\widetilde{D}_{\mathrm{Li}}} \tag{2}$$

where L_{Li} is the characteristic Li-ion diffusion length and $\widetilde{D}_{\mathrm{Li}}$ is the chemical diffusion coefficient of Li. This relationship indicates that the diffusion time increases quadratically with the diffusion length. Consequently, chemo-mechanical degradation, including particle cracking and loss of contact with the SE, has the potential to drastically increase the Li-ion diffusion pathway and thus slow lithiation/delithiation kinetics.

Conforto et al. [108] showed that the development of Li-concentration gradients in NCM particles depends on the particle boundary conditions and the available diffusion paths, leading to distinct diffusion-impedance characteristics, as illustrated in Figure 3a. Within the finite-space diffusion framework, the overall low-frequency impedance can be modeled as the parallel contribution of particle populations with different diffusion lengths,

$$Z_{\mathrm{diff}} = \left(\sum_i \frac{N_i}{Z_{fs,i}} \right)^{-1} \tag{3}$$

where Z_{diff} is the overall finite-space diffusion impedance of the composite cathode, $Z_{fs,i}$ is the finite-space diffusion impedance associated with the i-th particle population having the same particle size and geometry, and N_i is the corresponding number of particles in that population. The summation accounts for the parallel contributions of particle populations with different characteristic diffusion lengths and geometries. Within this model, variations in particle size, geometry, and diffusion length can lead to distinct low-frequency impedance responses, with broader particle-size distributions generally giving rise to more complex diffusion features. Therefore, when interpreted using an appropriate finite-space diffusion model and suitable assumptions regarding particle geometry and boundary conditions, the low-frequency impedance response may provide indirect information about the distribution of characteristic Li-ion diffusion lengths and finite-length diffusion effects in the cathode. However, the particle-size distribution cannot generally be determined directly from the impedance spectrum alone and requires model-based analysis, preferably supported by independent structural or morphological characterization.

In ASSLMBs, single-crystalline NCM (SC-NCM) also shows a higher initial capacity and better cycling stability than polycrystalline NCM (PC-NCM), retaining approximately 91% of its capacity after 100 cycles, as shown in Figure 3b. Since only regions satisfying $t_{charge} \geq \tau_i$ can be fully lithiated or delithiated during a finite charging/discharging time, the increase in diffusion length caused by chemo-mechanical degradation progressively reduces the electrochemically accessible active material. In PC-NCM, stress generated by repeated volume changes can progressively weaken contact between the particles and the electronic-conduction network, contributing directly to capacity loss. After cycling, the median Li-ion diffusion-path length in PC-NCM increases to three to four times its initial value, whereas the increase in SC-NCM remains below a factor of two. This difference indicates that cracking within polycrystalline particles, together with the loss of contact with the SE, substantially lengthens Li-ion transport pathways and limits the overall electrode kinetics.

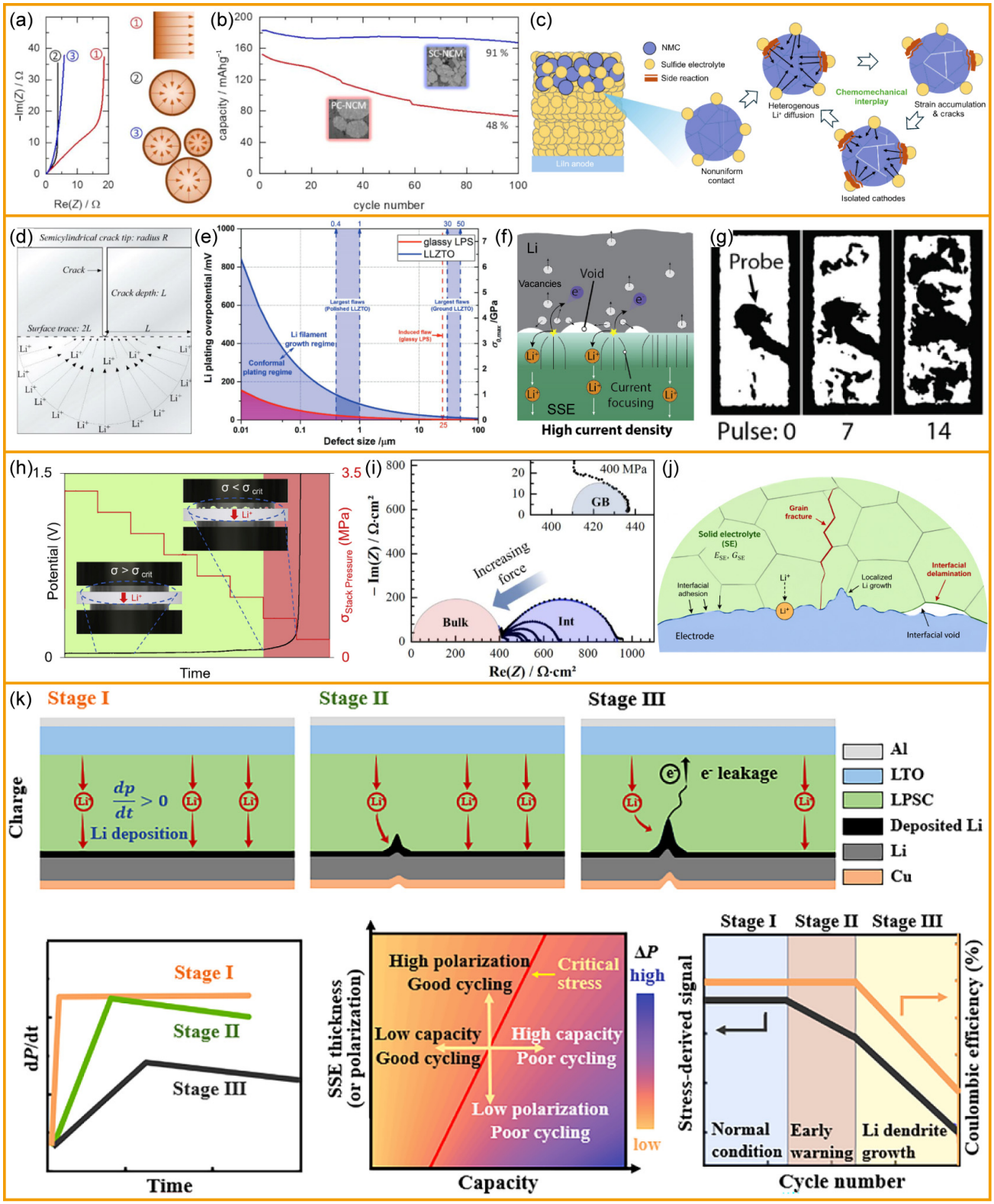


Figure 3. Effects of stress on electrochemical behavior in ASSLMBs. (**a**–**c**) Cathode-side electro-chemo-mechanical effects, including particle-size-dependent Li-ion diffusion and impedance response, differences in cycling stability and Li-ion diffusion pathways between single-crystalline and poly-crystalline NCM, and the coupling among particle cracking, reaction heterogeneity, and loss of ionic contact in composite cathodes. (**a**,**b**) Reproduced from Ref. [108] under the CC BY 4.0 license. Copyright 2021, the authors. Published by IOP Publishing on behalf of The Electrochemical Society. (**c**) Reproduced from Ref. [109] under the CC BY 4.0 license. Copyright 2025, the authors. (**d**–**g**) Stress-mediated Li plating and stripping at the Li/SE interface, showing stress concentration near

Li-filled defects, the dependence of crack propagation on defect size and deposition overpotential, vacancy accumulation and void formation during stripping, and the resulting current focusing at the remaining contact regions. (**d**) Reproduced from Ref. [110] under the CC BY 4.0 license. Copyright 2024, the authors. Published by Elsevier B.V. (**e**) Reproduced with permission from Ref. [111]. Copyright 2017 Wiley-VCH GmbH. (**f**,**g**) Reproduced from Ref. [112] under the CC BY-NC-ND 4.0 license. Copyright 2020, the authors. Published by Elsevier Inc. (**h**,**i**) Effects of external mechanical loading on Li/SE interfacial behavior, illustrating the pressure-dependent transition between unstable and stable cycling and the reduction in interfacial resistance with increasing mechanical load through improved solid–solid contact. (**h**) Reproduced with permission from Ref. [113]. Copyright 2019 Elsevier Inc. (**i**) Reproduced with permission from Ref. [114]. Copyright 2019 American Chemical Society. (**j**,**k**) Interfacial evolution under electro-chemo-mechanical coupling, highlighting the roles of mechanical properties, fracture resistance, and interfacial adhesion in governing contact stability, together with the multistage evolution from relatively uniform Li deposition to stress accumulation, void formation, localized Li growth, and eventual cell failure. (**j**) Adapted from Ref. [7]. Copyright 2019 Springer Nature Limited. (**k**) Reproduced with permission from Ref. [115]. Copyright 2024 Elsevier B.V.

To further clarify the coupling among electrochemical, chemical, and mechanical processes during cathode degradation, Zheng et al. [109] systematically investigated NMC811 cathodes, as illustrated in Figure 3c. Because the SE contacts the cathode particles mainly through discrete contact points, Li-ion transport pathways are limited and spatially nonuniform. During cycling, the anisotropic expansion and contraction of the cathode particles generate mechanical stresses that can initiate cracks within the particles. This process differs fundamentally from that in liquid-electrolyte batteries. In a liquid cell, the electrolyte can penetrate newly formed cracks and establish additional ionic pathways. SE, however, cannot readily fill these new interfaces. As a result, parts of the cathode gradually become isolated from the ionic network and no longer participate effectively in the electrochemical reaction, leading to a loss of accessible capacity. Cracks and electrochemically isolated regions also produce an increasingly nonuniform SOC distribution within the particles. The resulting reaction heterogeneity intensifies local stress concentrations and promotes further crack growth. This creates a positive feedback loop in which cracking impedes Li-ion transport, transport limitations increase local stress, and the accumulated stress drives additional cracking. Such electro-chemo-mechanical coupling ultimately accelerates capacity fading and the growth of R_{int} in ASSLMBs.

3.2. Effects of Anode-Side Stress on Electrochemical Behavior

Section 2.3 identified nonuniform Li plating and stripping as an important source of localized stress at the Li/SE interface. The resulting stress field, however, is not merely a mechanical consequence of electrochemical cycling. It can modify the electrochemical potential of Li and thereby affect several coupled processes at the anode interface, including Li^+ transport through the SE, interfacial charge transfer, and Li^0 redistribution within the metallic Li phase. Stress-induced changes in interfacial contact can further redistribute the local current density and deposition/stripping overpotential. Anode-side stress therefore feeds back into Li-plating and stripping kinetics, determining whether the interface remains morphologically stable or evolves toward localized deposition, Li penetration, and void growth.

This section focuses on this reverse coupling from mechanics to electrochemistry. Particular attention is given to three interconnected effects: stress-assisted transport and accumulation of metallic Li within pre-existing defects, current focusing associated with heterogeneous interfacial contact, and the competition between vacancy accumulation and Li redistribution in the Li metal during stripping. In the following discussion, Li^+ transport

refers specifically to ionic transport through the SE, whereas Li^0 transport or redistribution refers to the motion of neutral Li atoms within the metallic phase.

A direct manifestation of this mechanical feedback is the stress-assisted redistribution of Li^0 near interfacial defects. Richman et al. [116] established a theoretical framework in which the propagation of a Li-filled crack is governed by the total Li atomic flux arising from capillary, electrochemical, and stress-driven contributions. High local stresses develop near the tip of a Li filament and decrease gradually along its length, indicating that Li penetration is strongly influenced by mechanical forces, as shown in Figure 3d [110]. Richman proposed that the crack-propagation rate is related to the total Li atomic flux at the crack tip,

$$v_{crack} = -\Omega \cdot J_T,\ J_T = J_\gamma + J_E + J_\sigma \quad (4)$$

where v_{crack} is the crack-propagation velocity ($m \cdot s^{-1}$), Ω is the atomic volume of Li ($m^3 \cdot atom^{-1}$), and J_T is the total Li atomic number flux ($atom \cdot m^{-2} \cdot s^{-1}$). J_γ, J_E, and J_σ denote the contributions to the atomic flux driven by capillarity, the electrochemical driving force, and mechanical stress, respectively, and therefore have the same units as J_T. This formulation demonstrates that crack propagation is governed by the combined effects of electrochemical deposition, surface energy, and mechanical stress, rather than by electrochemical kinetics alone.

Interfacial defects further increase the local resistance and raise the deposition overpotential, promoting localized Li deposition and stress accumulation around the defect. Importantly, crack growth does not necessarily require the Griffith criterion to be satisfied from the outset. Stress-assisted Li transport and progressive Li accumulation within a pre-existing defect can drive stable or subcritical defect growth under electrochemical cycling. As the defect extends and the local stress intensity increases, the mechanical driving force for fracture progressively approaches the critical condition. Once the energy release rate (G) reaches the critical fracture energy (G_c) or equivalently the stress intensity factor (K_I) reaches the K_{Ic} under linear-elastic fracture mechanics, the crack can transition to unstable propagation, potentially forming a continuous pathway for rapid Li penetration through the SE. Thus, the Griffith criterion should be regarded as defining the critical condition for unstable crack propagation rather than the onset of all crack growth. The influence of external mechanical loading on crack propagation, together with experimental observations that the critical current density depends on the mechanical properties of Li metal, further supports the important role of fracture mechanics in Li penetration.

Building on this framework, Porz et al. [111] quantitatively related the electrochemical deposition overpotential to the mechanical pressure generated inside a Li-filled defect. Their analysis clarifies how an electrochemical driving force can be converted into a local mechanical driving force for defect opening and propagation. Their results showed that penetration generally depends on pre-existing defects, such as surface cracks, pores, and grain boundaries, and occurs only above a critical current density. On a defect-free glassy Li_2S-P_2S_5 (LPS) surface, Li deposits predominantly along the surface, whereas at pre-existing cracks it preferentially fills the defects and promotes their opening. In polycrystalline SEs, Li tends to propagate along pores and grain boundaries to form interconnected penetration pathways. Repeated plating and stripping further accelerate the formation of these Li networks, indicating that cyclic mechanical disturbance progressively damages the interface and facilitates Li penetration.

To quantitatively relate electrochemical driving force to the local mechanical stress, Porz et al. showed that the maximum hydrostatic stress generated within a Li-filled defect is determined by the deposition overpotential,

$$\sigma_{0,\max} \approx -\frac{F\Delta\Phi}{V_m^{\mathrm{Li}}} \tag{5}$$

where F is the Faraday constant, $\Delta\Phi$ is the Li deposition overpotential, and V_m^{Li} is the molar volume of Li. Even a relatively small overpotential of approximately 10 mV can generate stresses approaching 75 MPa, providing a substantial mechanical driving force for the opening and growth of pre-existing defects in brittle SEs.

Whether a Li-filled defect subsequently undergoes unstable propagation depends not only on the deposition-induced stress but also on the defect size and the fracture resistance of the SE, as illustrated in Figure 3e [111]. Within a linear-elastic fracture-mechanics description, unstable crack propagation becomes possible when the Mode-I stress intensity factor reaches the K_{Ic},

$$K_I = \gamma\sigma\sqrt{\pi a} \geq K_{\mathrm{Ic}} \tag{6}$$

where a is the characteristic defect size, γ is a dimensionless geometric correction factor, σ is the stress acting to open the defect, and K_{Ic} is the Mode-I fracture toughness of the SE. For a given K_{Ic}, larger defects therefore require a lower critical stress, and consequently a lower deposition overpotential, to reach the instability threshold. Compared with glassy LPS, $Li_6La_3ZrTaO_{12}$ (LLZTO) possesses a substantially higher K_{Ic} and therefore requires a greater mechanical driving force to reach the critical condition for unstable crack propagation. These results demonstrate that interfacial defects play a central role in Li penetration and short-circuit failure. Progressive Li filling and defect growth can occur before the fracture threshold is reached; once the critical fracture condition is attained, however, rapid unstable propagation of a Li-filled crack can provide a pathway for Li penetration through the SE and ultimately lead to internal short circuiting.

Whereas stress-assisted deposition dominates the charging process, stripping instability is governed primarily by the coupling among vacancy transport, contact loss, and current redistribution. Kazyak et al. [112] investigated void formation at the Li-metal/SE interface under deep-discharge conditions, as shown in Figure 3f. Operando optical images of the coupled electrochemical and morphological evolution are presented in Figure 3g, where the white regions correspond to Li-metal. At low current densities, diffusion of Li vacancies within the Li metal can remain in dynamic balance with the transport of Li-ion into the SE, allowing the interface to remain stable. During high-rate stripping, however, the effective contact area gradually decreases while the total current remains constant. The local current density at the remaining contact points therefore continues to increase. When vacancy diffusion in the Li metal can no longer compensate for Li removal at the interface, vacancies accumulate near the interface and coalesce into voids. These voids further reduce the effective contact area and force the current to concentrate at the remaining contact points, creating a positive feedback loop that accelerates void growth. This interfacial degradation not only promotes failure of the Li-metal anode but also substantially increases R_{int}, making it a major limitation on the high-rate performance of ASSLMBs.

Overall, anode-side stress alters electrochemical behavior through two complementary pathways. During plating, stress and deposition overpotential promote Li transport into defects and intensify localized deposition. During stripping, stress relaxation and void formation reduce the real contact area, causing current focusing and increased polarization. These feedback processes establish the electrochemical and mechanical conditions required for progressive Li-filament growth. Section 4.2 examines how they develop into physically observable crack propagation, electrolyte penetration, and short-circuit failure.

3.3. Effects of External Stress on Electrochemical Behavior

Externally applied mechanical stress, particularly stack pressure, strongly affects interfacial contact, ion transport, and electrochemical performance in ASSLMBs. Wang et al. [113] systematically investigated the effects of stack pressure and current density on the dynamics of the Li-metal/LLZO interface. Their work identified a pressure-dependent mechanism for stabilizing the interface and provided important guidance for the mechanical design of ASSLMBs. To quantitatively describe the competition between Li stripping and pressure-driven Li replenishment, the current-induced-strain rate of the Li electrode $\dot{\varepsilon}_j$ was expressed as

$$\dot{\varepsilon}_j = \frac{jM}{\rho F l_0} \tag{7}$$

where j is the applied current density, M is the molar mass of Li, ρ is the density of Li, F is the Faraday constant, and l_0 is the Li thickness. This relationship shows that increasing the current density accelerates Li depletion at the stripping interface and therefore increases the deformation rate that must be compensated by Li transport.

Under galvanostatic cycling, a critical stack pressure was found to exist for a given current density. When the applied pressure was below this critical value, the battery showed pronounced polarization and a rapid increase in voltage. Once the pressure exceeded the critical value, polarization decreased substantially and stable cycling could be maintained, as shown in Figure 3h. Using a three-electrode configuration with a Ni reference electrode, the authors further confirmed that the polarization originated mainly from contact loss caused by void formation on the Li-stripping side, rather than from morphological changes on the plating side.

At low stack pressure, the rate of Li removal from the interface exceeded the rate at which pressure-driven Li creep could restore contact. The creep deformation of Li can be described by a power-law relation,

$$\dot{\varepsilon}_{creep} = A\sigma^m \exp\left(-\frac{Q}{RT}\right) \tag{8}$$

where A is a material constant, σ is the applied stress, m is the creep exponent, Q is the activation energy, R is the gas constant, and T is the absolute temperature. Based on the competition between these two deformation processes, Wang et al. proposed that unstable void formation occurs when

$$\dot{\varepsilon}_j > \dot{\varepsilon}_{creep} \tag{9}$$

indicating that Li is stripped faster than it can be replenished through pressure-driven creep. Under this condition, voids progressively develop at the stripping interface, reducing the effective contact area and increasing the R_{int}, which ultimately results in severe polarization. Increasing the external pressure enhances Li creep, allowing continuous interfacial contact to be maintained and suppressing void formation. The critical stack pressure is therefore not an intrinsic material constant but is determined by the dynamic balance between the electrochemically induced stripping rate and the mechanically driven creep rate of Li metal.

Krauskopf et al. [114] further examined the influence of external mechanical loading on the interfacial kinetics and morphological stability of Li in contact with garnet-type LLZO, as shown in Figure 3i. The R_{int} decreased sharply as the applied load increased. After isostatic pressing at 400 MPa, the R_{int} approached zero and reached one of the lowest values reported for a Li/LLZO interface without an intermediate interlayer. This behavior

was explained mainly in terms of constriction resistance. Based on the theory of electrical contact resistance, the interfacial resistance can be expressed as

$$R_{int} = \frac{1}{2\sigma_{Li^+}}\sqrt{\frac{\pi H_{Li}}{F}} \quad (10)$$

where σ_{Li^+} is the ionic conductivity of LLZO, H_{Li} is the hardness of Li metal, and F is the externally applied force. Accordingly, interfacial resistance follows an approximate scaling relation of $R_{int} \propto F^{-1/2}$, indicating that increasing the external pressure enlarges the real contact area through plastic deformation of Li and effectively suppresses current constriction at discrete contact spots. According to this interpretation, the interfacial impedance originates primarily from current convergence at the limited microscopic contact points between Li metal and LLZO, rather than from the intrinsic charge-transfer reaction itself. Furthermore, temperature-dependent measurements showed that the apparent activation energy of the interfacial process was close to that of Li-ion transport through bulk LLZO. This finding further suggests that the rate-limiting process is mainly ion transport within the SE, rather than charge transfer across the interface.

Overall, external pressure affects the interfacial kinetics of ASSLMBs by controlling solid–solid contact and the creep behavior of Li metal. Excessively high stack pressure, however, complicates cell and module design and may introduce additional mechanical risks. Reducing the dependence on large external pressures will therefore require alternative approaches, such as moderately increasing the operating temperature to promote Li creep, introducing interfacial coatings to improve Li transport along the interface, or modifying the metallurgy and microstructure of Li metal to enhance its creep response.

3.4. Interfacial Evolution Under Electro-Chemo-Mechanical Coupling

A complete understanding of interfacial evolution and failure in ASSLMBs requires simultaneous consideration of electrochemical reactions, interfacial chemistry, and mechanical deformation. These processes are strongly coupled and cannot be treated independently.

Famprikis et al. [7] discussed how the mechanical properties of SEs and electrode materials affect stress development and interfacial stability across microscopic and mesoscopic length scales, as illustrated in Figure 3j. During cycling, lithiation and delithiation generate periodic electrochemical strains within the electrode materials. Because these strains are constrained by the surrounding SE, they cannot be fully accommodated and instead produce local stress accumulation. The resulting stresses can drive crack propagation, interfacial debonding, and the loss of contact between neighboring particles. The mechanical properties of the SE are therefore critical to long-term interfacial stability. K_{Ic} is an important measure of resistance to crack initiation and propagation. Dense oxide electrolytes generally possess relatively high mechanical strength and K_{Ic}. Some sulfide electrolytes, although softer and better able to accommodate deformation because of their lower elastic modulus, may still be susceptible to cracking because of their low K_{Ic}. The adhesion strength between the SE and Li metal also directly affects the stability of interfacial contact during cycling. Weak adhesion facilitates delamination and contact loss, leading to increased R_{int} and less uniform charge transfer.

Interfacial evolution is also governed by electrochemical stability. In principle, the electrochemical stability window of a SE can be predicted using first-principles calculations. Under practical cycling conditions, however, reaction kinetics and interfacial transport can considerably alter the apparent stability range. When an electrode contacts a SE, redox decomposition, elemental interdiffusion, and other side reactions may occur, producing interphases with different ionic and electronic conductivities. An ideal interphase should conduct Li-ion while remaining electronically insulating, thereby preventing continuous

electrolyte decomposition. Strategies based on intrinsic thermodynamic stabilization, kinetic stabilization, and artificial protective layers, such as $LiNbO_3$ coatings, are therefore widely used to regulate interfacial reactions, reduce R_{int}, and improve cycling stability.

Yue et al. [115] combined operando mechanical measurements with electrochemical analysis to examine interfacial evolution in ASSLMBs under electro-chemo-mechanical coupling, as illustrated in Figure 3k. Li deposition was found to proceed through several distinct stages. During the initial stage, Li deposited relatively uniformly. As deposition continued, mechanical stress gradually accumulated and promoted the formation of interfacial voids. At a later stage, the voids caused local current focusing and further stress amplification, which facilitated Li-dendrite nucleation and growth and eventually led to cell failure. The rate of pressure change, (dP/dt), showed a clear correlation with the different stages of Li deposition and could therefore serve as an indicator of interfacial evolution and impending failure. Based on a stress-evolution model and a critical-stress criterion, the operating stress could be maintained below the failure threshold by optimizing parameters such as areal capacity, SE thickness, and current density. For example, reducing the areal capacity to 0.64 $mAh \cdot cm^{-2}$ or increasing the SE thickness to 1200 μm was shown to lower the mechanical stress while maintaining relatively low polarization and improved cycling performance. These results demonstrate that the electrochemical and mechanical design of ASSLMBs must be considered together. Cell parameters that improve energy density may also increase mechanical stress, and their optimization therefore requires a balance among capacity, polarization, and long-term interfacial stability.

4. Electro-Chemo-Mechanical Coupling Failure Mechanisms

During prolonged cycling, Li insertion/extraction in electrode materials, Li plating/stripping, and interfacial side reactions continuously generate local volume changes and stress evolution. Mechanical stress, in turn, can deteriorate ion transport, charge-transfer kinetics, and interfacial stability, thereby further amplifying electrochemical heterogeneity and accelerating electro-chemo-mechanical degradation [8,23,117]. This coupling occurs across several critical regions of ASSLMBs and leads to distinct forms of failure. In composite cathodes, repeated expansion and contraction of cathode particles can induce particle cracking, interfacial debonding, and disruption of ionic and electronic transport networks. Importantly, the evolving physical contact between the cathode active material and SE also regulates interfacial chemical reactions. Intimate contact provides pathways for electrochemical decomposition of the SE, whereas cathode contraction and the resulting interfacial separation can reduce the local reaction area while simultaneously deteriorating ionic transport. Thus, chemical reactions, volume evolution, and contact loss are mutually coupled rather than independent degradation processes [118–122]. At the Li-metal anode, local stress concentrations associated with nonuniform deposition may promote crack initiation and Li penetration through the SE [111,123,124]. Meanwhile, prolonged interfacial reactions and changes in solid–solid contact can result in contact loss, impedance growth, and progressive cell degradation [125,126]. The interaction between electrochemical processes and mechanical deformation is therefore a central factor governing the lifetime and safety of ASSLMBs.

With the development of operando characterization, multiscale simulation, and advanced mechanical analysis, it has become increasingly clear that failure in ASSLMBs cannot be attributed to a single electrochemical or mechanical process [11]. Instead, it arises from multiscale coupling among chemical reactions, structural evolution, and stress redistribution. This section discusses three representative failure modes: electro-chemo-mechanical degradation in composite cathodes, Li-dendrite growth and penetration of SEs, and interfacial degradation under electro-chemo-mechanical coupling. Together, these

mechanisms illustrate how electrochemical reactions induce mechanical instability and how the resulting mechanical damage feeds back into cell operation, providing a basis for understanding cell degradation and optimizing electrode and electrolyte design.

4.1. Electro-Chemo-Mechanical Failure in Composite Cathodes

The composite cathode is a multiphase region in which electrochemical reactions, ion transport, and electronic conduction occur simultaneously. Its structural stability therefore has a decisive influence on cell performance. Lithiation and delithiation generate composition-dependent chemical strain within cathode particles. When this strain is spatially heterogeneous or mechanically constrained by neighboring grains and the surrounding SE, heterogeneous stress fields develop within the particles and across cathode/SE interfaces. These stresses can cause particle cracking, interfacial debonding, and contact loss, which in turn redistribute Li-ion transport and reaction kinetics and progressively amplify electrochemical heterogeneity.

Koerver et al. [119] systematically investigated the evolution of the interface between the Ni-rich layered oxide NCM811 and the sulfide SE β-Li_3PS_4 in an ASSLMB. The first-cycle Coulombic efficiency was only 70.5%, substantially lower than that of a comparable liquid-electrolyte cell. During the following 50 cycles, the capacity continued to decrease by approximately 1–2% per cycle, eventually reaching a reversible capacity of only 81 $mAh \cdot g^{-1}$. At the same time, the cathode/SE R_{int} increased irreversibly by approximately 140 $\Omega \cdot cm^{-2}$ during the first charge and became a major contributor to capacity loss. SEM images of the composite cathode before and after cycling are shown in Figure 4a,b. In the pristine electrode, the NCM particles remained in close contact with the SE. After charging, however, distinct spherical gaps appeared around the particles, indicating that delithiation-induced contraction of NCM had degraded the interfacial contact. The authors attributed the capacity fading to a combination of chemical and mechanical processes. On the chemical side, β-Li_3PS_4 oxidized at high potential and formed a resistive cathode electrolyte interphase. On the mechanical side, contraction of NCM811 during delithiation generated stress and caused the particles to lose effective contact with the surrounding SE. Importantly, chemical and mechanical degradation at the cathode/SE interface should not be regarded as independent processes. The evolution of physical contact determines the spatial extent of interfacial reactions, while reaction products can modify interfacial adhesion, transport resistance, and the local mechanical response, establishing a reciprocal chemo-mechanical feedback loop.

Zhang et al. [127] further used ex situ transmission XCT to reveal macroscopic mechanical failure in solid-state cells operated without external pressure. As shown in Figure 4c,d, an In/$Li_{10}GeP_2S_{12}$ (LGPS)/LCO cell developed pronounced bending and edge cracking after the first charge. This deformation arose from the mismatch in volume change between the two electrodes. During delithiation, LCO expanded by approximately 2% along the c-axis because of increased electrostatic repulsion between adjacent layers. By contrast, lithiation of the In anode to form $InLi_{1-x}$ involved a tetragonal-to-cubic phase transition and a volume expansion of up to 105.6%. The authors noted that similar mechanical mismatch is common in many electrode combinations, including NCM and LFP, and represents a major challenge for next-generation ASSLMBs.

Low-strain or near-zero-strain electrode materials, such as $Li_4Ti_5O_{12}$ (LTO), together with optimized external mechanical constraint, may therefore help accommodate cycling-induced volume changes and preserve interfacial stability. Cells operated without external pressure showed poor cycling performance, whereas pressure-confined cells maintained substantially more stable electrochemical behavior. This comparison directly demonstrates

the importance of external pressure in preserving continuous electrode/electrolyte contact and maintaining ionic and electronic transport pathways.

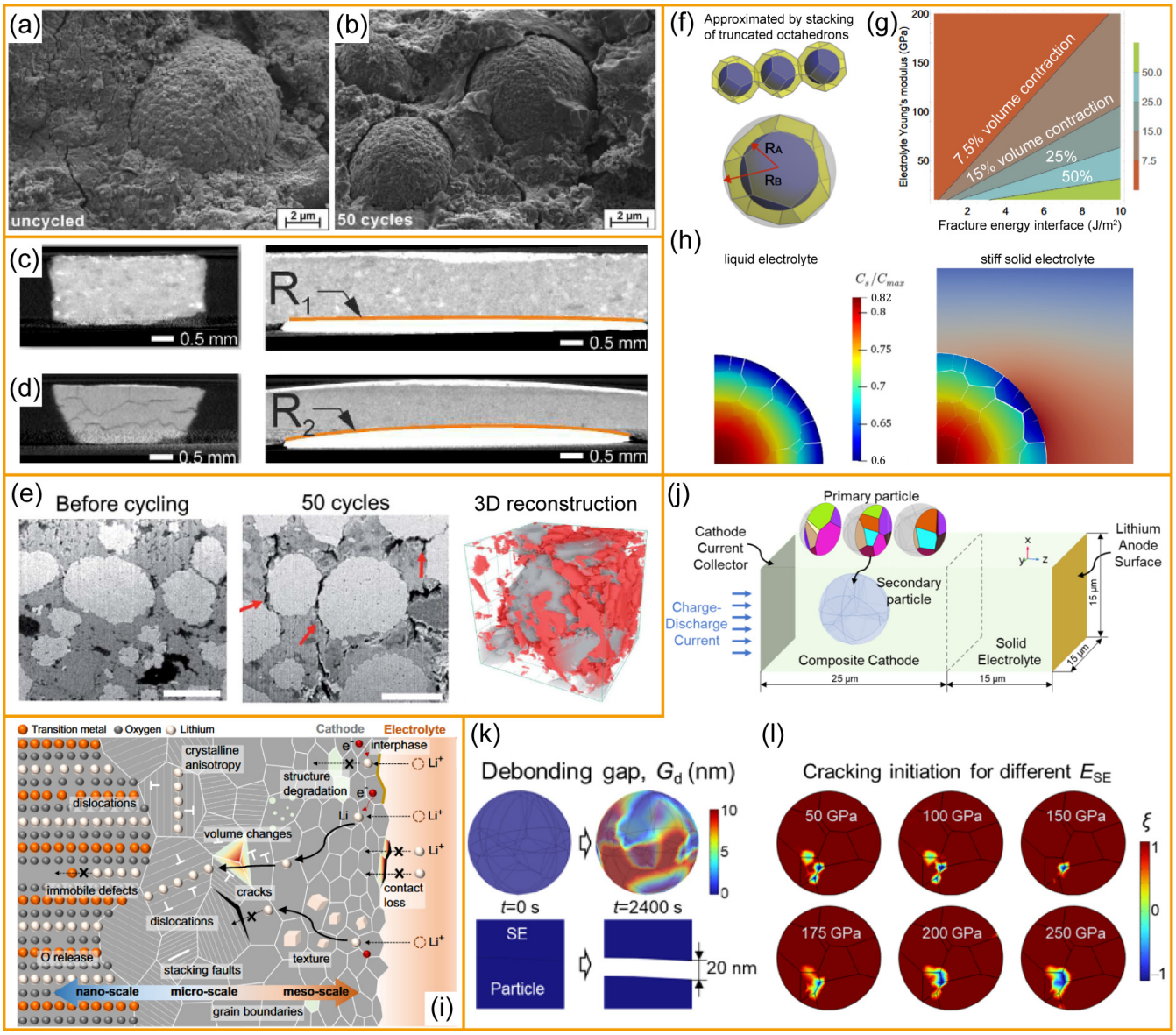


Figure 4. Electro-chemo-mechanical degradation and failure mechanisms in composite cathodes of ASSLMBs. (**a**–**e**) Experimentally observed mechanical degradation of solid-state batteries and composite cathodes during electrochemical cycling, including cycling-induced electrode deformation, cell bending and edge cracking caused by electrode-volume mismatch, and progressive loss of solid–solid contact around cathode particles. (**a**,**b**) Reproduced with permission from Ref. [119]. Copyright 2017 American Chemical Society. (**c**,**d**) Reproduced with permission from Ref. [127]. Copyright 2017 The Royal Society of Chemistry. (**e**) Reproduced from Ref. [118] under the CC BY-NC 3.0 license. Copyright 2020, the authors. Published by the Royal Society of Chemistry. (**f**,**g**) Mechanics of cathode particle/SE interfacial debonding, illustrating the idealized composite-electrode microstructure and the dependence of critical particle-volume contraction for debonding on interfacial fracture energy and SE stiffness. (**f**,**g**) Reproduced with permission from Ref. [128]. Copyright 2018 American Physical Society. (**h**,**i**) Influence of mechanical constraint imposed by the SE on cathode-particle fracture, showing the transition from predominantly radial opening-mode cracking under weak constraint to mixed-mode fracture involving radial and circumferential cracking and grain-boundary shear under solid-state confinement. (**h**) Reproduced with permission from Ref. [129]. Copyright 2021 Elsevier Ltd. (**i**) Reproduced from Ref. [120] under the CC BY 4.0 license. Copyright 2024, the authors. (**j**–**l**) Coupled

electrochemical–mechanical modeling of cathode particle/SE interfacial failure, illustrating the 3D ASSLMB configuration, nonuniform interfacial debonding induced by cathode contraction during delithiation, and the influence of SE mechanical properties on stress accumulation, crack initiation, and interfacial separation. (**j–l**) Reproduced with permission from Ref. [130]. Copyright 2025 Elsevier B.V.

Shi et al. [118] systematically examined the relationship between electrochemical performance loss and mechanical degradation in a composite cathode. The initial discharge capacity was 129 $mAh \cdot g^{-1}$ and gradually decreased to 102 $mAh \cdot g^{-1}$ during the first 26 cycles. A rapid decline then occurred between cycles 30 and 40, and the final capacity fell below 20 $mAh \cdot g^{-1}$. Cross-sectional SEM analysis before and after cycling, shown in Figure 4e, revealed that the volume fraction of contact-loss regions around the cathode particles increased from 2.87 to 10.4 vol%, demonstrating substantial interfacial debonding. Notably, contact loss was concentrated mainly on one side of each particle. This asymmetric debonding may occur because local separation on one side is sufficient to release part of the strain generated by particle expansion and contraction. The nonuniform debonding lengthened Li-ion transport pathways and gradually isolated parts of the cathode from the electrochemical reaction. More importantly, after 50 cycles, reapplying a pressure of 300 MPa restored the capacity to approximately 80 $mAh \cdot g^{-1}$. This partial recovery directly confirmed that mechanical degradation was a major cause of the observed capacity loss.

Based on these observations, Shi et al. proposed two possible mechanisms for electro-chemo-mechanical failure. The first is synergistic chemical and mechanical degradation. Continued interfacial side reactions, even in the presence of an Li–Zr-oxide (LZO) coating, produce a reaction layer that weakens interfacial adhesion and facilitates crack propagation. Residual stresses introduced by the reaction products are then superimposed on the stresses generated by electrode volume changes. The second mechanism involves the progressive accumulation of microcracks. Small cracks formed during early cycling may remain below the detection limit of conventional characterization methods. As cycling continues, they accumulate and coalesce into large-scale interfacial debonding, eventually causing severe electrochemical degradation.

In addition to experimental studies, electro-chemo-mechanical models have been developed to clarify failure in composite cathodes. Bucci et al. [128] used a one-dimensional radially symmetric analytical model to investigate interfacial debonding between a cathode particle and the surrounding SE and to evaluate its effect on cell performance. The idealized electrode microstructure is shown in Figure 4f. The composite electrode was represented as a periodic assembly of truncated octahedral unit cells, each containing one cathode particle. Radial symmetry was then used to describe the mechanical coupling between the particle and the surrounding electrolyte. On this basis, the authors established a relationship between particle contraction and interfacial failure and calculated contour maps of the relative particle-volume contraction under different combinations of material properties, as shown in Figure 4g. For most combinations of interfacial fracture energy and electrolyte stiffness, a radial strain of only approximately 2.5%, corresponding to a volume change of about 7.5%, was sufficient to initiate interfacial debonding. A more compliant SE could accommodate particle deformation and reduce stress accumulation, allowing particle-volume changes of up to approximately 25% before debonding occurred. The model also suggested that nanoscale cathode particles with radii of approximately 50–500 nm can stabilize crack growth and reduce the risk of abrupt interfacial separation during cycling.

Rezaei et al. [129] developed a thermodynamically consistent framework to describe intergranular fracture within cathode particles under electro-chemo-mechanical coupling. As shown in Figure 4h, the study compared particle failure in the absence and presence

of mechanical constraint from a SE. In a liquid-electrolyte environment, where external mechanical constraint is weak, cracks primarily propagate radially from the particle interior toward the surface and are dominated by opening-mode fracture, or normal failure (Mode I). Under SE constraint, however, the rigid surrounding phase restricts particle deformation and substantially changes the crack pattern. In addition to radial cracks, circumferential cracks parallel to the particle surface develop, together with shear sliding along grain boundaries characteristic of shear failure (Mode II) fracture. The mechanical constraint imposed by the SE therefore fundamentally alters the damage mode of cathode particles. Whereas failure in liquid cells is dominated by opening cracks, a stiff SE promotes mixed-mode fracture involving both normal separation and shear sliding. This change directly affects particle integrity, interfacial contact, and capacity retention. Mechanical compatibility between the cathode material and SE is therefore a key requirement for the long-term stability of composite cathodes.

Yuan et al. [130] developed a fully coupled electrochemical–chemical–mechanical model to study cracking of cathode particles and failure of the particle/SE interface in ASSLMBs. The 3D model included a composite cathode, an LLZO SE, and a Li-metal anode, as illustrated in Figure 4j. During delithiation, the cathode particles contracted, while the stiff SE could not deform sufficiently to accommodate the shrinkage. The resulting mechanical mismatch caused interfacial debonding. The maximum debonding gap G_d, reached approximately 23.4 nm and was strongly nonuniform, leading to a rapid increase in R_{int}, as shown in Figure 4k. The authors also examined the influence of the Young's modulus of the SE. A lower-modulus electrolyte, such as a sulfide, accommodated particle contraction more effectively and reduced the associated mechanical stress, thereby delaying interfacial separation and crack initiation, as shown in Figure 4l. Nevertheless, reducing electrolyte stiffness only delayed failure and could not eliminate the interfacial degradation and particle fracture caused by repeated volume changes.

Liu et al. [120] finally examined the role of grain-level chemo-mechanics in the degradation of composite cathodes. The coupled processes of electrochemical reaction, Li insertion, structural evolution, and lattice-defect formation are summarized in Figure 4i. Because of crystallographic anisotropy, SOC-dependent Li diffusion, and substantial lattice-parameter changes, cycling generates nonuniform elastic strain within the grains and produces local regions of high stress. These stress concentrations promote the formation of crystal defects such as dislocations and stacking faults, which tend to accumulate preferentially near the outer region of secondary particles [48]. Local lattice distortion around these defects alters the oxygen coordination environment and lowers the formation energy of oxygen vacancies. Such defect-associated strain fields may lower the energetic barrier for oxygen-vacancy formation and facilitate TM migration, thereby providing a possible mechanistic link between mechanical defect accumulation and irreversible surface or bulk reconstruction.

Contact loss at the cathode/SE interface was also shown to originate not only from external operating conditions but from microscopic mismatch between anisotropic chemical expansion of the cathode and mechanical constraint from the SE. Even under low-rate cycling, the interface can remain under substantial tensile stress, leading to debonding and loss of contact. Therefore, composite-cathode degradation is inherently a multiscale process driven by grain-level electro-chemo-mechanical coupling. Cycling-induced crystal defects serve as initiation sites for oxygen loss and structural reconstruction, which also accelerate electrochemical degradation. At the same time, interfacial contact loss arises from the mismatch between cathode volume change and electrolyte mechanical properties. Conventional surface coatings or interfacial treatments alone are therefore unlikely to fully prevent degradation. Effective mitigation will require coordinated control of crystal structure, interface chemistry, and mechanical compatibility.

4.2. Li-Dendrite Growth and SE Penetration

The preceding sections established the conditions that destabilize the Li/SE interface: nonuniform plating and stripping generate localized stress, while the resulting stress and contact heterogeneity further concentrate current and promote Li transport into defects. Once this feedback exceeds the ability of Li to relax through creep or of the SE to resist fracture, the interfacial instability develops into a distinct failure process involving Li-filament growth, crack propagation, and eventual electrolyte penetration.

Accordingly, this section shifts the emphasis from the origin and electrochemical influence of stress to the physical progression of failure. Li penetration is treated as a multistage electro-chemo-mechanical process comprising preferential nucleation at structurally or electrochemically active sites, pressure buildup within Li-filled defects, crack opening and extension, and the formation of a continuous electronically conductive pathway through the SE. Particular attention is given to how the location and nature of defects determine the initiation site, propagation geometry, and final short-circuit pathway.

4.2.1. Li-Dendrite Growth

Experimentally observed Li-penetration pathways can be classified according to their initiation location and propagation microstructure. Three representative modes are considered here: filament growth initiated at interfacial defects, propagation through grain-boundary or pore networks, and penetration initiated from defects within the bulk electrolyte. Although these modes share the same underlying coupling among deposition, pressure buildup, and fracture, they differ in their nucleation sites, spatial morphologies, and dominant propagation pathways.

(1) Li-filament growth initiated at interfacial defects

In this mode, pre-existing surface cracks, pores, or processing defects act as the initial sites for localized Li insertion. Continued filling pressurizes the defect and mechanically opens the surrounding SE, converting an initially isolated flaw into a propagating Li-filled crack.

Ning et al. [131] directly observed dendrite-induced crack initiation and propagation in a sulfide ASSLMB using operando XCT, as shown in Figure 5a. Li deposition did not begin directly at the electrolyte surface but first appeared within subsurface pores. As deposition continued, Li filled defect regions through interconnected pores and surface microcracks. As the viscoplastic flow of Li could not release the pressure rapidly enough, the pressure inside the pores continued to increase and eventually fractured the SE. Dendrite initiation was therefore governed by local microstructural factors, including grain-boundary fracture strength, pore size, pore density, and local current density. Once a crack had formed, its subsequent propagation was controlled by more macroscopic factors, such as electrolyte K_{Ic}, filament length, current density, stack pressure, and cycling capacity. Importantly, Li did not simply advance at the crack tip. It deposited within the crack and mechanically forced the crack to open further. The resulting failure is therefore best described as a coupled sequence of defect-assisted deposition, stress accumulation, and mechanical fracture.

Stack pressure also affected this process. Pressures of only a few megapascals had little influence on the critical current for dendrite initiation, whereas pressures above 50 MPa could lower the critical initiation current. Reducing the stack pressure, however, clearly slowed crack propagation. Mechanical boundary conditions therefore affect not only dendrite initiation but also the rate of subsequent penetration.

(2) Li propagation through grain boundaries and pores

Grain-boundary- and pore-assisted Li propagation is particularly important in polycrystalline SEs. Grain boundaries generally contain more structural defects, may possess lower mechanical strength, and often exhibit transport properties different from those

of the grain interiors. These characteristics make them favorable pathways for localized deposition and continuous Li penetration.

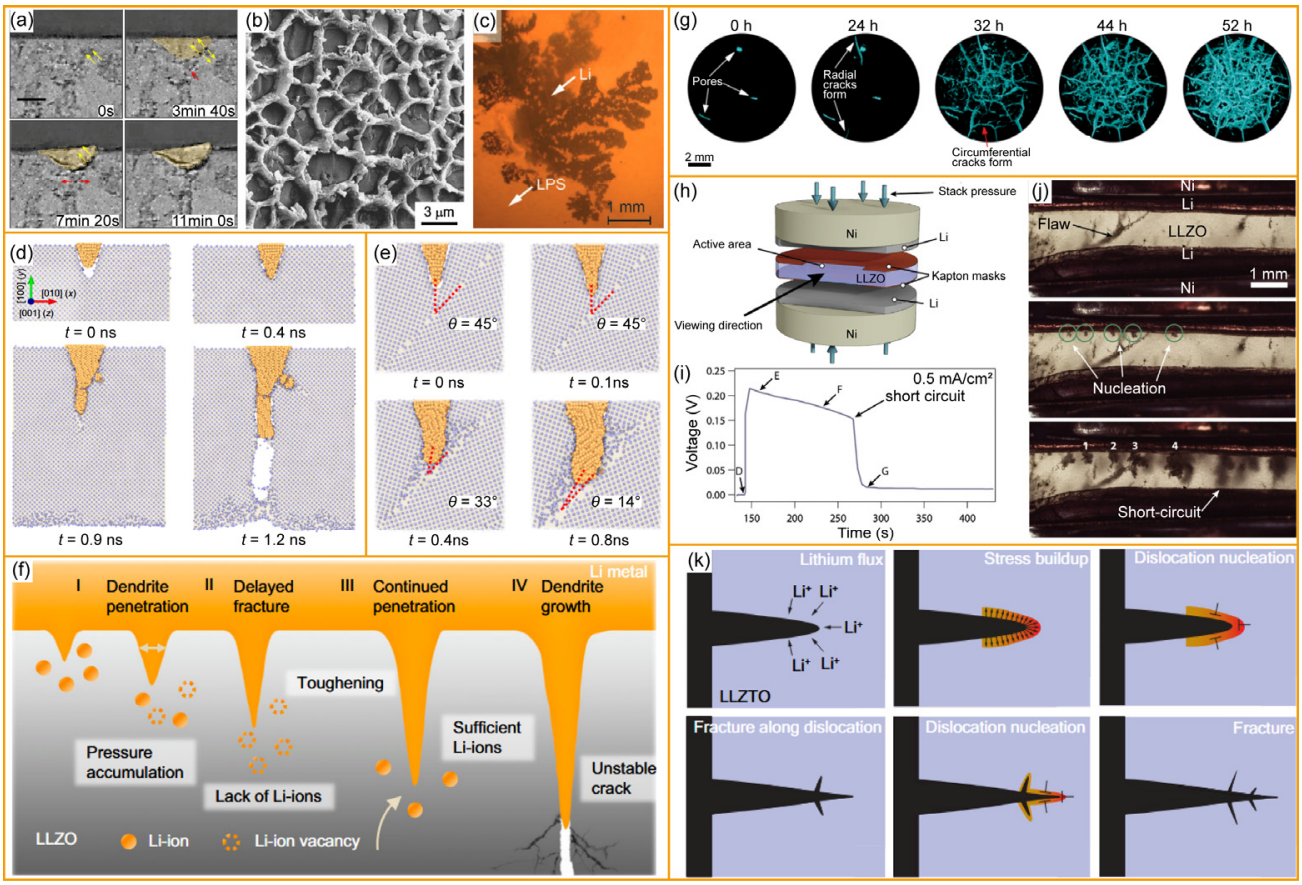


Figure 5. Li-dendrite growth and SE penetration mechanisms in ASSLMBs. (**a**–**c**) Representative Li-filament nucleation and propagation pathways in SEs, including defect-assisted Li deposition and crack initiation from subsurface pores or interfacial defects, preferential Li propagation along grain boundaries and pore networks, and Li nucleation within the bulk electrolyte associated with local electronic leakage and electrochemical heterogeneity. (**a**) Reproduced with permission from Ref. [131]. Copyright 2023, the authors, under exclusive licence to Springer Nature Limited. (**b**) Reproduced with permission from Ref. [132]. Copyright 2017 Elsevier Ltd. (**c**) Reproduced with permission from Ref. [111]. Copyright 2017 Wiley-VCH GmbH. (**d**–**f**) Atomic-scale mechanisms of mechanically driven Li penetration through crystalline SEs, showing stress accumulation and crack propagation ahead of Li-filled defects in single-crystalline LLZO, preferential filament deflection and propagation along grain boundaries in polycrystalline LLZO, and Li-concentration-dependent fracture behavior associated with local structural reconstruction and crack-tip toughening. (**d**–**f**) Reproduced from Ref. [133] under the CC BY-NC-ND 4.0 license. Copyright 2025, the authors. (**g**) Progressive electro-chemo-mechanical degradation of a Li/LAGP interface, illustrating the evolution from an initially intact electrolyte to radial and circumferential crack networks during cycling and the associated increase in interfacial resistance. (**g**) Reproduced with permission from Ref. [134]. Copyright 2019 American Chemical Society. (**h**–**j**) Operando visualization of Li penetration through ceramic SEs, showing Li nucleation at surface defects, subsequent branched filament propagation through the electrolyte, and eventual formation of a continuous penetration pathway leading to internal short circuit. (**h**–**j**) Reproduced from Ref. [112] under the CC BY-NC-ND 4.0 license. Copyright 2020, the authors. Published by Elsevier Inc. (**k**) Defect-mediated Li-penetration mechanism involving dendrite-induced local stress, dislocation generation and accumulation near the filament tip, and their potential role in facilitating subsequent crack propagation. (**k**) Reproduced from Ref. [135] under the CC BY 4.0 license. Copyright 2024, the authors.

Cheng et al. [132] observed a network-like Li structure propagating along the grain boundaries of polycrystalline LLZO, as shown in Figure 5b. The hexagonal network visible on the fracture surface had a characteristic size of 2.6 ± 0.7 μm, comparable to the LLZO grain size, and followed the grain-boundary network. Auger electron spectroscopy revealed a substantially stronger Li signal in this region than in the surrounding LLZO matrix, directly confirming the presence of metallic Li along the grain boundaries. The authors attributed preferential deposition to the high defect density, enhanced local ion transport, and lower mechanical stability of the grain-boundary region. As Li filled the boundaries, it generated local stress concentrations and promoted intergranular cracking. The opened grain boundaries then provided continuous pathways for further Li penetration, eventually connecting the two electrodes and causing a short circuit. This study demonstrates that bulk mechanical properties, such as the average shear modulus, are insufficient to predict dendrite resistance in polycrystalline electrolytes. Grain-boundary engineering and defect control are equally important.

(3) Li penetration initiated within the electrolyte

In principle, SEs are expected to transport Li-ion while blocking electron transport, so that lithium deposition is restricted to the Li | SE interface. However, if the electronic conductivity of the SE is not sufficiently suppressed, electrons can infiltrate into the SE and induce the reduction of Li-ion within the SE. Meanwhile, defects such as pores, microcracks, and grain boundaries may serve as electron-trapping sites, leading to localized charge accumulation and internal lithium nucleation. Porz et al. [111] employed transmitted-light microscopy to visualize Li penetration in dense polycrystalline β-Li_3PS_4 under high current density, as shown in Figure 5c. Their observations demonstrated that Li penetration preferentially initiated from pre-existing defects, such as surface cracks, and propagated by filling and widening these defects once the critical current density was exceeded.

Han et al. [136] subsequently used operando neutron depth profiling to track changes in Li concentration and revealed a bulk-nucleation mechanism caused by electronic leakage. In LiPON, the Li concentration remained nearly unchanged during deposition and no obvious dendrite formation was detected. In LLZO and Li_3PS_4, however, the Li concentration increased throughout the bulk electrolyte without a clear dependence on distance from the electrode interface. This observation indicates that Li did not grow directionally from the electrode into the electrolyte. Instead, metallic Li nucleated directly within the bulk. When a SE has appreciable electronic conductivity, electrons can enter the electrolyte and combine with mobile Li-ion in regions where the local electrochemical potential falls below the Li-plating potential. Bulk Li formation therefore requires two conditions: mobile electrons must be present within the electrolyte, and the local electrochemical potential must be below the Li/Li-ion equilibrium potential.

Unlike interface-driven dendrite growth, electronically induced Li deposition produces distributed nucleation sites throughout the electrolyte, with little correlation between Li distribution and distance from the interface. These observations demonstrate that electronic leakage, defect-assisted lithium nucleation, and the associated electro-chemo-mechanical coupling collectively govern dendrite formation in SEs.

4.2.2. Penetration of SEs

The ability of soft Li metal to penetrate mechanically strong ceramic electrolytes has attracted extensive attention. Two main explanations have been proposed. The first attributes penetration to the accumulation of local stress during Li growth. Once the stress exceeds the fracture resistance of the electrolyte, cracks initiate and Li advances through the newly formed pathways. The second proposes that electronic leakage at grain boundaries

promotes local reduction of Li-ion, generating isolated Li nuclei that eventually connect into a continuous metallic pathway.

Dehm's group [137] combined cryogenic electron microscopy with mechanical modeling to investigate the microscopic mechanism of Li penetration. The Li-dendrite tip produced both transgranular and intergranular fracture and subsequently filled the resulting nanoscale cracks. No isolated Li nuclei were observed ahead of the advancing tip. This result supports a mechanically driven crack-propagation mechanism rather than independent Li nucleation caused by electronic leakage. The stress state within the Li filament was also found to be close to hydrostatic, indicating that pressure generated by confined Li growth can provide the driving force for electrolyte fracture.

Using molecular dynamics simulations, Zhang et al. [133] examined the atomic-scale evolution of Li penetration through single-crystalline LLZO. Snapshots at 0, 0.4, 0.9, and 1.2 ns are shown in Figure 5d. Li initially nucleated at a pre-existing defect. Continued deposition then increased the stress within the Li filament until fracture was initiated at its tip, allowing Li to advance further into the electrolyte. The simulations therefore revealed a direct relationship among pre-existing defects, local stress concentration, and crack propagation. They further showed that the local Li-ion concentration could alter the fracture response of LLZO. As illustrated in Figure 5f, a reduction in Li-ion concentration near the crack tip promoted the formation of oxygen bridges behind the advancing crack. These bridges strengthened local atomic bonding, increased K_{Ic}, and slowed further crack growth. Li-ion therefore influence not only the electrochemical deposition process but also the mechanical response of the SE by modifying its local atomic structure.

Zhang et al. also investigated Li penetration in polycrystalline LLZO containing a Σ5(310) grain boundary. As shown in Figure 5e, even when a filament initially nucleated inside a grain, it deflected upon approaching the grain boundary and then propagated preferentially along it. Atomic-scale analysis showed that the grain boundary reduced Li-ion diffusivity and produced a step-like concentration distribution, with a Li-rich region on one side and a Li-poor region on the other. This resembled a local space-charge layer. The local electrostatic potential was also lower at the grain boundary, favoring reduction and deposition of Li. Grain boundaries therefore promote Li penetration in two ways: mechanically, by acting as weak fracture paths, and electrochemically, by altering local ion transport and potential distribution.

Tippens et al. [134] used operando XCT to investigate electro-chemo-mechanical degradation in Li/LAGP/Li cells and directly observed the formation and growth of a crack network. As shown in Figure 5g, the pristine LAGP electrolyte contained no obvious defects. After 24 h of cycling, radial cracks began to extend from the interior toward the edge. With further cycling, these cracks developed into a 3D network composed of radial and circumferential fractures. The cracks were concentrated mainly in the region in contact with Li metal, which covered approximately 75% of the LAGP surface, whereas the uncovered edge region showed much less damage. This spatial correlation indicates a close relationship between interfacial reaction and mechanical failure. EIS showed that the R_{int} increased from approximately 2.81 to 256 $k\Omega \cdot cm^{-2}$, representing an increase by roughly 175 times. The resistance remained relatively stable before crack initiation but increased rapidly once cracking began and reached its maximum when the damaged area reached 72.4%.

The authors attributed fracture to tensile stress generated by the volume expansion of interfacial reaction products. The rapid increase in resistance was caused mainly by interruption of Li-ion transport pathways by the cracks rather than by the intrinsic resistance of the interphase itself.

Kazyak et al. [112] developed an operando transmission Li/LLZO/Li cell that enabled direct observation of Li deposition, dendrite propagation, and final short circuiting. As

shown in Figure 5h–j, under galvanostatic plating at 0.5 mA·cm^{-2}, Li first nucleated at a surface defect and subsequently propagated through LLZO in a branched morphology until the electrolyte was fully penetrated. The operando platform allowed Li penetration to be monitored under conditions approaching practical cell operation, including current densities above 1 mA·cm^{-2} and R_{int} below 5 Ω·cm^{-2}. Such direct visualization provides a basis for developing early-warning indicators of failure and for optimizing Li/SE interface design.

In addition to crack propagation, dislocations have recently been proposed as possible contributors to penetration failure in ceramic electrolytes. Unlike metals, dislocation motion in ceramics is extremely slow at RT, typically ranging from nanometers to micrometers per second [138,139]. Increasing the applied stress is also more likely to trigger brittle fracture than sustained dislocation motion. Dislocations are therefore unlikely to move fast enough to remain ahead of a rapidly growing Li filament. Instead, they may form as local structural defects in response to dendrite-induced stress. Yildirim et al. [135] proposed the mechanism illustrated in Figure 5k, in which high local stresses generated by Li growth nucleate dislocations in the ceramic electrolyte. The residual dislocation structures may then provide preferred paths for subsequent crack propagation. Dislocation nucleation in ceramics generally requires stresses on the order of gigapascals, but such stress levels may be reached locally near an advancing Li filament. Although operando diffraction detected residual stresses of only several tens of megapascals after dendrite formation, indicating substantial stress relaxation, the remaining dislocations may still lower the energy barrier for fracture and promote Li penetration along selected pathways.

Collectively, these observations show that Li-dendrite penetration is not a single-step deposition event but a progressive failure sequence controlled by defect activation, Li filling, pressure accumulation, and fracture. The relative importance of these stages depends strongly on electrolyte microstructure, grain-boundary properties, defect population, current density, and mechanical boundary conditions. Directly resolving such transient and buried processes requires advanced operando characterization, as discussed in Section 5.2.

4.3. Interfacial Degradation Under Electro-Chemo-Mechanical Coupling

A typical ASSLMB contains a metal anode, a SE, and a composite cathode, together with several potentially vulnerable interfaces. These include the anode/SE interface, the cathode/SE interface, and interfaces associated with the CCs. Because electrode/SE interfaces directly participate in Li-ion transfer and electrochemical reactions, they are particularly important to cell performance and cycling stability.

The degradation mechanisms of the anode and cathode interfaces are nevertheless different. A metal-anode/SE interface is usually a relatively planar 2D contact. Its stability is governed mainly by volume changes during Li plating and stripping, local stress evolution, and the dynamic redistribution of contact. By contrast, the composite-cathode/SE interface is a complex 3D multiphase network. Its stability depends not only on electrode microstructure but also on the spatial continuity of contact among cathode particles, SE particles, and the electronic-conduction network. Understanding the electro-chemo-mechanical behavior of these different interfaces is therefore essential for clarifying failure in ASSLMBs.

4.3.1. Evolution of Interfacial Contact in Composite Electrodes

Interfacial contact stability is a major determinant of long-term cycling performance. Huo et al. [140] compared the interfacial evolution of a composite Si/LPSC anode with that of a Si anode lacking a continuous SE network. Cross-sectional SEM images before and after cycling, shown in Figure 6a, indicated that the composite Si/LPSC electrode retained a relatively stable internal structure during prolonged cycling. By contrast, the Si electrode

without an electrolyte network developed progressive debonding, void formation, and ion-transport failure because of the large volume changes associated with lithiation and delithiation. The difference arose because LPSC formed a continuous 3D Li-ion transport network within the composite electrode and mechanically constrained the Si particles. This network accommodated part of the local strain generated by repeated particle expansion and contraction, reduced interfacial stress concentration, and preserved electrochemical contact. A simple 2D Si/LPSC interface, in contrast, could not adapt sufficiently to the large deformation of Si and therefore degraded continuously.

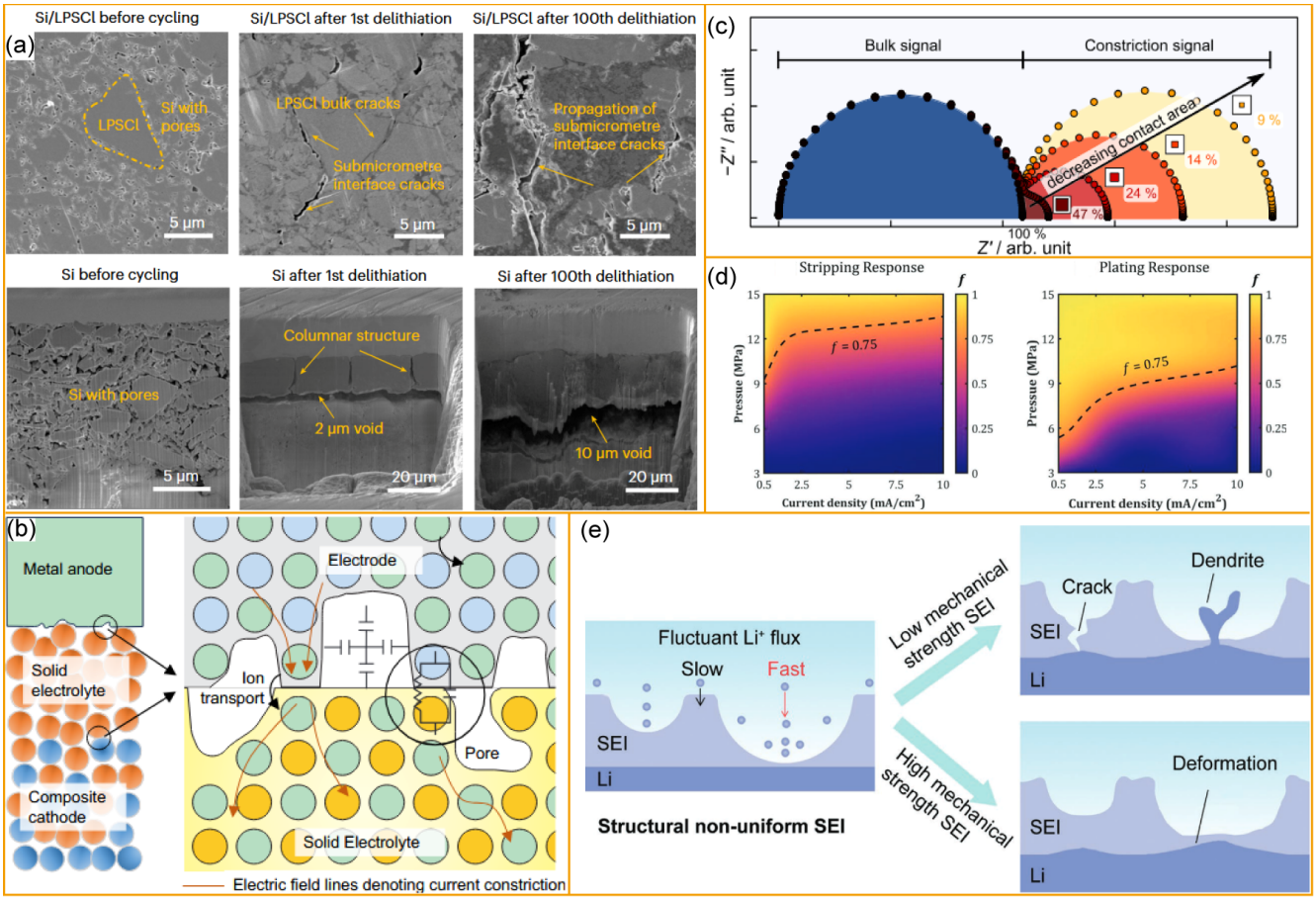


Figure 6. Electro-chemo-mechanical interfacial degradation in ASSLMBs. (**a**) Evolution of interfacial contact in Si-based composite electrodes, illustrating the role of a continuous 3D SE network in accommodating cycling-induced volume changes, suppressing debonding and void formation, and preserving ionic transport pathways. (**a**) Reproduced from Ref. [140] under the CC BY 4.0 license. Copyright 2024, the authors. (**b**–**d**) Contact-loss-induced degradation at the Li/SE interface, showing the evolution of microscopic contact regions and current constriction during Li stripping, the characteristic impedance response associated with decreasing real contact area, and the asymmetric contact evolution between Li plating and stripping under different current densities and stack pressures. (**b**) Reproduced from Ref. [55]. under the CC BY-NC 4.0 license. Copyright 2025 ASME. (**c**) Reproduced from Ref. [141] under the CC BY-NC-ND 4.0 license. Copyright 2022, the authors. Published by the American Chemical Society. (**d**) Reproduced from Ref. [142] under the terms of the CC BY 4.0 license. Copyright 2022, the authors. Published by Wiley-VCH GmbH. (**e**) Coupled morphological and mechanical evolution of the SEI during Li deposition, illustrating how nonuniform Li-ion flux induces localized Li growth and heterogeneous stress, ultimately leading to mechanical failure of the interfacial layer. (**e**) Reproduced with permission from Ref. [143]. Copyright 2020 Wiley-VCH Verlag GmbH & Co. KGaA, Weinheim.

The mechanical response of a full solid-state cell is not determined solely by the volume change of one electrode. It also depends on strain matching between the cathode and anode and on the overall mechanical boundary conditions. For example, half cells using In/InLi anodes showed a negative pressure change during cycling, whereas full cells containing $Li_2B_4O_7$ (LBO)-coated NCM cathodes showed a positive pressure change. This difference indicates that strain coupling between the two electrodes can alter the internal mechanical state of the cell and may help maintain contact through sustained compressive stress. Interfacial-stability assessments based only on half-cell configurations may therefore not fully represent the mechanical environment of a practical ASSLMB. Longer cycle life will require low-strain or near-zero-strain electrode materials, or deliberate matching of cathode and anode volume changes, so that the deformation of the two electrodes can be coordinated and electro-chemo-mechanical interfacial degradation minimized.

4.3.2. Contact Loss and Impedance Evolution at the Li/SE Interface

Ahmad et al. [55] analyzed interfacial degradation in ASSLMBs from the perspective of solid–solid contact mechanics. As illustrated in Figure 6b, the work described the evolution of real contact area during Li stripping and the resulting current-constriction effect. The interfacial contact state was jointly controlled by current density and external stack pressure. Higher pressure promoted creep deformation at the interface, increased the real contact area, and helped compensate for voids formed during Li stripping, thereby delaying contact failure. As contact area continued to decrease, however, current was forced through a limited number of conductive regions. The resulting convergence of current lines increased the local current density and aggravated interfacial polarization.

Eckhardt et al. [141] identified the impedance signature of contact loss at a metal/SE interface, as shown in Figure 6c. As the contact area decreased, an additional semicircle appeared in the low-frequency region of the EIS, while the high-frequency bulk resistance remained essentially unchanged.

The additional low-frequency response originated from the increase in constriction resistance caused by interfacial voids and the resulting reduction in effective contact area. It can therefore be used as an electrochemical indicator of mechanical degradation at solid–solid interfaces. Lu et al. [144] further investigated void formation and impedance evolution at the Li/SE interface during stripping. They constructed a map of interfacial contact loss as a function of areal capacity and current density. Severe contact loss occurred under conditions of both high areal capacity and high current density. This macroscopic degradation was traced to the accumulation of microscopic voids and the progressive reduction in real contact area.

Vishnugopi et al. [142] further demonstrated that the interfacial response is strongly asymmetric between Li plating and stripping, as shown in Figure 6d. For the same transferred capacity, stripping caused substantially greater contact loss than plating. External pressure was required during both processes to preserve a high contact-area fraction, but stripping required a larger pressure. For example, Li plating at 10 $mA \cdot cm^{-2}$ required approximately 10 MPa, whereas stripping at only 5 $mA \cdot cm^{-2}$ required approximately 12 MPa. This asymmetry confirms that stripping-induced void formation is one of the main factors limiting the cycling stability of ASSLMBs.

4.3.3. Interfacial Reaction Layers and Artificial SEI Design

Unlike in liquid lithium batteries, where the SEI formed by electrolyte decomposition has long been a central research topic, interfacial studies in ASSLMBs have traditionally focused on solid–solid contact, space-charge layers, and electro-chemo-mechanical behavior. Increasing evidence nevertheless shows that chemical reactions also occur between

SEs and electrodes, producing interfacial layers that may either protect or degrade the interface. Future interface design for ASSLMBs may therefore need to combine mechanical optimization with strategies adapted from liquid-electrolyte systems. Stable artificial interphases or intermediate layers may improve Li-ion transport, suppress side reactions, and accommodate interfacial deformation.

Shen et al. [143] showed that the uniformity of an SEI strongly affects Li-deposition morphology. As illustrated in Figure 6e, a nonuniform SEI produces a locally enhanced Li-ion flux, leading to the formation of Li protrusions. These protrusions generate vertical compressive stresses together with in-plane tensile and shear stresses. When the local von Mises stress exceeds the yield strength of the SEI, the layer fractures and loses its protective function.

The key requirement for SEI design is not simply the highest possible mechanical strength. Instead, the layer must combine structural uniformity with suitable mechanical properties. A low-modulus SEI may be unable to restrain morphological instability, whereas an excessively stiff SEI may undergo brittle fracture because it cannot accommodate local deformation. Artificial interphases for ASSLMBs should therefore be designed to balance structural uniformity, Li-ion conductivity, chemical stability, and mechanical compliance. Coordinated optimization of these properties is required to suppress interfacial side reactions while avoiding mechanically induced failure.

5. Characterization Techniques for Electro-Chemo-Mechanical Coupling

Recent advances in in situ, quasi-operando, and operando characterization techniques, together with the rapid development of 3D imaging methods, have enabled real-time visualization and quantitative analysis of structural evolution, interfacial dynamics, and mechanical responses in ASSLMBs. However, the electro-chemo-mechanical processes occurring within ASSLMBs involve coupled Li-ion transport, phase transitions, stress evolution, interfacial contact, and structural degradation across multiple length and time scales. Consequently, no single characterization technique can comprehensively capture these complex phenomena. Instead, different techniques provide complementary information, each offering distinct capabilities in terms of spatial resolution, operando compatibility, Li sensitivity, stress sensitivity, etc.

Figure 7 schematically summarizes the complementary roles of advanced characterization techniques in resolving electro-chemo-mechanical evolution in ASSLMBs. These methods probe three major aspects: structural and interfacial evolution in composite cathodes, dynamic Li plating and stripping at the anode/SE interface, and stress and mechanical responses across the cell. By combining imaging, spectroscopy, and mechanical sensing across multiple length scales, they enable the evolution of microstructure, interfacial contact, Li morphology, fracture, and stress distribution to be correlated with electrochemical cycling. Table 4 summarizes the characteristics of the most widely used characterization techniques for ASSLMBs, including their measured quantities, spatial resolutions, operando capability, Li sensitivity, stress sensitivity, major advantages and limitations. This comparison provides practical guidance for selecting appropriate characterization methods and highlights the complementary roles of different techniques in elucidating electro-chemo-mechanical coupling mechanisms in ASSLMBs.

Table 4. Comparison of representative characterization techniques for electro-chemo-mechanical behaviors in ASSLMBs.

Technique	Primary Information	Spatial Resolution	Operando Capability	Li Sensitivity	Stress Sensitivity	Major Advantages	Major Limitations	Ref.
Optical microscopy (OM)	Surface morphology, crack initiation, dendrite growth	~1–5 μm	✔	✗	△	Simple, low cost, large field of view	Limited to surface observations; no subsurface information	[145–147]
Scanning electron microscopy (SEM)/In situ SEM	Particle cracking, interface evolution, Li deposition	5–20 nm	✔*	✗	△	High spatial resolution; direct visualization	Vacuum environment; beam damage; limited buried interface observation	[148–150]
Focused ion beam (FIB)–SEM tomography	3D microstructure, porosity, interfacial contact	10–50 nm	✗	✗	△	High-resolution 3D reconstruction	Destructive; time-consuming; limited volume	[118,151]
Synchrotron X-ray tomography (XCT)	3D crack propagation, pore evolution	1–5 μm	✔	✗	△	Non-destructive 3D imaging	Weak contrast for Li; synchrotron required	[152,153]
Transmission X-ray microscopy (TXM)	Morphology, phase evolution	20–50 nm	✔	△	△	High-resolution operando imaging	Limited sample size; synchrotron dependence	[154,155]
X-ray absorption near-edge structure (XANES) imaging	Local oxidation state, reaction heterogeneity	30–100 nm	✔	✗	✗	Chemical reaction distribution	Chemical information only; indirect mechanical insight	[156]
Neutron imaging/tomography	Li distribution, transport pathways	10–100 μm	✔	✔	✗	Excellent Li sensitivity; non-destructive 3D imaging	Low spatial resolution; limited facility access	[157,158]
Neutron diffraction	Lattice strain, phase transition	Bulk	✔	✔	✔	Direct lattice strain measurement	Poor spatial resolution; large sample required	[159,160]
Synchrotron X-ray diffraction (XRD)	Lattice strain, phase transition	10–100 μm beam	✔	△	✔	High strain sensitivity; quantitative	Spatially averaged information; synchrotron required	[161]
Raman spectroscopy	Stress-induced peak shift and chemical bonds change	~0.5–1 μm	✔	△	✔	Sensitive to stress and chemistry	Fluorescence; limited penetration depth	[162,163]
Digital image correlation (DIC)	Surface strain field	~1–10 μm	✔	✗	✔	Full-field strain mapping	Surface only; requires optical access	[164,165]
Fiber bragg grating (FBG)	Local stress evolution	Local (sensor position)	✔	✗	✔	Highly sensitive operando local stress monitoring	Local measurement only; sensor integration required	[166]
Pressure sensor	Overall stack pressure	Cell scale	✔	✗	✔	Simple implementation	Cannot resolve local stress heterogeneity	[167]
Atomic force microscopy (AFM)	Surface modulus, adhesion	10–50 nm	△	✗	✔	Nanoscale mechanical mapping	Small scan area; slow imaging	[168]
Nanoindentation	Elastic modulus, hardness	~100 nm	✗	✗	✔	Quantitative mechanical properties	Local and destructive; no operando capability	[169]
Cryo-transmission electron microscopy (Cryo-TEM)	Atomic structure, SEI/interface	<1 nm	✗	✔	△	Atomic-scale interface characterization	Complex sample preparation; beam sensitivity	[170,171]

Note: ✓, applicable; ✗, not applicable; △, indirect sensitivity, where stress-related information is inferred from morphological or structural changes rather than directly measured; *, specially designed or modified electrochemical cells are required for operando measurements.

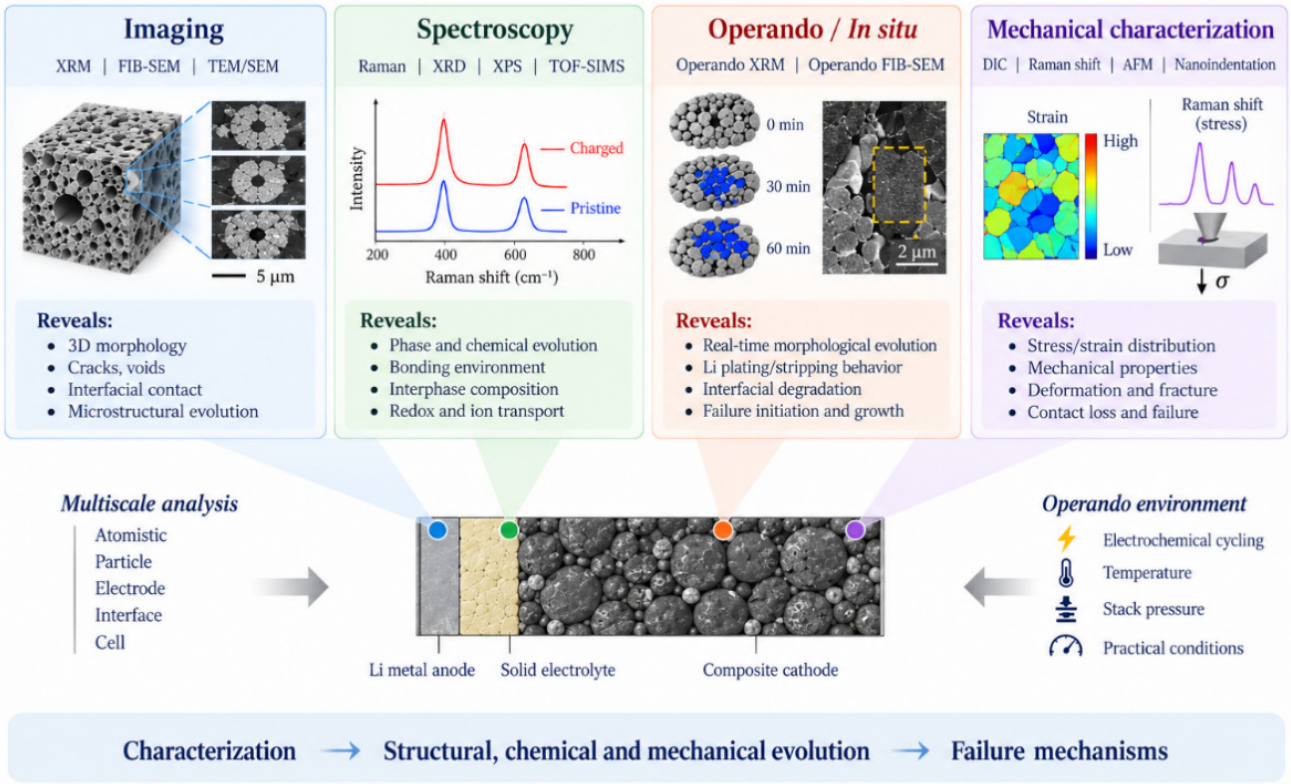


Figure 7. Schematic overview of advanced characterization techniques for probing composite-cathode evolution, Li plating/stripping dynamics, and stress and mechanical behavior in ASSLMBs.

5.1. Characterization of Composite-Cathode Structure and Interfacial Evolution

The composite cathode is a multiphase region in which ion transport, electronic conduction, and electrochemical reactions occur simultaneously. Its microstructural evolution therefore directly determines reaction uniformity and interfacial stability. A composite cathode contains several phases, including the cathode material, inorganic SE, electronically conductive additive, binder, and pores. Conventional 2D characterization is often unable to accurately resolve their 3D distributions, interfacial contact, and structural degradation during cycling. A range of advanced 3D imaging and operando or quasi-in situ techniques have therefore been developed, including FIB-SEM, synchrotron XCT, X-ray absorption near-edge structure (XANES) imaging, and transmission X-ray microscopy (TXM). These methods allow structural evolution and electro-chemo-mechanical failure in composite cathodes to be examined from the microscale down to the nanoscale.

Minnmann et al. [172] used plasma FIB-SEM tomography to investigate how the particle size of a sulfide SE affects composite-cathode microstructure and electrochemical performance, as shown in Figure 8a. Serial sectioning combined with high-resolution imaging enabled 3D visualization and quantitative analysis of the cathode material, SE, and pore network. Reducing the particle size of the inorganic SE substantially lowered the porosity of the composite cathode and allowed the electrolyte particles to fill the spaces between cathode particles more uniformly, thereby reducing cathode-particle agglomeration. 3D analysis further showed that smaller electrolyte particles decreased ionic tortuosity, shortened Li-ion transport pathways, and increased the effective ionic conductivity. This work demonstrates that 3D microstructural reconstruction can directly relate pore distribution and interfacial contact to electrochemical performance. It therefore provides an effective means of investigating porosity-driven chemo-mechanical degradation in composite cathodes.

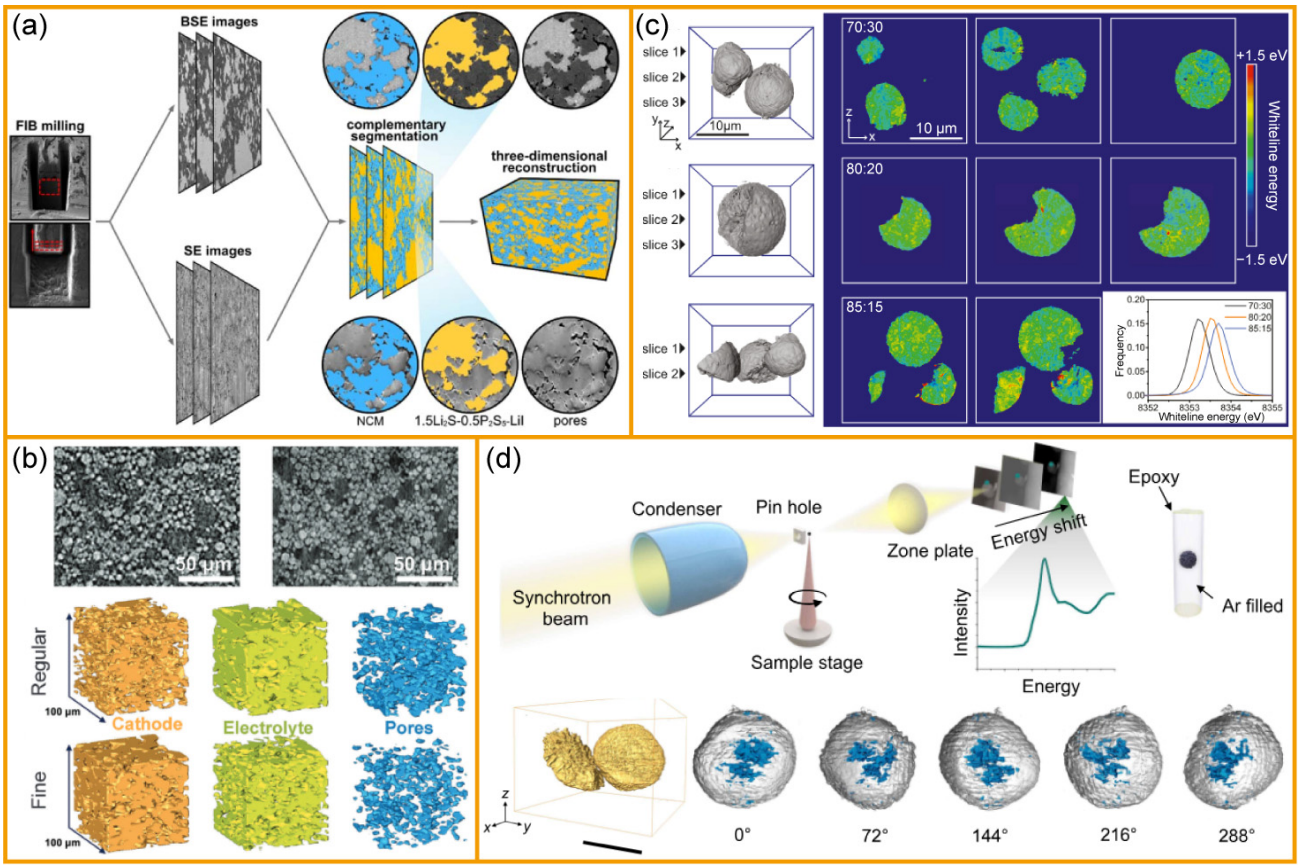


Figure 8. Advanced 3D characterization of structural and interfacial evolution in composite cathodes. (**a**,**b**) 3D reconstruction and quantitative microstructural analysis of composite cathodes with different SE particle sizes using plasma FIB–SEM tomography and synchrotron XCT, respectively, revealing the spatial distributions of cathode materials, SEs, and pores and the effects of SE particle size on porosity, interfacial contact, ionic-transport pathways, and electrode densification. (**a**) Reproduced from Ref. [172] under the CC BY 4.0 license. Copyright 2024, the authors. Published by IOP Publishing on behalf of The Electrochemical Society. (**b**) Reproduced from Ref. [173] under the CC BY-NC-ND 4.0 license. Copyright 2024, the authors. Published by Wiley-VCH GmbH. (**c**) Spatially resolved 3D XANES imaging of NCM/LPSC composite cathodes with different cathode loadings, correlating local Ni oxidation-state distributions with lithiation heterogeneity and revealing the relationship among cathode loading, microstructural degradation, local reaction nonuniformity, and electrochemical performance. (**c**) Reproduced with permission from Ref. [51]. Copyright 2025 American Chemical Society. (**d**) Full-field TXM reconstruction of cycled NCM811 particles, visualizing 3D internal cracking and particle fragmentation and quantifying crack-induced disruption of particle integrity and Li-ion transport pathways. (**d**) Reproduced from Ref. [109] under the CC BY-NC 4.0 license. Copyright 2025, the authors. Published by the American Association for the Advancement of Science.

Recent developments have extended FIB-SEM from post-mortem 3D reconstruction toward operando chemical imaging. Sharma et al. [174] integrated a dual-beam FIB-SEM with secondary ion mass spectrometry (SIMS) and a dedicated electrochemical holder, enabling simultaneous cell operation and spatially resolved Li imaging in a solid-state half-cell. By employing a ^{6}Li-enriched electrode as an isotopic tracer, changes in ^{6}Li concentration within the SE were visualized during current flow, directly revealing transient Li-ion migration across the electrode/electrolyte region. This operando FIB-SEM-SIMS approach therefore complements conventional FIB-SEM tomography by providing not only structural information but also time-resolved chemical information on Li transport pathways. However, since ion/electron-beam irradiation may perturb the specimen, beam-induced artifacts and chemical cross-talk must be carefully evaluated in operando FIB-based measurements.

Jeong et al. [173] similarly used synchrotron XCT to reconstruct composite cathodes containing SE particles of different sizes. Image segmentation was used to distinguish the cathode material, SE, and pores, as shown in Figure 8b. Smaller SE particles produced a denser and more uniform composite structure. The porosity of the small LPSC particles (LPSC-S) cathode was approximately 11 vol%, substantially lower than the 16 vol% measured for the large LPSC particles (LPSC-L) cathode. Mechanical testing further showed that, below a critical pressure of approximately 400 MPa, the more porous LPSC-L cathode underwent greater deformation and was therefore more mechanically compliant. Above this pressure, the responses of the two electrodes became similar, indicating that the pore structures had largely collapsed and become densified. The LPSC-S cathode also delivered a higher capacity and better cycling stability at different rates. At 0.1C, its capacity retention reached 94.26%, compared with only 47.33% for the LPSC-L cathode. This study shows that 3D imaging can reveal not only how porosity and contact influence ion transport, but also how microstructural evolution is related to macroscopic mechanical and electrochemical performance.

More recently, operando XCT has been applied directly to zero-excess ASSLMBs to assess how interfacial nucleation layers modify Li deposition and mechanical stability. Xu et al. [175] showed that bare Cu favored edge-localized, heterogeneous Li deposition, whereas an Ag-coated Cu interface promoted more spatially distributed Li growth, demonstrating how operando tomography can directly correlate interfacial design with deposition morphology and mechanical failure.

Spatially resolved chemical imaging has also been used to examine reaction heterogeneity within composite cathodes. Park et al. [51] applied 3D XANES to composite cathodes with different NCM/LPSC ratios, as shown in Figure 8c. This technique provides both the 3D distribution of cathode particles and spatially resolved information on local elemental oxidation states, allowing variations in lithiation state to be mapped directly. After full discharge, cathodes with a high NCM fraction showed a higher average Ni white-line energy, indicating a lower degree of lithiation. Their oxidation-state distributions were also more heterogeneous. This reaction heterogeneity was attributed mainly to local Li-ion transport limitations caused by crack formation and loss of interfacial contact during cycling. 3D chemical imaging can therefore reveal local reaction nonuniformity that cannot be detected by conventional bulk electrochemical measurements. It also provides direct evidence linking cathode loading, stress accumulation, reaction heterogeneity, and capacity fading.

Beyond X-ray-based chemical imaging, vibrational spectroscopy provides complementary information on local bonding environments and lattice evolution in composite cathodes. Raman spectroscopy provides a sensitive probe of local bonding environments and structural evolution in composite cathodes through changes in characteristic vibrational modes, while operando measurements further enable these changes to be correlated directly with electrochemical states during cycling. For example, Cao et al. [162] employed operando Raman spectroscopy to track the reaction chemistry of a sulfur cathode in an all-solid-state Li–S battery. The characteristic Raman bands of S_8 at 158, 220, and 473 cm^{-1} gradually weakened during discharge but remained detectable even at the fully discharged state, revealing incomplete sulfur conversion. Meanwhile, the C–S-related bands at 176 and 310 cm^{-1}, assigned to stretching and in-plane bending vibrations, respectively, also decreased slightly. During charging, the S_8 bands recovered and a transient band at approximately 438 cm^{-1} emerged at an intermediate state of charge, which was assigned to Li_2S_2, thereby providing direct spectroscopic evidence for the evolution of chemical species during the solid–solid conversion reaction.

Raman peak shifts can additionally serve as local fingerprints of lattice and bonding changes in oxide cathodes. Otoyama et al. [163] demonstrated this capability in LCO–SE composite cathodes: the pristine LCO exhibited Raman-active E_g and A_{1g} modes at approximately 486 and 596 cm^{-1}, corresponding to O–Co–O bending and Co–O stretching, respectively. Upon delithiation, both modes shifted toward lower wavenumbers and decreased in intensity, reaching approximately 470 and 582 cm^{-1} after charging to 4.2 V; these changes were attributed primarily to c-axis lattice expansion accompanying Li extraction. Spatial Raman mapping further distinguished low- and high-SOC LCO particles and revealed substantial reaction heterogeneity within the composite cathode, including residual low-SOC particles associated with insufficient contact with the SE. Thus, Raman spectroscopy can bridge molecular-scale bonding and lattice changes with spatially heterogeneous electrochemical reactions in composite cathodes.

To examine cycling-induced mechanical damage at the particle scale, Zheng et al. [109] used full-field TXM to reconstruct the internal structure of cycled NCM811 particles in three dimensions. This technique enables cracks and internal fracture structures to be imaged directly at nanoscale resolution, as shown in Figure 8d. After cycling, the NCM811 particles showed pronounced fragmentation and internal cracking, with cracks accounting for approximately 5.36% of the particle volume. The 3D reconstructions showed that these cracks not only disrupted particle integrity but also obstructed Li-ion diffusion pathways and isolated parts of the cathode from electrochemical reaction.

This work illustrates the value of advanced 3D microscopy for resolving complex failure processes in ASSLMBs and provides direct experimental evidence for understanding mechanical degradation in cathode particles.

5.2. Dynamic Characterization of Li Plating and Stripping

The failure mechanisms discussed in Section 4.2 develop at buried Li/SE interfaces and evolve rapidly from localized deposition to crack-assisted penetration. Post-mortem characterization can identify the final morphology of Li filaments and fractured electrolytes, but it cannot reliably determine where Li first nucleated, whether deposition preceded cracking or followed an existing crack, or how stress and microstructural defects altered the propagation pathway. Resolving these causal relationships requires operando or time-resolved characterization capable of tracking Li redistribution, interfacial contact, crack evolution, and local deformation during electrochemical cycling.

Recent advances in in situ SEM, operando optical microscopy (OM), in situ transmission electron microscopy (TEM), 3D focal-variation microscopy, X-ray imaging, and dark-field X-ray microscopy (DFXM) have enabled different stages of Li plating and stripping to be visualized across complementary length and time scales. Rather than repeating the mechanisms of dendrite formation, this section focuses on the information provided by these techniques, including nucleation location, deposition morphology, crack-initiation sequence, 3D penetration pathway, and the strain or defect fields surrounding Li filaments.

From a characterization perspective, Li-plating and stripping studies address four principal questions: where Li nucleates, how the Li morphology evolves, whether Li deposition causes or follows fracture, and how the resulting penetration pathway develops in three dimensions. Optical and electron microscopies provide high-temporal-resolution visualization of interfacial morphology, whereas X-ray-based techniques enable buried and 3D structures to be examined. Diffraction-based imaging further resolves lattice orientation, strain, and defect evolution around Li-filled cracks. These complementary capabilities are summarized below through representative operando and in situ studies.

Duan et al. [176] used in situ SEM to directly observe crack initiation and propagation induced by Li deposition in a Li | LPSC | Li symmetric cell, as shown in Figure 9a. The

operando imaging method captured changes in the surface morphology of the SE and revealed the dynamic relationship among Li deposition, crack evolution, and final short circuiting. During plating, a crack network first developed within the SE. Li then progressively filled the cracks and increased the local electronic and ionic conductivity, turning the damaged regions into rapid pathways for further Li growth. The cell consequently failed within a short period. These observations show that dendrite-induced failure is not governed solely by the morphology of deposited Li. It is also controlled by interfacial contact, local current distribution, and mechanical stress. In situ SEM provided direct evidence for a positive feedback process involving contact loss, current focusing, stress accumulation, and crack propagation.

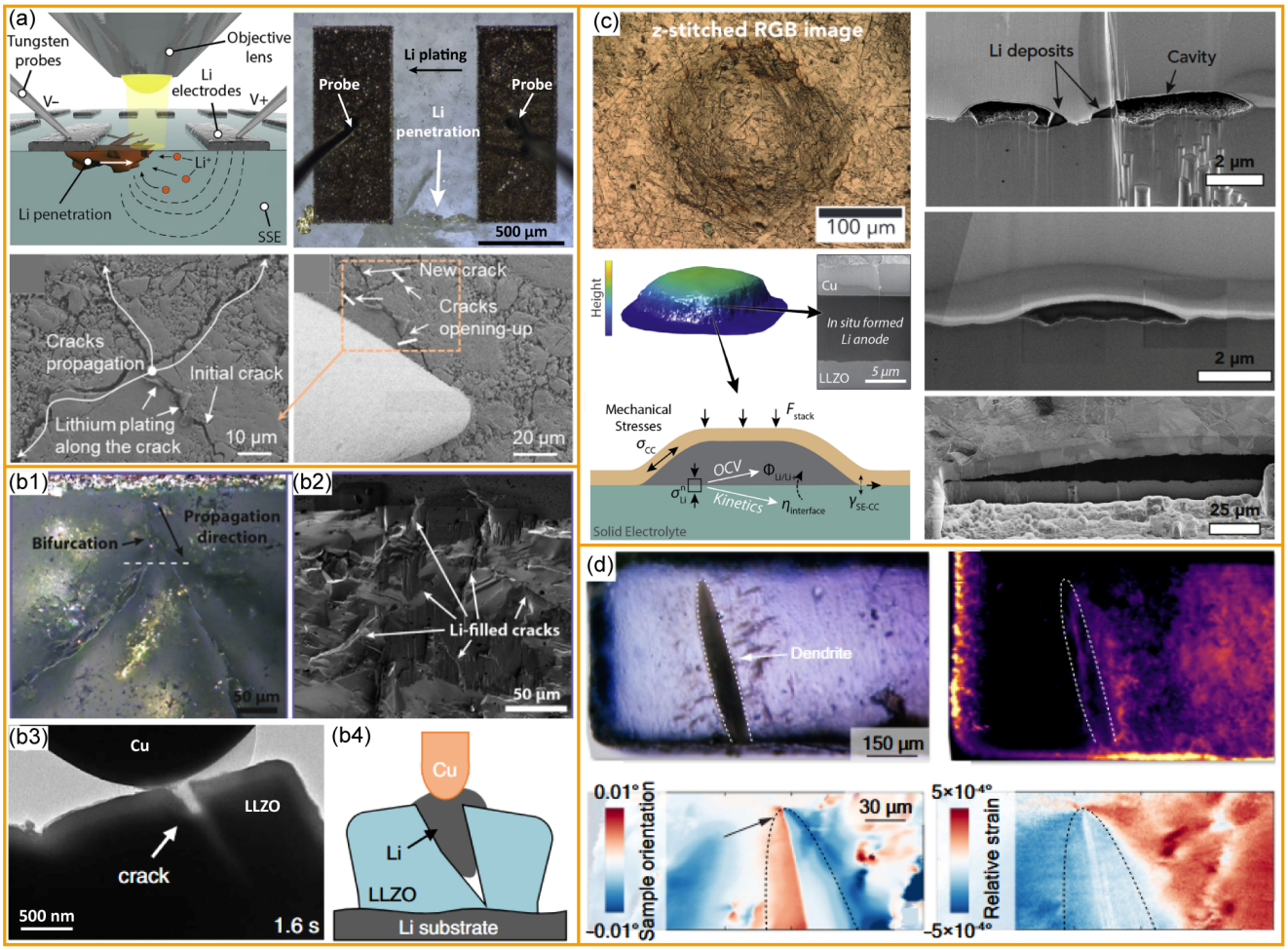


Figure 9. Multiscale in situ and operando characterization of Li plating and penetration in ASSLMBs. (**a**) In situ SEM observation of Li-deposition-induced crack initiation and propagation in a Li/LPSC/Li cell, revealing the progressive development of a crack network, subsequent Li filling of the cracks, and the coupled evolution toward electrolyte penetration and short circuit. (**a**) Reproduced with permission from Ref. [176]. Copyright 2023 Elsevier Ltd.; and reproduced from Ref. [112] under the CC BY-NC-ND 4.0 license. Copyright 2020, the authors. Published by Elsevier Inc. (**b1**–**b4**) Direct visualization of Li penetration across complementary length scales: (**b1**,**b2**) operando OM combined with cross-sectional FIB–SEM analysis of an in-plane Li/LLZO configuration, resolving branched Li propagation and crack-assisted penetration through the ceramic electrolyte; and (**b3**,**b4**) cross-sectional in situ TEM of a Li/LLZO/CC nanobattery, revealing mechanically confined Li accumulation, interfacial stress buildup, Li eruption, and associated crack formation in LLZO. (**b1**,**b2**) Reproduced from Ref. [112] under the CC BY-NC-ND 4.0 license. Copyright 2020, the authors. Published by Elsevier Inc. (**b3**,**b4**) Reproduced from Ref. [177] under the CC BY 4.0 license. Copyright 2022, the authors. (**c**) Operando 3D focal-variation microscopy of an anode-free Cu/LLZO/Li cell, correlating

Li nucleation and blister formation at the CC interface with simultaneously measured electrochemical responses and interfacial deformation. (**c**) Reproduced with permission from Ref. [178]. Copyright 2022 Elsevier Inc. (**d**) Correlative operando OM and DFXM of Li penetration in single-crystalline LLZTO, mapping lattice misorientation, local strain, and dislocation accumulation around the Li-dendrite tip and revealing the coupling among Li deposition, stress evolution, crystal-defect formation, and fracture. (**d**) Reproduced from Ref. [135] under the CC BY 4.0 license. Copyright 2024, the authors.

To overcome the difficulty of observing Li dendrites growing through the thickness of a conventional solid-state cell, Kazyak et al. [112] designed an in-plane configuration in which two Li electrodes were deposited on the same surface of an LLZO ceramic plate. This geometry forced Li to propagate laterally along the electrolyte surface, as shown in Figure 9(b1,b2). Operando OM, combined with subsequent FIB-SEM cross-sectional analysis, enabled both real-time observation and 3D structural characterization of Li penetration. The authors first confirmed that the in-plane configuration showed cross-sectional evolution similar to that of conventional through-thickness LLZO cells, demonstrating that the platform could reproduce the essential features of practical Li penetration. Li propagated mainly in a branched morphology, particularly at high current density. Cross-sectional FIB-SEM analysis showed that this propagation occurred primarily through mechanically driven cracking. Li entered pre-existing or newly formed cracks, generated local stress at the crack tip, and promoted further crack growth and Li filling. The combination of operando optical imaging and 3D cross-sectional analysis therefore provides a multiscale method for resolving the propagation of Li through ceramic SEs.

At smaller length scales, nanobattery platforms combined with in situ TEM provide direct access to Li deposition at buried interfaces. Gao et al. [177] constructed a Li | LLZO | CC nanobattery and used cross-sectional in situ TEM to directly visualize Li-deposition kinetics and the resulting mechanical failure at the Li/SE interface, as shown in Figure 9(b3,b4). The mechanical boundary conditions were varied by changing the CC, including a thick Cu probe, a thin W probe, and a carbon nanotube. This enabled the effects of constraint and deposition rate on interfacial evolution to be systematically examined. Under strong mechanical confinement and rapid deposition, Li accumulated quickly within the restricted space and generated a sharp increase in interfacial stress, eventually producing a "Li eruption." At the same time, vertical cracks formed in LLZO. Li subsequently filled these cracks and drove them into the subsurface region. Coupled electro-chemo-mechanical simulations suggested that the hydrostatic pressure within the confined Li during eruption could reach the gigapascal range and, in some cases, approach 10 GPa. Such pressures are sufficient to exceed the theoretical strength of LLZO and induce cleavage even in crystals without obvious pre-existing defects. This study demonstrates that in situ TEM can directly resolve nanoscale stress concentration and crack propagation at buried interfaces, providing critical evidence for understanding mechanical failure of SEs.

Operando X-ray microscopy (XRM) is particularly advantageous for visualizing buried morphological evolution without disassembling the cell. Using synchrotron XCT, researchers have tracked the 3D evolution of Li metal during plating and stripping in real time [179]. The reconstructed volumes revealed pronounced current-density-dependent changes in Li morphology and connectivity, including the development of rapidly growing fractal Li structures associated with electrochemical instability and eventual cell failure. Such measurements demonstrate that operando XRM can resolve not only the final location of deposited Li but also the temporal evolution of its nucleation, growth, connectivity, and loss of reversibility.

To eliminate the influence of the initial morphology of a Li-metal anode, Kazyak et al. [178] constructed an anode-free Cu | LLZO | Li cell and combined controlled stack pressure with 3D focal-variation microscopy. This approach enabled operando 3D observation of surface morphology at the CC during Li deposition, as shown in Figure 9c. The method simultaneously recorded electrochemical signals, including voltage and impedance, and correlated them with changes in deposition morphology. During the initial stage, Li nucleated preferentially at local surface defects. As the deposited capacity increased, Li volume expansion deformed the interface and produced observable Li blisters. Changes in the voltage response corresponded directly to the mechanical evolution of the interface, indicating that abnormal voltage features may serve as indicators of interfacial failure in ASSLMBs. This work highlights the value of operando 3D topographic imaging for revealing the coupling between Li deposition and stress evolution in anode-free solid-state cells.

Understanding the role of crystal defects during Li penetration requires information on internal strain and dislocation structures within the electrolyte. Yildirim et al. [135] combined operando OM with DFXM to examine dislocation behavior near a Li-dendrite tip in single-crystalline LLZTO, as shown in Figure 9d. DFXM can resolve crystal orientation, local strain, and defect distributions across nanometer-to-micrometer length scales. 3D strain imaging around the dendrite revealed clear lattice misorientation, highly strained regions, and dislocation accumulation near the dendrite tip. These observations show that local stress generated by Li deposition can alter the defect structure of the SE and may subsequently facilitate crack propagation and Li penetration. This work provided direct structural evidence at the crystal-defect scale for a coupled sequence of Li deposition, stress accumulation, dislocation formation, and fracture.

Overall, the development of in situ SEM, OM, TEM, 3D microscopy, and DFXM has enabled Li plating and stripping to be studied dynamically over multiple length scales, from macroscopic morphology and buried-interface evolution to crystal defects. These techniques not only reveal the pathways of dendrite formation and penetration but also establish direct links among deposition behavior, stress evolution, and SE failure.

5.3. Characterization of Stress and Mechanical Behavior

Electro-chemo-mechanical coupling in ASSLMBs is expressed through the generation, transfer, redistribution, and release of stress during Li plating and stripping, changes in interfacial contact, and electrode volume variation. Quantitative operando measurement of stress and mechanical behavior is therefore required to understand the relationships among stack-pressure evolution, interfacial degradation, and structural transformations. Recent developments in operando mechanical characterization have progressed from measurement of the overall force or pressure of the cell to local stress sensing and spatial visualization of internal stress fields. These methods provide important tools for understanding electro-chemo-mechanical coupling in ASSLMBs.

Operando stack-pressure monitoring is among the most widely used methods for characterizing mechanical response. A typical experimental setup is shown in Figure 10a. A force sensor integrated outside the cell records changes in stack pressure during cycling and thereby provides the overall stress evolution of the cell. Han et al. [180] used this method to study pressure evolution in ASSLMBs containing alloy anodes. The magnitude of the pressure change was directly related to the amount of Li transferred. Sb produced the largest pressure variation, approximately 2.25 MPa, whereas Sn and Si generated smaller changes. The pressure response also depended on electrode architecture and particle size. Composite electrodes and foil electrodes exhibited different pressure evolution, while nanoscale Si reduced stress accumulation by filling internal pores within the electrode. Analysis of the pressure-change rate, dP/dt, also enabled phase transformations in the

electrode to be identified sensitively. Operando pressure monitoring can therefore provide more than a measure of the overall mechanical response. It can also serve as an indirect probe of structural and phase evolution within electrode materials.

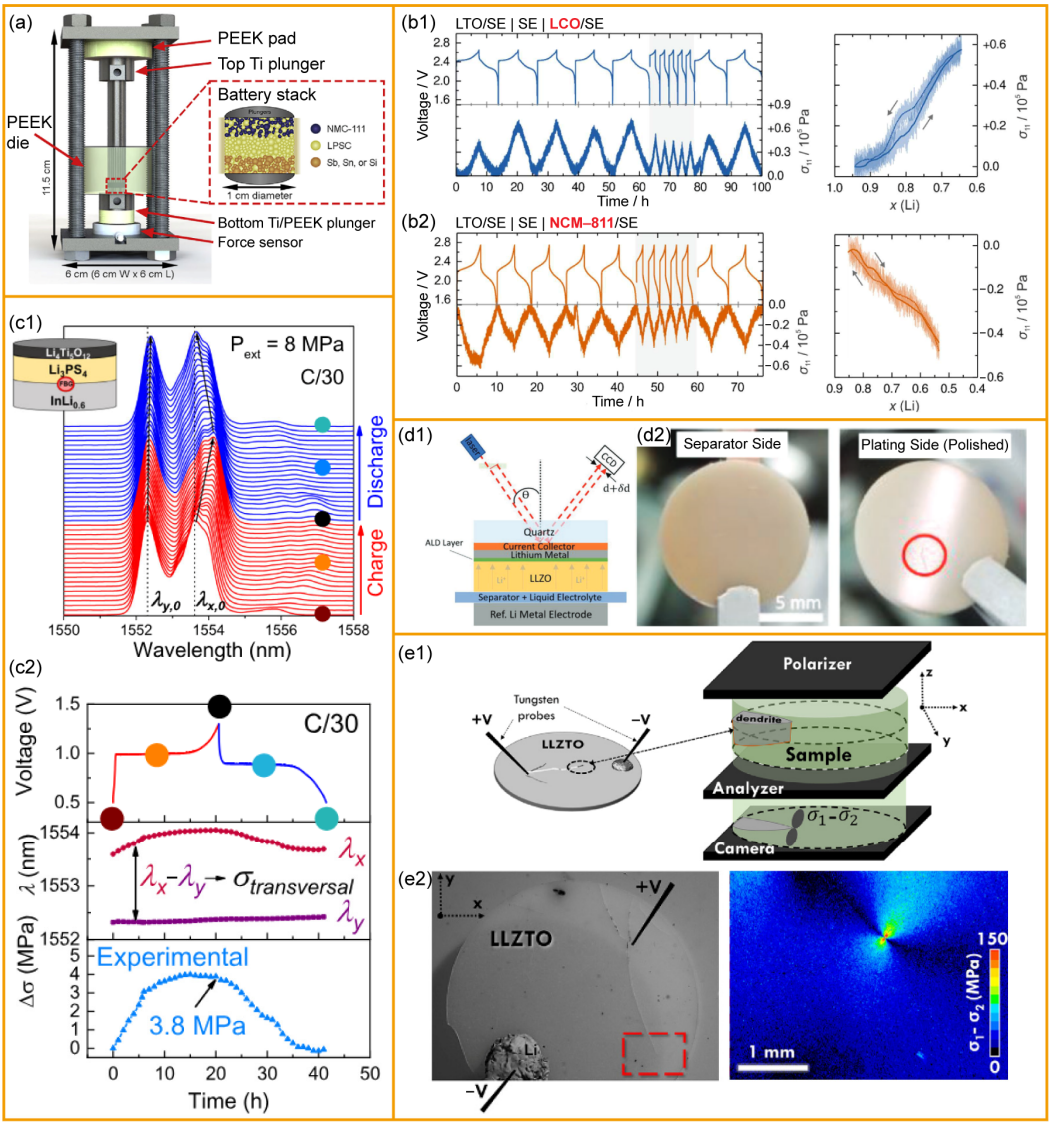


Figure 10. Operando characterization of stress and mechanical evolution in ASSLMBs. (**a**,**b**) Operando stack-pressure monitoring of the cell-level mechanical response during electrochemical cycling, including the experimental configuration for simultaneous pressure and electrochemical measurements and representative pressure evolution associated with reaction-induced volume changes in different electrode materials and architectures. (**a**) Reproduced with permission from Ref. [180]. Copyright 2021 Elsevier Inc. (**b1**,**b2**) Reproduced with permission from Ref. [13]. Copyright 2018 The Royal Society of Chemistry. (**c1**,**c2**) Local interfacial stress measurement using an embedded FBG sensor, showing stress-induced splitting of the Bragg reflection into two polarized peaks and the corresponding reversible evolution of interfacial stress during electrochemical cycling. (**c1**,**c2**) Reproduced from Ref. [166] under the CC BY 4.0 license. Copyright 2022, the authors. (**d1**,**d2**) In situ optical-curvature measurement of stress generated during Li deposition, illustrating the conversion of substrate bending into the internal pressure of the growing Li layer and the abrupt mechanical response associated with SE cracking and Li penetration. (**d1**,**d2**) Reproduced with permission from Ref. [181]. Copyright 2022 Wiley-VCH GmbH. (**e1**,**e2**) Operando photoelastic visualization of dendrite-induced stress fields in a transparent SE, showing the experimental configuration for optical retardation measurements and the spatially resolved stress concentration around a propagating Li-dendrite tip. (**e1**,**e2**) Reproduced with permission from Ref. [147]. Copyright 2023 Elsevier Inc.

Koerver et al. [13] further used operando pressure monitoring to compare stress accumulation in different all-solid-state cell configurations, as shown in Figure 10(b1,b2). When the near-zero-strain anode LTO was used, the overall pressure response was governed mainly by the cathode volume change. Cells containing LCO showed a positive pressure change, whereas those containing NCM showed a negative change. When Li metal or graphite, both of which undergo larger dimensional changes, was used as the anode, the cycling-induced stress increased by approximately one order of magnitude compared with cathode-dominated cells. Operando pressure monitoring can therefore distinguish the mechanical contributions of different electrode materials and provide a direct means of comparing stress evolution among cell chemistries.

External force sensors, however, measure only the average mechanical response of the entire cell. They cannot resolve local stresses near internal interfaces or within individual electrodes. Research has therefore increasingly shifted toward operando measurement of local stress inside the cell.

Blanquer et al. [166] developed a non-invasive operando stress-monitoring method based on Fiber Bragg grating (FBG) sensors. The FBG sensor was embedded within an electrode or placed on its surface. Electrode volume changes strained the optical fiber and shifted the Bragg wavelength (λ_B). After correcting for temperature and external pressure, the wavelength shift could be converted into a local stress response. As shown in Figure 10(c1), the operando FBG spectra collected from an $InLi_x$ | LPS | LTO cell cycled at C/30 (5.83 $mA \cdot g^{-1}$) under an external pressure of 8 MPa exhibit two distinct reflection peaks. When the FBG sensor is positioned at the electrode/SE interface, the non-uniform stress acting on the optical fiber induces birefringence, causing the original reflection peak to split into two polarized peaks (λ_x and λ_y). The wavelength separation ($\lambda_x - \lambda_y$) can be directly correlated with the transverse interfacial stress, corresponding to the axial stress of the cell, with a maximum value of approximately 3.8 MPa. By continuously tracking the evolution of λ_x and λ_y during charge and discharge, the internal stress evolution was quantitatively determined (Figure 10(c2)). The measured stress evolution showed excellent reversibility with the electrochemical response, highlighting the superior sensitivity of local stress monitoring compared with conventional external pressure measurements.

Notably, in symmetric cells, the volume changes of the two electrodes can compensate for each other at the cell level, causing the external force sensor to detect almost no net change. An FBG positioned at one electrode interface, however, still recorded a reversible stress variation of approximately 14–15 MPa during cycling of that electrode. FBG sensing therefore overcomes the averaging limitation of conventional external pressure measurements and enables quantitative operando monitoring of local stresses inside ASSLMBs. This technique provides a powerful tool for directly probing localized electro-chemo-mechanical responses and elucidating interfacial degradation mechanisms during battery operation.

In addition to direct stress sensing, internal stress can be inferred from deformation of a substrate or cell component. Cho et al. [181] developed an in situ optical-curvature platform, with the measurement principle illustrated in Figure 10(d1). The method monitored the curvature of a quartz substrate during Li deposition and converted the bending response into the internal stress of the growing Li layer. As deposition proceeded, pressure accumulated within the Li metal. At low current density, the curvature eventually reached a steady value corresponding to an internal pressure of approximately 0.1–0.2 MPa, close to the yield strength of Li metal. When the cell short-circuited, the curvature signal changed abruptly. This event corresponded closely to the formation of cracks inside the LLZO electrolyte, as shown in Figure 10(d2). Post-mortem microscopy further revealed that Li propagated mainly along grain boundaries and formed a characteristic web-like penetra-

tion network. In situ curvature measurement can therefore monitor stress accumulation in real time and may also provide an early warning of mechanical failure in the SE.

To spatially resolve internal stress fields, Athanasiou et al. [147] developed an operando imaging method based on photoelasticity, with the experimental configuration shown in Figure 10(e1). When a transparent material is stressed, its refractive index becomes anisotropic and introduces a phase delay between orthogonal polarization components. Measuring this optical retardation allows the principal stress difference (σ_1–σ_2) to be calculated and the 2D stress field to be reconstructed. The method was applied to Li-dendrite growth in an LLZTO SE. Following polarization of the metal electrode and Li deposition, the stress distribution near the dendrite tip was directly imaged, as shown in Figure 10(e2). A pronounced stress concentration developed at the dendrite tip, and the measured field closely matched the prediction of an elastic-fracture-mechanics model for a pressurized crack. This work provided the first direct visualization of a dendrite-induced stress field inside an ASSLMB. Compared with conventional force measurements, photoelasticity extends stress characterization from measurement at a single location to full-field imaging. It can quantify local stress magnitudes while also revealing the positions and propagation paths of stress concentrations. Photoelastic imaging therefore offers a powerful operando method for studying dendrite propagation, cathode-particle cracking, interfacial contact loss, and other electro-chemo-mechanical failure processes.

Overall, stress characterization in ASSLMBs has developed from global pressure monitoring to local stress measurement and, more recently, full-field stress visualization. Operando force sensors capture the overall mechanical response of the cell, FBG sensors provide quantitative measurements of local internal stress, and optical-curvature and photoelastic methods reveal the evolution and spatial distribution of mechanical deformation. Although it remains difficult to obtain the complete 3D stress evolution associated with electro-chemo-mechanical failure inside an operating ASSLMB, optical and other indirect characterization methods already provide increasingly accurate operando measurements of stress and mechanical behavior. These techniques are essential for establishing quantitative relationships among electrochemical reactions, structural evolution, and mechanical failure.

6. Modification Strategies for Mitigating Electro-Chemo-Mechanical Coupling Failure

Electro-chemo-mechanical failure in ASSLMBs arises from the mutual reinforcement of reaction-induced volume changes, stress accumulation, and interfacial degradation. These coupled processes eventually lead to crack propagation, contact loss, impedance growth, and dendrite-induced short circuiting. Optimizing a single material property is therefore unlikely to address these problems fundamentally. Instead, coordinated design is required across the material, interface, electrode, and cell levels. This section discusses modification strategies for cathode materials, interface engineering, and other electro-chemo-mechanical approaches. Particular attention is given to their roles in relieving stress concentrations, maintaining interfacial contact, regulating Li deposition, and improving the long-term cycling stability of ASSLMBs.

6.1. Cathode-Material Modification

During prolonged cycling, cathode materials repeatedly undergo Li insertion and extraction, resulting in lattice distortion, volume change, and local stress accumulation. These electrochemically induced mechanical responses can cause internal cracking and particle fracture, degrade contact at the cathode/SE interface, block ion-transport pathways, and isolate parts of the cathode from electrochemical reaction. Rational control of the

intrinsic structure, interfacial stability, and chemo-mechanical response of cathode materials is therefore essential for mitigating electro-chemo-mechanical degradation.

Current cathode-modification strategies can be broadly divided into three categories: interfacial stabilization, composite-electrode design, and regulation of the intrinsic stress response. Surface coatings and artificial interphases can suppress side reactions between the cathode and SE while improving the retention of contact during cycling. Composite cathodes with both high ionic conductivity and mechanical compliance can reduce porosity, homogenize Li-ion transport, and accommodate cycling-induced strain. More recently, active control of crystallographic orientation and texture has emerged as a means of tailoring the stress response of cathodes, reducing the need for large external stack pressures and improving long-term stability.

6.1.1. Cathode Surface Coatings and Interfacial Stabilization

Surface coating is a relatively simple and cost-effective approach for improving cathode stability. An artificial protective layer separates the cathode from the SE, suppresses interfacial side reactions, and can also improve the mechanical integrity of the particle and interface during cycling. Although surface coatings can suppress interfacial side reactions and improve chemical compatibility, excessively thick or poorly conductive coatings may increase Li-ion transport resistance and reduce active-material utilization. Therefore, coating composition and thickness must be optimized to balance interfacial protection against kinetic penalties. Zheng et al. [109] prepared LNO-coated NMC811 and systematically evaluated its electrochemical performance. As shown in Figure 11(a1), the LNO@NMC811 cathode exhibited substantially better cycling stability than uncoated NMC811. It delivered an initial discharge capacity of 133 $mAh \cdot g^{-1}$ and retained 116 $mAh \cdot g^{-1}$ after 200 cycles, together with a high Coulombic efficiency. In contrast, the capacity of uncoated NMC811 rapidly decreased from 110 to only 6 $mAh \cdot g^{-1}$. The LNO layer served not only as a chemical barrier that suppressed interfacial side reactions, including oxidation of the sulfide electrolyte, but also as a mechanical reinforcement for the cathode particles. After cycling, uncoated NMC811 showed severe fragmentation and extensive internal cracking. These cracks obstructed Li-ion diffusion and isolated active regions. The coated particles, by comparison, exhibited a higher fracture strength and a crack-volume fraction of only 0.058%. The coating also promoted a more uniform Li-ion distribution and reduced chemical and structural heterogeneity during cycling. LNO coating therefore mitigated electro-chemo-mechanical degradation through three complementary effects: suppression of interfacial reactions, improvement of particle mechanical integrity, and homogenization of Li-ion transport.

In addition to conventional dry solid-state and wet-chemical coating methods, thin-film deposition techniques have recently enabled more precise control overcoating thickness and interfacial structure. Cheng et al. [182] used aerosol deposition to form a Li_3BO_3-coated LCO film on an Al-doped LLZO substrate at RT, as shown in Figure 11(a2). Li_3BO_3 acted as a Li-ion-conducting solder. During heat treatment, it softened and filled the interfacial gaps, improving contact between LCO particles and the LLZO substrate and lowering the interfacial impedance. Optimization of this interface substantially improved the performance of the Li/LLZO/LCO cell. The study also showed that mechanical degradation of the interface, particularly crack formation, was a major cause of capacity fading. Interfacial solder materials that combine high Li-ion conductivity with mechanical adaptability may therefore be valuable for maintaining low resistance and structural continuity during long-term cycling.

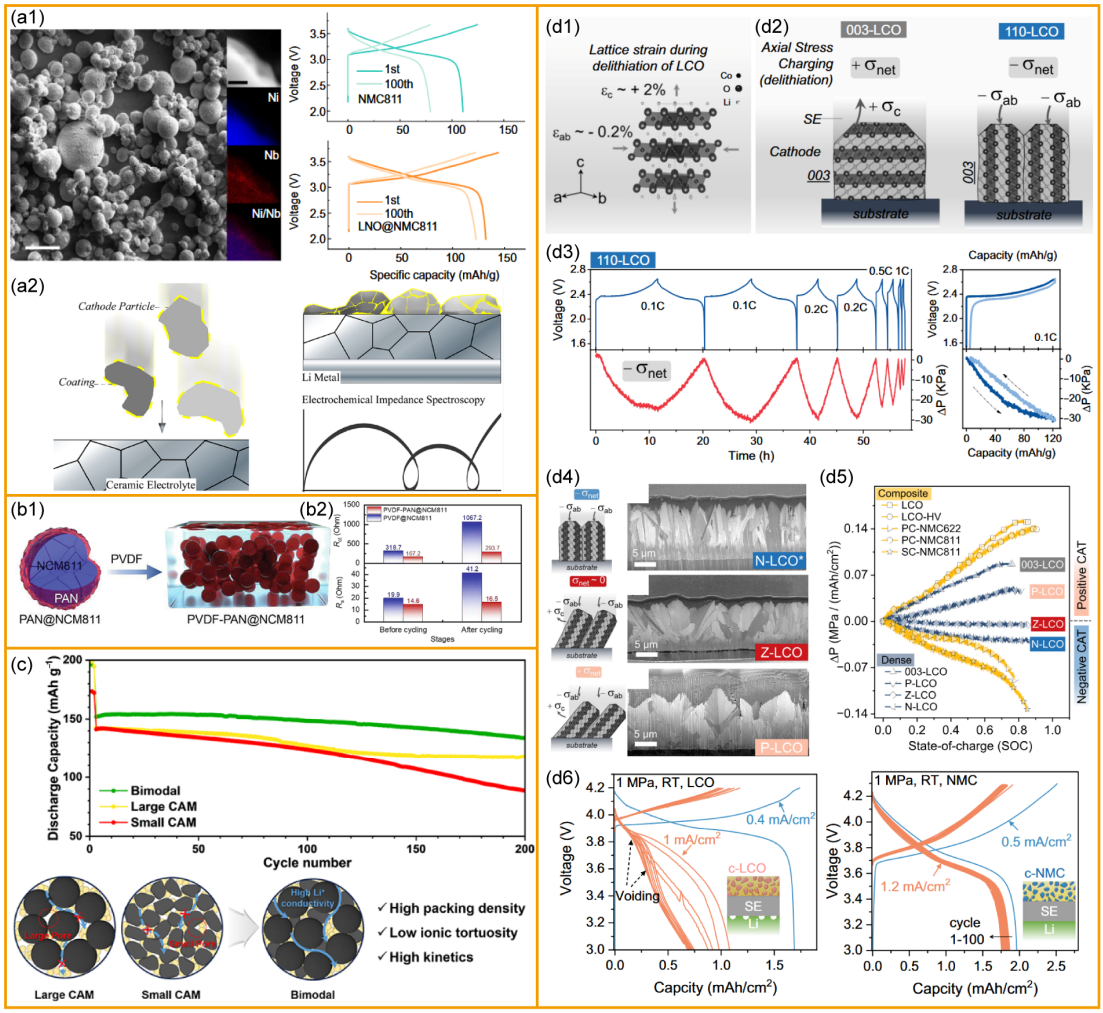


Figure 11. Cathode engineering strategies for mitigating electro-chemo-mechanical degradation in ASSLMBs. (**a1**,**a2**) Surface-coating strategy for stabilizing Ni-rich layered oxide cathodes, showing the improved cycling performance of LNO-coated NMC811 and the suppression of cycling-induced particle cracking, structural fragmentation, and reaction heterogeneity through simultaneous interfacial protection and mechanical reinforcement. (**a1**) Reproduced from Ref. [109] under the CC BY 4.0 license. Copyright 2025, the authors. Published by the American Association for the Advancement of Science. (**a2**) Reproduced with permission from Ref. [182]. Copyright 2023 Elsevier Ltd. (**b1**,**b2**) Mechanically compliant polymer-assisted composite-cathode design using a PVDF–PAN framework, illustrating homogenized Li-ion transport, accommodation of cycling-induced strain, improved structural integrity, and reduced interfacial resistance and polarization during prolonged cycling. (**b1**,**b2**) Reproduced with permission from Ref. [183]. Copyright 2023 Elsevier B.V. (**c**) Bimodal particle-size engineering of composite cathodes by combining large polycrystalline NCWA with small single-crystalline NCM particles, enabling denser particle packing, reduced porosity and ionic tortuosity, improved cathode/SE contact, and enhanced electrochemical kinetics and mechanical integrity. (**c**) Reproduced with permission from Ref. [184]. Copyright 2026 American Chemical Society. (**d1**–**d6**) Crystallographic texture engineering for active regulation of cathode stress, illustrating anisotropic lattice deformation of LCO during delithiation, orientation-dependent compressive and tensile pressure responses, tailoring of the magnitude and direction of electrode stress through controlled grain orientation, and improved cycling stability of stress-regulated ASSLMBs under low external stack pressure. (**d1**–**d6**) Reproduced from Ref. [185] under the CC BY-NC-ND 4.0 license. Copyright 2025, the authors.

6.1.2. Composite-Cathode Design for Stress Accommodation

Beyond surface coatings, composite-cathode architectures that combine rapid ion transport with mechanical compliance offer another route to reducing stress concentrations

and preserving interfacial contact. Polymer components in such electrodes must, however, simultaneously provide Li-ion transport and mechanical regulation, and these requirements are not always compatible.

Jiang et al. [183] combined the relatively high ionic conductivity of polyacrylonitrile (PAN) with the mechanical flexibility of polyvinylidene fluoride (PVDF) to construct a composite NCM811 cathode with a PAN inner layer and a PVDF outer layer, denoted PVDF–PAN@NCM811, as shown in Figure 11(b1). After 200 cycles at 4.5 V and 0.1C, the solid-state cell containing PVDF–PAN@NCM811 retained a capacity of 146.2 $mAh \cdot g^{-1}$, substantially higher than that of the cathode containing PVDF alone. It also showed a more stable voltage profile and lower polarization. EIS, shown in Figure 11(b2), revealed a lower initial R_{int} and slower resistance growth during cycling. These results indicate that the PAN-rich inner layer improved ionic contact and stabilized the cathode/electrolyte interface. The cycled electrode also retained a more intact structure, confirming the stress-buffering effect of the polymer matrix. Both simulation and experiment showed that PAN primarily promoted homogeneous Li-ion transport within the composite cathode, whereas the more compliant PVDF outer layer accommodated cycling-induced strain. Their combined functions reduced transport heterogeneity and suppressed structural degradation.

A bimodal particle-size distribution can also improve the chemo-mechanical integrity of composite cathodes. Oh et al. [184] showed that cathode performance is strongly influenced not only by material chemistry but also by particle size and single-crystalline or polycrystalline morphology. Small single-crystalline NCM particles were used to fill the voids between larger polycrystalline $LiNi_{0.88}Co_{0.10}W_{0.01}Al_{0.01}O_2$ (NCWA) particles, while LPSC provided ionic conduction and mechanical support. The resulting densely packed bimodal cathode, shown in Figure 11c, had a porosity 35–58% lower than that of comparable unimodal electrodes. When the ratio of large polycrystalline NCWA to small single-crystalline NCM was optimized to 7:3, the cathode delivered the highest discharge capacity at 0.5C and maintained strong performance at 2–3C. After 200 cycles, the capacity retention reached 87.8%, markedly higher than that of conventional unimodal cathodes. The higher packing density and improved capacity utilization also resulted in greater volumetric energy density. This strategy demonstrates that matching particles of different sizes and structural types can produce a denser electrode network, reduce porosity and ionic tortuosity, and increase the effective ionic conductivity. Bimodal architectures therefore provide a useful route to simultaneously improving electrochemical kinetics and mechanical integrity.

6.1.3. Cathode Microstructural Design and Dynamic Cell Volume Compensation

Although coatings and composite-electrode design can improve interfacial stability, continuous volume changes of cathode particles still generate local stress during prolonged or high-rate cycling. These stresses can promote void formation, reduce contact area, and increase electrochemical polarization. Regulating the intrinsic electro-chemo-mechanical response through crystallographic orientation and texture therefore offers a more direct means of controlling stress.

Moradi et al. [185] prepared dense LCO cathodes with controlled crystallographic orientation using electrodeposition. LCO undergoes strongly anisotropic lattice deformation during delithiation, expanding by approximately 2% along the c-axis while contracting by approximately 0.2% within the ab plane, as illustrated in Figure 11(d1). Based on this anisotropy, the authors prepared two LCO textures: 003-oriented LCO with the c-axis normal to the substrate and 110-oriented LCO with the ab plane aligned parallel to the substrate, as shown in Figure 11(d2). During charging, 003-LCO generated a positive compressive pressure response of approximately 40 kPa, whereas 110-LCO produced a negative tensile

response of approximately −30 kPa. Their pressure evolution and reversibility are shown in Figure 11(d3). By further adjusting grain orientation, three distinct LCO textures were obtained, and their microstructures and delithiation-induced stress responses were compared, as shown in Figure 11(d4,d5). Crystallographic texture could strengthen, eliminate, or even reverse the pressure response generated by the cathode.

The authors then constructed LCO- and NMC-based ASSLMBs and compared their performance under a low stack pressure of 1 MPa, as shown in Figure 11(d6). A cell containing a negative-stress composite NMC622 cathode cycled for more than 200 cycles at an areal capacity of 5 mAh·cm^{-2} and a current density of 1.25 mA·cm^{-2} without an interlayer at the Li/electrolyte interface, retaining 99% of its capacity. The negative-stress cathode promoted uniform Li deposition and generated a mechanical response favorable for closing interfacial voids during stripping. A positive-stress cathode, in contrast, could worsen nonuniform Li deposition and facilitate void formation and growth. This approach departs from the conventional strategy of relying on large external stack pressures. By actively designing the intrinsic stress response of the cathode, stable operation can be achieved under much lower external pressure, providing a new direction for practical ASSLMB design.

The severe mechanical degradation arising from the enormous volume change (~300%) of Si anodes remains one of the fundamental obstacles to the practical implementation of all-solid-state batteries. To address this challenge, Hu et al. [186] developed a stress-compensated Si–S all-solid-state battery based on a dynamic volume compensation concept. Rather than relying solely on material-level modifications, this approach exploits the complementary volume evolution of silicon anodes and sulfur cathodes during lithiation and delithiation, enabling spontaneous compensation of cell-level deformation throughout battery operation. In contrast to Li–S half cells, which exhibit a pronounced increase in interfacial impedance upon discharge due to deformation-induced contact deterioration, the Si–S full cell maintained relatively stable charge-transfer and solid-state diffusion resistances during cycling. These results indicate that the dynamic volume compensation design effectively preserves intimate solid–solid contact and continuous ion-transport pathways. Overall, this work highlights that rational cell-level structural design, through the synergistic coupling of the electrochemical and mechanical responses of alloy-type anodes and conversion-type cathodes, can effectively mitigate stress accumulation in all-solid-state Si–S batteries. This dynamic volume compensation concept provides a scalable cell-design paradigm for developing next-generation all-solid-state batteries with high energy density, long cycle life, and enhanced safety.

6.2. Interface Engineering

Interfacial stability directly governs Li-ion transport, charge-transfer kinetics, and mechanical integrity in ASSLMBs. Unlike a liquid electrolyte, which can wet and refill newly formed gaps, a rigid solid–solid interface cannot readily maintain conformal contact. Interfacial voids, local stress concentrations, and nonuniform ion transport can therefore develop easily. Cycling-induced volume changes, interfacial reactions, and Li plating/stripping further destabilize these interfaces, leading to resistance growth, dendrite-induced short circuiting, and capacity fading. Controlling interfacial chemistry, structure, and mechanical state is consequently a central strategy for mitigating electro-chemo-mechanical failure. Current approaches include surface cleaning and reconstruction, construction of functional internal interfaces, external stress engineering, and artificial interlayer design.

6.2.1. Surface Cleaning and Reconstruction

Garnet-type LLZO combines high Li-ion conductivity with relatively good chemical stability and is regarded as a promising SE. Its practical use is nevertheless limited by poor wettability with Li metal and a high Li/LLZO R_{int}, which commonly exceeds

100 Ω·cm^2. Sharafi et al. [187] developed an interfacial treatment based on wet polishing, high-temperature annealing, and preheating, without introducing an additional coating, as shown in Figure 12a. Air-exposed LLZO was found to develop a surface contamination layer composed mainly of LCO and LiOH. This layer prevented direct contact between Li metal and LLZO and hindered Li-ion transport across the interface. Dry-polished LLZO remained largely covered by carbonate species, whereas wet polishing reduced some of the carbonate but produced a LiOH-rich surface. Mechanical polishing alone was therefore insufficient to remove the contamination. Annealing the wet-polished LLZO under an inert atmosphere at temperatures up to 500 °C removed LiOH and reduced the carbonate content, producing a surface composition closer to that of bulk LLZO. After wet polishing, annealing at 500 °C, and preheating at 175 °C, the Li/LLZO R_{int} decreased to approximately 2 Ω·cm^2, lower than that of some conventional liquid-electrolyte interfaces. This study demonstrates that control of surface chemistry alone can markedly improve solid–solid contact and interfacial transport without requiring an additional protective layer.

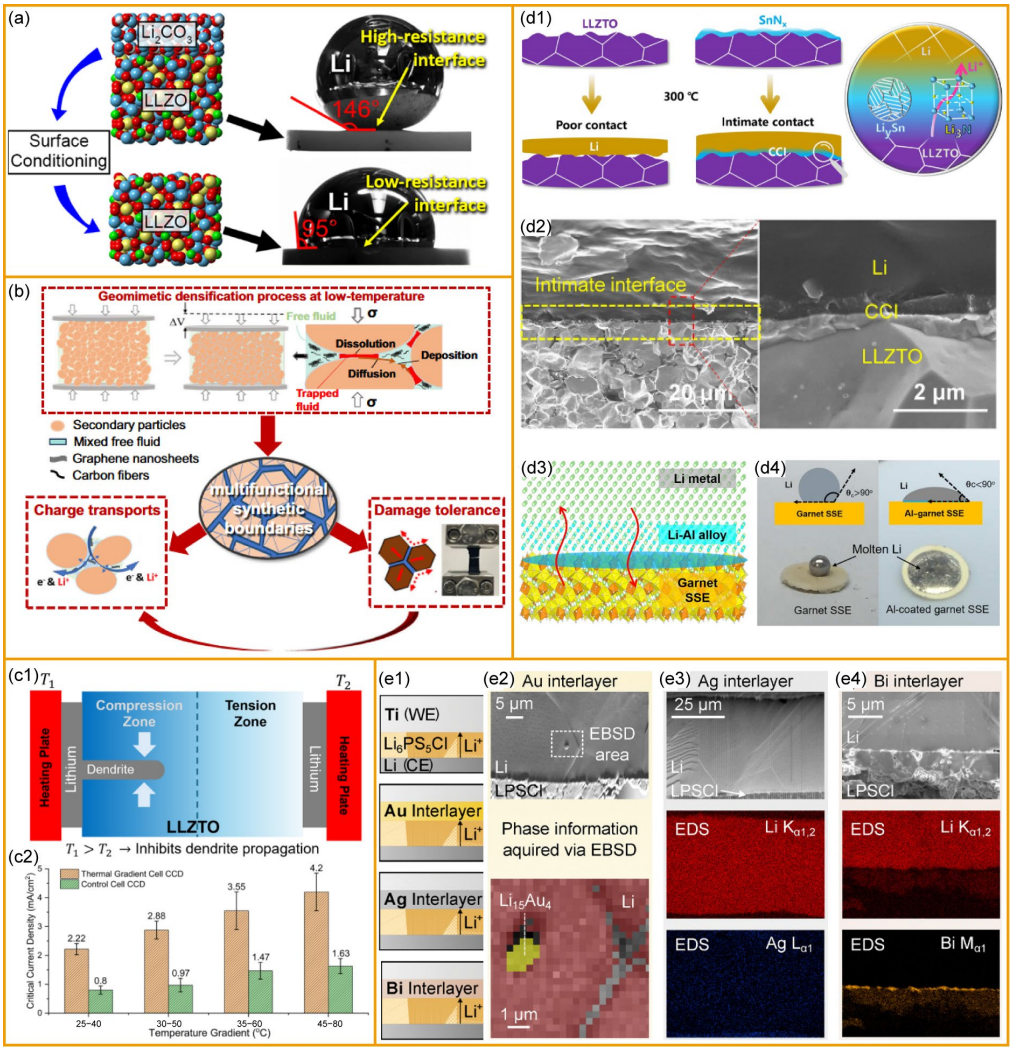


Figure 12. Interfacial engineering strategies for mitigating electro-chemo-mechanical degradation in ASSLMBs. (**a**) Surface cleaning and reconstruction of garnet-type LLZO, illustrating the removal of LCO/LiOH surface contamination through wet polishing, high-temperature annealing, and Li preheating to improve Li wettability, restore intimate Li/LLZO contact, and reduce interfacial resistance. (**a**) Reproduced with permission from Ref. [187]. Copyright 2017 American Chemical Society. (**b**) Functional interface engineering within thick composite cathodes through transient-liquid-assisted densification, showing stress-driven redistribution and redeposition of soluble components into interparticle voids to

form continuous secondary boundaries that enhance particle bonding, mechanical toughness, and 3D ion/electron transport. (**b**) Reproduced from Ref. [188] under the CC BY 4.0 license. Copyright 2025, the authors. (**c1**,**c2**) External stress engineering using a through-thickness temperature gradient across LLZTO, generating a residual compressive-stress field that reduces the Mode-I crack-driving force for Li-filled defects and thereby increases the critical current density and cycling stability against Li-dendrite penetration. (**c1**,**c2**) Reproduced with permission from Ref. [189]. Copyright 2025 Elsevier Inc. (**d1**–**d4**) Artificial interlayer strategies for stabilizing the Li/garnet interface, including the formation of a conductive Li_ySn/Li_3N composite interface from a SnN_x precursor and an ultrathin Li–Al alloy interlayer, both of which improve Li wettability, homogenize interfacial contact, and substantially reduce interfacial resistance. (**d1**,**d2**) Reproduced with permission from Ref. [190]. Copyright 2020 Wiley-VCH GmbH. (**d3**,**d4**) Reproduced from Ref. [191] under the CC BY-NC 4.0 license. Copyright 2017, the authors. Published by the American Association for the Advancement of Science. (**e1**–**e4**) Regulation of Li deposition microstructure using Au, Ag, and Bi interlayers, illustrating how interlayer chemistry modifies Li grain size, crystallographic texture, lattice strain, and grain-growth behavior, thereby providing an additional route to controlling electro-chemo-mechanical stability at the Li/SE interface. (**e1**–**e4**) Reproduced from Ref. [192] under the CC BY 3.0 license. Copyright 2026, the authors. Published by the Royal Society of Chemistry.

6.2.2. Functional Interfaces Within Composite Cathodes

The complex multiphase interfaces within composite cathodes are also critical to battery performance. Contact among the cathode material, SE, and electronic-conduction network determines ion and electron transport and influences how mechanical strain is distributed during cycling.

Inspired by the densification of geological minerals, Nie et al. [188] developed a transient-liquid-assisted densification process to form multifunctional secondary boundaries in thick composite electrodes, as shown in Figure 12b. Under uniaxial pressure, moderate heating, and a small amount of transient liquid such as dimethylformamide or acetone, localized solvothermal environments formed between ceramic particles. Soluble components, including LiTFSI and PVDF-co-hexafluoropropylene (HFP), dissolved from highly compressed regions and were transported by stress-driven mass migration into interparticle voids, where they redeposited as a polyionic-liquid gel secondary phase. This process lowered the activation energy and temperature required for densification and avoided thermal degradation of organic components. The continuous secondary-boundary phase strengthened bonding between inorganic particles and the organic interphase, increased the toughness and damage tolerance of the thick electrode, and formed a 3D ion- and electron-transport network. Transient-liquid-assisted densification therefore offers a potential route to mechanically robust, high-loading electrodes and may be compatible with scalable processing of large-format ASSLMBs.

Cheng et al. [193] further demonstrated that introducing an ionic liquid into the cathode to construct a non-flowable quasi-solid-state composite cathode is an effective strategy for overcoming the large interfacial resistance between ceramic SEs and cathode materials. The ionic liquid acts as an interfacial wetting agent within the composite cathode, significantly improving the interparticle contact between LCO particles as well as the interfacial contact between LCO and the Al-doped LLZO electrolyte. This study confirmed that the appropriate incorporation of ionic liquids provides a simple, effective, and manufacturing-compatible approach to substantially reducing the cathode interfacial resistance in ASSLMBs.

6.2.3. External Stress Engineering

Since interfacial failure in ASSLMBs is closely associated with mechanical evolution, deliberate control of the stress state through external conditions can also be regarded as a

form of interface engineering. Increasing stack pressure improves solid–solid contact and suppresses stripping-induced void formation; however, excessive pressure may promote Li penetration, fracture brittle SEs, complicate cell packaging, and reduce the practical gravimetric and volumetric energy density. Yu et al. [189] applied a sustained through-thickness temperature gradient, ΔT, across an LLZTO garnet electrolyte and performed both unidirectional deposition and symmetric plating/stripping experiments, as shown in Figure 12(c1). The thermal gradient generated a stable residual compressive-stress field within the electrolyte, particularly near the hotter Li-plating interface. Under this gradient, the critical current density of an LLZTO symmetric cell increased by approximately a factor of three relative to an isothermal cell at the same average temperature, while the cycling life increased by more than fourfold, as shown in Figure 12(c2). From a fracture-mechanics perspective, a Li dendrite can be regarded as a pressurized internal crack. Compressive thermal stress reduces the effective Mode-I crack-driving force generated during confined Li growth, thereby increasing the resistance of the SE to crack extension. Consequently, a larger mechanical driving force is required for dendrite propagation.

This work experimentally demonstrated that residual compressive stress could suppress Li-dendrite growth and introduced thermal-gradient control as a mechanical strengthening strategy that could be combined with chemical interface engineering.

6.2.4. Artificial Interlayers

Functional interlayers are widely used to improve wettability, lower R_{int}, and regulate Li deposition in ASSLMBs. Interlayers that are lithiophilic, ionically conductive, and mechanically stable can reduce local current concentration and suppress dendritic growth.

Shi et al. [190] deposited a SnN_x layer on LLZTO by magnetron sputtering. Reaction with molten Li then formed a conductive composite interface (CCI) consisting of Li_ySn alloy and Li_3N, as illustrated in Figure 12(d1). Cross-sectional SEM of the Li/LLZTO@CCI interface, shown in Figure 12(d2), confirmed good wettability and the formation of a continuous, dense Li_ySn/Li_3N interphase. The interlayer reduced the R_{int} of a Li/LLZTO/Li symmetric cell from 4468 to 164.8 Ω, a decrease of approximately 27 times. The cell cycled stably for more than 1200 h and reached a critical current density of 1.5 $mA \cdot cm^{-2}$. Fu et al. [191] similarly introduced an ultrathin Al interlayer to form a Li–Al alloy interface, as shown in Figure 12(d3). A 20 nm Al film deposited on the garnet surface reacted with molten Li and converted the initially lithiophobic LLZO surface into a lithiophilic interface, allowing Li to spread uniformly over the electrolyte, as shown in Figure 12(d4). The charge-transfer resistance of the Li/garnet interface decreased from approximately 950 to 75 $\Omega \cdot cm^{-2}$ at 20 °C and to approximately 30 $\Omega \cdot cm^{-2}$ at 60 °C, approaching values found in conventional liquid-electrolyte cells.

Interlayers also alter the microstructure of deposited Li. Becker et al. [192] systematically investigated Au, Ag, and Bi interlayers and their effects on Li morphology and crystallographic structure, as shown in Figure 12(e1–e4). Without an interlayer, Li formed large columnar grains. An Au interlayer produced $Li_{15}Au_4$ alloy particles that restricted grain growth through a Zener-pinning-like mechanism, resulting in smaller Li grains. Ag formed a Li–Ag solid solution, introduced lattice strain, and modified the surface energy of Li, thereby suppressing grain coarsening. Bi formed a Li_3Bi alloy layer and changed the deposition substrate, leading to a different evolution of Li grain orientation. These results show that interlayer chemistry governs not only R_{int} and wettability but also the microstructure of deposited Li. Evaluation of dendrite suppression should therefore consider the evolution of Li grain size, texture, and defect structure in addition to the macroscopic deposition morphology.

6.3. Other Electro-Chemo-Mechanical Strategies

Electro-chemo-mechanical failure can also be mitigated through electrolyte functionalization, mechanical regulation of CCs, and cell-level structural design. Unlike local modification of a single material or interface, these approaches focus on the interaction among ion transport, deformation, and structural integrity. Their common objective is to maintain continuous ion-transport pathways, stable interfacial contact, and a controlled stress distribution under cycling or external loading. At the material level, self-healing composite electrolytes can repair cracks and accommodate strain. At the electrode level, compliant substrates and 3D CCs can release deposition-induced stress and homogenize local current density. At the device level, helical, overlapping, wrinkled, arched, or kirigami structures can convert macroscopic deformation into reversible geometric motion, protecting brittle active layers and interfaces.

6.3.1. Self-Healing Composite Electrolytes

Conventional solid polymer electrolytes often struggle to simultaneously achieve high ionic conductivity, sufficient mechanical strength, and stable interfacial contact. Segmental motion promotes Li-ion transport but can weaken mechanical support, whereas higher crosslinking density or stiffness improves structural stability at the cost of RT conductivity. Combining polymers with complementary functions and introducing reversible dynamic bonds provides one route to balancing these properties.

Ye et al. [194] combined a self-healing polyurethane (PNPU), containing multiple hydrogen-bonding interactions with PVDF–HFP to prepare a PNPU–PVDF–HFP solid polymer electrolyte. The dynamic hydrogen-bond network increased both strength and ductility and could reform after local damage. The modified electrolyte showed a denser microstructure and greater ability to accommodate deformation, as shown in Figure 13(a1–a3), helping to maintain contact with both electrodes. PNPU also increased the fraction of amorphous polymer and introduced oxygen-containing groups that provided additional coordination and migration sites for Li-ion. As a result, the RT ionic conductivity increased and the activation energy for ion transport decreased, as shown in Figure 13(a4). A Li/Li symmetric cell using this electrolyte showed stable long-term plating and stripping, as shown in Figure 13(a5). The dynamic polymer network therefore did more than improve toughness: it simultaneously preserved the mechanical framework and the ion-transport network. When microcracks or local interfacial separation developed, reversible-bond reformation slowed further damage and increased tolerance to cycling-induced strain.

Introducing highly conductive ceramic fillers into a polymer electrolyte can further improve ion transport and mechanical stability. Conventional physically blended polymer–ceramic composites, however, often suffer from particle agglomeration, interfacial debonding, and high-temperature phase separation. The nature of the polymer–ceramic interface is therefore critical. Lei et al. [195] covalently grafted a polyurethane–urea polymer (PUS) containing dynamic disulfide bonds onto $Li_7P_3S_{11}$ ceramic particles. P–N bonds formed between the ceramic surface and polymer chains, strengthening the interface and promoting uniform particle dispersion, as shown in Figure 13(b1). The dynamic disulfide bonds in PUS provided rapid self-healing. Damaged membranes could heal at RT and recover substantial tensile deformability, as shown in Figure 13(b2–b4). Compared with physical blending, chemical grafting suppressed rearrangement and separation of the polymer and ceramic phases under heat or repeated stress and improved load transfer across the interface. A composite electrolyte combining a stable covalent interface with a dynamic reversible network can therefore mitigate phase separation, interfacial debonding, and mechanical cracking simultaneously.

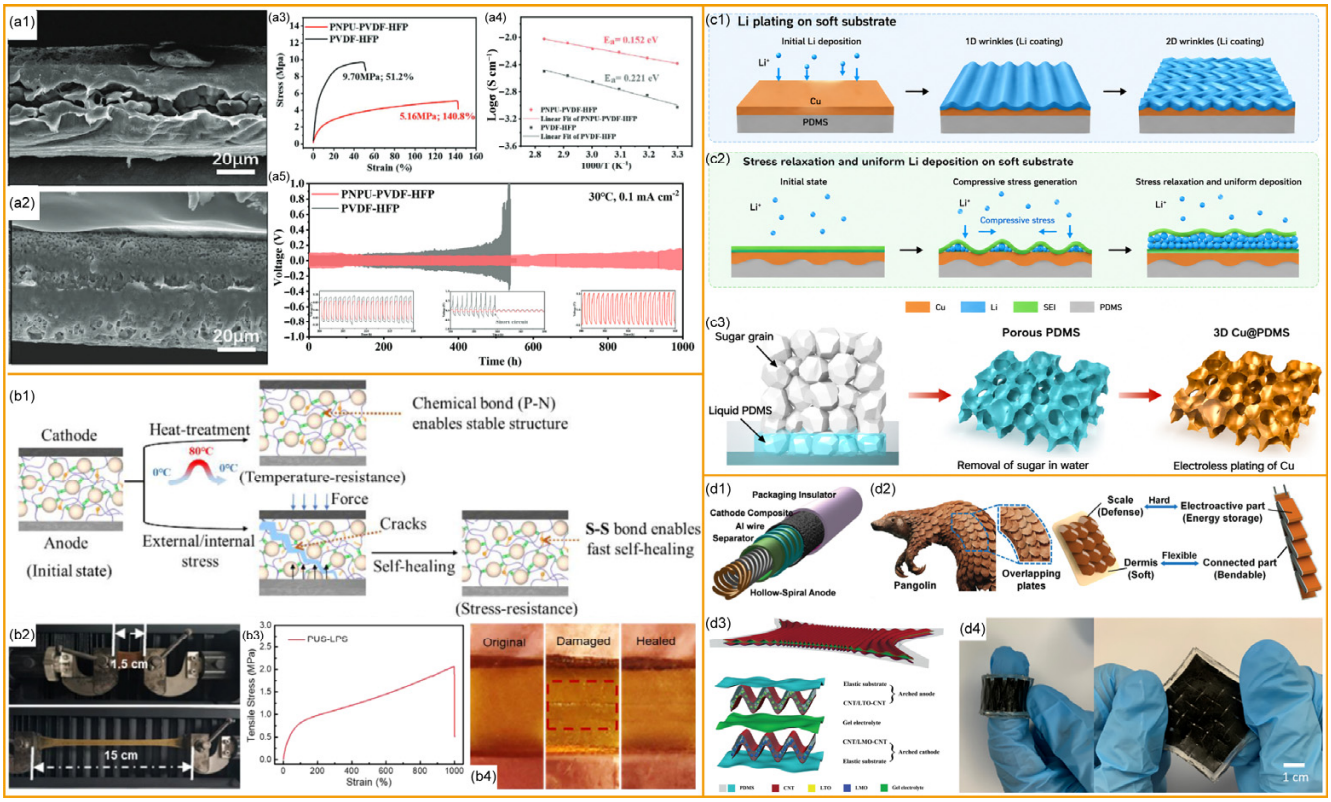


Figure 13. Multiscale electro-chemo-mechanical regulation strategies for mechanically robust ASSLMBs. (**a1**–**a5**) Self-healing polymer–electrolyte design based on a PNPU–PVDF–HFP network with reversible hydrogen bonding, illustrating enhanced mechanical strength and deformability, recovery of structural integrity after damage, improved Li-ion transport, and stable long-term Li plating/stripping enabled by simultaneous preservation of the mechanical framework and ionic-conduction network. (**a1**–**a5**) Reproduced with permission from Ref. [194]. Copyright 2023 Wiley-VCH GmbH. (**b1**–**b4**) Chemically bonded self-healing polymer–ceramic composite electrolyte formed by covalently grafting dynamic polyurethane–urea chains onto $Li_7P_3S_{11}$ particles, showing strengthened polymer/ceramic interfacial adhesion, homogeneous particle dispersion, RT self-healing and recovery of tensile deformability, and improved resistance to phase separation, interfacial debonding, and mechanical cracking. (**b1**–**b4**) Reproduced with permission from Ref. [195]. Copyright 2022 Elsevier B.V. (**c1**–**c3**) Stress regulation of Li deposition through compliant CCs and 3D deposition substrates, comparing stress-constrained Li growth on rigid Cu with stress-relieved deposition on Cu/PDMS and porous Cu@PDMS architectures, where substrate deformation and increased effective surface area redistribute deposition-induced compressive stress and local current density to promote more uniform Li nucleation and growth. (**c1**–**c3**) Adapted from Ref. [196]. Copyright 2018 Springer Nature Limited. (**d1**–**d4**) Cell-level mechanical regulation through geometrically flexible battery architectures, including helical, overlapping rigid–flexible, wrinkled/arched, and kirigami configurations that convert bending, twisting, stretching, and other macroscopic deformations into reversible geometric motion, thereby reducing strain accumulation in brittle active materials and critical interfaces while maintaining electrochemical functionality. (**d1**) Reproduced with permission from Ref. [197]. Copyright 2012 Wiley-VCH Verlag GmbH & Co. KGaA, Weinheim. (**d2**) Reproduced with permission from Ref. [198]. Copyright 2023 Wiley-VCH GmbH. (**d3**) Reproduced with permission from Ref. [199]. Copyright 2015 WILEY-VCH Verlag GmbH & Co. KGaA, Weinheim. (**d4**) Reproduced with permission from Ref. [200]. Copyright 2023 Elsevier B.V.

Overall, self-healing composite electrolytes should be designed to provide continuous Li-ion pathways, sufficient strength and deformability, and the ability to restore local structure and contact after damage. Dynamic hydrogen bonds, disulfide bonds, and other reversible interactions offer useful design tools, although their long-term chemical stability,

healing efficiency, and compatibility with high-voltage cathodes and Li metal remain to be fully established.

6.3.2. Stress Release Through Compliant Deposition Substrates

Li deposition is governed not only by current density and interfacial chemistry but also by the mechanical properties of the CC and deposition substrate. On a rigid CC, volume growth and lateral constraint generate residual compressive stress. If this stress cannot be released, it may promote local plastic deformation, defect growth, and nonuniform deposition, ultimately facilitating dendrite formation.

Wang et al. [196] proposed plating Li on a compliant substrate and identified deposition-induced compressive stress as an important driving force for dendrite growth. On conventional rigid Cu foil, the compressive stress generated during Li deposition is constrained by the substrate and cannot be relieved through overall deformation. Li therefore tends to protrude from local defects and develop into dendritic structures, as illustrated in Figure 13(c1). To modify this boundary condition, the authors deposited a thin Cu layer on a soft polydimethylsiloxane (PDMS) substrate. As Li accumulated, the Cu film released compressive stress through wrinkling and out-of-plane deformation. Li deposited more uniformly and with fewer sharp dendrites, as shown in Figure 13(c2). The CC therefore does more than conduct electrons. Its modulus, thickness, and deformation mode define the mechanical boundary conditions of Li growth. A lower substrate stiffness can convert compressive stress within the Li deposit into reversible deformation of the CC, reducing stress-driven morphological instability.

A 3D Cu@PDMS scaffold was subsequently developed, as shown in Figure 13(c3). Its porous structure increased the effective deposition area and lowered the local current density, while the compliant PDMS framework accommodated deposition stress. Together, these effects improved Li nucleation and growth uniformity and produced more stable cycling. This strategy simultaneously regulates current distribution through 3D geometry and stress distribution through substrate compliance. Future optimization may involve substrate modulus, metal-layer thickness, pore size, and surface lithiophilicity. An excessively soft substrate, however, may suffer from insufficient dimensional stability, excessive interfacial deformation, or packaging difficulties. The goal is therefore not simply to minimize modulus, but to balance mechanical support, contact stability, and stress-release capacity.

6.3.3. Flexible Battery Architectures

Whereas compliant substrates regulate local deposition stress at the electrode level, flexible battery architectures can mitigate damage caused by external bending, stretching, and twisting. Conventional layered cells concentrate stress at electrode, separator, or electrolyte interfaces under large deformation, leading to cracking, delamination, and contact loss. Geometric structures can instead convert macroscopic deformation into helix extension, interlayer sliding, wrinkle flattening, or structural rotation, thereby reducing the strain experienced by electrochemically active regions.

Kwon et al. [197] developed a cable-type battery with hollow multi-helix electrodes, as shown in Figure 13(d1). The helical architecture produced a spring-like mechanical response. During bending, twisting, and even knotting, deformation was accommodated mainly through extension and contraction of the helix rather than direct stretching of the active-material layer. This design demonstrates that changing the conventional planar stack can effectively decouple macroscopic deformation from local electrochemical regions.

Bao et al. [198] developed an overlapping architecture composed of alternating rigid energy-storage units and flexible connecting regions, as shown in Figure 13(d2). Energy storage and mechanical deformation were spatially separated: the rigid units preserved

energy density and electrochemical stability, while the flexible joints accommodated most of the deformation. Compared with making the entire cell flexible, this locally rigid–flexible architecture reduced strain accumulation in the active materials while maintaining both mechanical load-bearing capability and energy-storage performance.

For cells requiring large tensile deformation, wrinkled and arched structures are commonly used. Weng et al. [199] constructed a sandwich electrode containing an aligned carbon-nanotube framework, active material, and an elastic binder. Releasing a prestrained substrate produced arched wrinkles, as shown in Figure 13(d3). During stretching, the arches unfolded before the electrode materials themselves were significantly strained. The aligned CNT network also maintained electronic continuity and reduced loss of active particles, limiting the influence of mechanical deformation on electrochemical performance.

Gao et al. [200] used a kirigami architecture to construct a low-modulus electrode, as shown in Figure 13(d4). During stretching, the cut patterns rotated, opened, and deformed out of plane, converting tensile strain into geometric motion. Unlike designs that depend on the intrinsic elasticity of the electrode materials, kirigami structures place lower demands on the ductility of the active material and CC and can accommodate deformation in multiple directions.

These examples show that flexible battery design does not require every component to be highly extensible. Instead, geometric decoupling can reduce the actual stress carried by brittle active materials and critical interfaces. Helical structures are suited to bending and twisting, overlapping rigid–flexible structures balance energy density and load bearing, wrinkled or arched structures accommodate large uniaxial strain, and kirigami designs enable multidirectional deformation.

Despite these advances, most flexible battery designs have been demonstrated using liquid or gel electrolytes. Extending these concepts to ASSLMBs remains challenging because inorganic SEs generally possess high elastic moduli and limited fracture strains. In addition, the fabrication of complex geometries may introduce extra interfaces, structural defects, and processing difficulties, all of which can compromise mechanical integrity and interfacial stability. Future ASSLMB architectures may therefore require thin, segmented, or modular electrolyte designs in which deformation is preferentially accommodated by compliant connectors while brittle electrolyte layers and solid–solid interfaces remain mechanically protected.

Beyond material and interfacial engineering, advanced manufacturing technologies have recently emerged as an effective means of realizing mechanically optimized battery architectures. Among these approaches, 3D printing offers unprecedented freedom in tailoring geometry, porosity, and interfacial configuration [201]. Unlike conventional slurry coating and lamination, additive manufacturing techniques such as direct ink writing (DIW) and stereolithography (SLA) enable the fabrication of hierarchical porous frameworks, lattice structures, and conformal interfaces with precisely controlled microstructures. These architectures can accommodate electrode deformation, redistribute local stress, improve solid–solid interfacial contact, and construct continuous 3D ion-transport pathways without sacrificing ionic or electronic conductivity. Consequently, 3D printing provides a promising manufacturing platform for integrating structural optimization with electro-chemo-mechanical regulation, offering new opportunities to suppress stress accumulation caused by volume changes and interfacial mismatch in ASSLMBs.

At present, however, a unified electro-chemo-mechanical evaluation framework for flexible ASSLMBs is still lacking. Existing studies employ different bending radii, tensile strains, loading frequencies, and electrochemical testing protocols, making quantitative comparison across different structural designs difficult. Future evaluation should simultaneously consider energy density, capacity retention, maximum deformation, mechanical-

cycle durability, and interfacial-impedance evolution, while also incorporating multiaxial loading, long-term fatigue resistance, packaging reliability, manufacturing scalability, and production cost. Establishing standardized evaluation protocols will facilitate objective comparison among different structural strategies and accelerate their practical implementation.

Overall, electro-chemo-mechanical regulation has evolved from optimizing individual materials toward designing integrated multiscale battery systems. At the material level, self-healing polymers and chemically coupled polymer–ceramic electrolytes improve damage tolerance while preserving ion-transport pathways. At the electrode level, compliant substrates and 3D CCs relieve Li-deposition-induced stress and homogenize current distribution. At the device level, flexible architectures redistribute macroscopic deformation through rational geometric design. Ultimately, achieving durable ASSLMBs will require electro-chemo-mechanical design principles to be incorporated throughout the entire battery—from material selection and interface engineering to electrode architecture, cell configuration, and scalable manufacturing—thereby enabling mechanically resilient and high-energy ASSLMBs for practical applications.

7. AI-Driven Electro-Chemo-Mechanical Prediction and Intelligent Design

The electro-chemo-mechanical behavior of ASSLMBs originates from the strong coupling among Li-ion transport, electrochemical reactions, stress evolution, interfacial contact, and microstructural degradation across multiple length and time scales. Conventional experimental characterization and multiphysics simulations have substantially advanced the understanding of these coupled processes. However, the increasing complexity of solid–solid interfaces, together with the rapid growth of imaging, spectroscopy, electrochemical, and mechanical datasets, makes quantitative interpretation and predictive design increasingly challenging. Artificial intelligence (AI) therefore provides a promising opportunity to bridge experimental characterization, physics-based simulations, and battery design [202–204]. Rather than replacing conventional approaches, AI is increasingly being integrated with electro-chemo-mechanical models to establish efficient frameworks for failure prediction, mechanism interpretation, and inverse optimization [205–207].

7.1. AI-Assisted Prediction of Electro-Chemo-Mechanical Failure

A representative example was recently reported by Wu et al. [208], who developed a prior-knowledge-driven machine-learning framework for predicting electro-chemo-mechanical failure in SEs. Instead of relying solely on data-driven learning, coupled electro-chemo-mechanical finite-element simulations were first used to generate defect–stress datasets for various defect distributions. Physically meaningful descriptors, including defect curvature, eccentricity, aspect ratio, symmetry, and defect density, were subsequently incorporated into a physics-informed SE-UNet model during network training. Compared with conventional convolutional neural networks (CNN), residual networks (ResNet), and UNet models, the proposed framework achieved significantly higher accuracy in reconstructing von Mises stress fields while exhibiting improved generalization across different defect configurations. More importantly, it reduced the computational cost of conventional finite-element analysis by several orders of magnitude. Such physics-informed surrogate models provide an efficient route for rapidly identifying stress-concentration regions, evaluating electro-chemo-mechanical failure risks, and guiding the optimization of pore morphology, defect density, and grain-boundary distributions in SEs.

7.2. AI-Driven Interface Design and Optimization

Beyond predicting stress evolution in bulk SEs, AI has recently become an increasingly powerful tool for optimizing the complex electrode/SE interfaces that dominate

electro-chemo-mechanical degradation in ASSLMBs. Unlike bulk-material design, interface engineering requires the simultaneous optimization of multiple competing factors, including chemical stability, Li-ion transport, electronic insulation, interfacial adhesion, mechanical compliance, and long-term structural stability. Consequently, interface optimization naturally becomes a multi-objective optimization problem rather than a conventional single-property screening task.

Wang et al. [209] summarized three major AI strategies for SE and interface engineering, including structure–property screening pipelines, molecular dynamics accelerated by machine-learning force fields (MLFFs), and inverse materials design based on generative models. Together, these approaches establish an efficient framework for discovering stable interfaces, understanding interfacial evolution, and optimizing interfacial structures under realistic operating conditions.

Recent advances in halide solid electrolytes further demonstrate the potential of machine learning for materials screening, ion-transport analysis, and prediction of interfacial reactions, providing a complementary route toward data-driven interface optimization [210]. One representative application is the prediction of Li-metal/SE interfacial stability. Rather than classifying interfaces simply as thermodynamically stable or unstable, recent AI-assisted approaches distinguish stable, passivating, and continuously reactive interfaces according to atomic rearrangement, decomposition kinetics, and sublattice diffusion [211]. This distinction is particularly important for electro-chemo-mechanical analysis because a moderately reactive interface may still be desirable if it forms a dense, ionically conductive, and electronically insulating passivation layer. In contrast, continuously reactive interfaces usually undergo persistent decomposition, interphase thickening, local volume expansion, and mechanical degradation, resulting in increasing interfacial resistance and stress accumulation during cycling. Compared with evaluating reaction energy alone, AI-based kinetic classification therefore provides a more realistic criterion for selecting Li-compatible SEs and artificial interphases.

Mechanical properties should also be incorporated explicitly into interface optimization. Several machine-learning frameworks have been developed to predict the bulk modulus, shear modulus, elastic anisotropy, and thermodynamic stability of candidate SEs [212,213]. By combining graph-based machine learning with high-throughput first-principles calculations, these studies screened garnet-type electrolytes while simultaneously considering ionic conductivity, electronic insulation, thermodynamic stability, and elastic properties. Rather than maximizing a single parameter, the resulting models identify materials that balance mechanical robustness with efficient Li-ion transport, illustrating the advantages of AI for multidimensional interface design.

From the perspective of electro-chemo-mechanical coupling, interface optimization can therefore be formulated as a multiobjective optimization problem,

$$\min_{x} \left[R_{\mathrm{int}}, \Delta G_{\mathrm{rxn}}, \sigma_{\mathrm{max}}, D_{\mathrm{damage}} \right] \tag{11}$$

subject to

$$\sigma_{\mathrm{ion}} \geq \sigma_{\mathrm{min}},\ \sigma_{\mathrm{e}} \leq \sigma_{\mathrm{e,max}},\ K_{\mathrm{Ic}} \geq K_{\mathrm{Ic,min}} \tag{12}$$

where x represents design variables such as interphase composition, coating thickness, porosity, elastic modulus, adhesion strength, and processing conditions. Here, R_{int}, ΔG_{rxn}, σ_{max}, and D_{damage} denote the interfacial resistance, reaction free energy, maximum local stress, and a damage descriptor, respectively. This formulation highlights that the optimal interface should simultaneously minimize electrochemical polarization, suppress side reactions, and alleviate stress concentration, rather than optimizing any single property independently.

AI-assisted optimization is equally valuable for cathode/SE interfaces, where coating layers must remain chemically stable against both high-voltage cathodes and reactive SEs. High-throughput screening frameworks have therefore been developed to identify coating materials according to electronic insulation, electrochemical stability, reaction energy, and Li-ion diffusivity. Machine-learning force fields further enable molecular dynamics simulations over much larger temporal and spatial scales than conventional ab initio molecular dynamics, allowing realistic investigation of interfacial reconstruction, elemental interdiffusion, and Li-ion migration.

A representative example is the optimization of amorphous LiF coatings at the LCO/LPSC interface [214]. Machine-learning-assisted molecular dynamics demonstrated that LiF effectively suppresses direct chemical reactions between LCO and LPSC while preserving the structural integrity of the sulfide electrolyte. However, when the coating thickness exceeded approximately 1 nm, increasingly ordered LiF regions developed and substantially impeded Li-ion transport. This study illustrates an important electro-chemo-mechanical principle: the thickest or chemically most stable coating is not necessarily optimal. Instead, coating layers should be sufficiently thick to suppress side reactions and accommodate interfacial deformation, yet sufficiently thin and ionically conductive to minimize transport resistance. AI therefore provides an efficient strategy for simultaneously optimizing coating composition, thickness, ionic conductivity, and mechanical compliance.

7.3. AI-Enhanced Electro-Chemo-Mechanical Characterization

Besides interface optimization, AI has begun to substantially enhance advanced electro-chemo-mechanical characterization techniques. Conventional electrochemical measurements, such as EIS and cyclic voltammetry (CV), primarily monitor electrical responses and therefore cannot directly distinguish stress accumulation, crack formation, interfacial contact loss, and chemical degradation. Emerging techniques, including mechano-electrochemical impedance spectroscopy (MEIS) and mechano-voltammetry (MV), simultaneously acquire electrochemical and mechanical signals during battery operation [215]. Combined with AI-assisted feature extraction and machine-learning algorithms, these techniques enable automatic identification of mechanically sensitive spectral features for SOC and state-of-health estimation while providing quantitative information on stress relaxation, particle breathing, porous-electrode compaction, and stress-coupled transport processes that are inaccessible using conventional electrochemical measurements.

AI also enables multimodal characterization by integrating electron microscopy, XCT, diffraction, spectroscopy, impedance, strain, and pressure measurements into a unified analytical framework. Computer-vision algorithms can automatically extract particle morphology, pore distribution, crack density, grain-boundary characteristics, and interfacial contact fractions from large imaging datasets. Multimodal learning subsequently correlates these structural descriptors with electrochemical and mechanical responses, allowing different degradation mechanisms to be distinguished even when they produce similar voltage or impedance signatures. Such developments considerably improve the interpretability of operando characterization and provide quantitative descriptors for electro-chemo-mechanical modeling.

7.4. Toward Closed-Loop Electro-Chemo-Mechanical Design

Despite these advances, current AI applications in ASSLMBs remain largely focused on individual tasks, such as property prediction, interface screening, or image analysis. In contrast, future electro-chemo-mechanical research will increasingly rely on closed-loop AI frameworks that integrate characterization, physics-based modeling, intelligent optimization, and experimental validation into a unified workflow [216,217].

In a typical closed-loop framework, multimodal operando characterization techniques—including electron microscopy, X-ray imaging, spectroscopy, and electrochemical–mechanical measurements—first provide quantitative descriptors of microstructure, stress evolution, and interfacial degradation. These data are subsequently combined with physics-informed machine learning and multiscale simulations to establish predictive models for Li-ion transport, stress distribution, and damage evolution. The resulting models can then be coupled with Bayesian optimization, active learning, or generative AI to inversely design SEs, artificial interphases, coating layers, electrode microstructures, and operating conditions with targeted electro-chemo-mechanical performance [218]. Experimental validation continuously updates the training database, enabling iterative improvement of both the predictive models and material design strategies.

Such a closed-loop framework transforms AI from a passive data-analysis tool into an active decision-making platform for electro-chemo-mechanical engineering. Rather than optimizing electrochemical, mechanical, or interfacial properties independently, future AI models are expected to simultaneously consider ionic transport, chemical stability, mechanical integrity, and interfacial evolution across multiple length scales. As standardized multimodal databases, physics-informed learning algorithms, and autonomous experimentation continue to mature, AI will play an increasingly important role in accelerating the inverse design of mechanically robust ASSLMBs with stable solid–solid interfaces and predictable long-term degradation.

8. Summary and Outlook

Electro-chemo-mechanical coupling fundamentally distinguishes ASSLMBs from conventional liquid-electrolyte batteries. Throughout battery operation, electrochemical reactions continuously generate mechanical stresses through cathode volume changes, chemo-mechanical mismatch, Li plating and stripping, stack pressure, and thermal effects. These stresses are not merely passive consequences of electrochemical processes; they actively modify ion transport, reaction kinetics, interfacial contact, and current distribution, giving rise to a dynamic feedback loop that governs structural degradation, interfacial instability, and ultimately cell performance. In this review, we have established a unified framework linking the origins of stress with its electrochemical consequences, representative failure mechanisms, advanced characterization techniques, mitigation strategies, and emerging AI-assisted approaches. Rather than treating electrochemical and mechanical phenomena independently, this framework highlights that battery degradation arises from their continuous interaction across multiple length scales, from atomic defects and grain boundaries to composite electrodes and full cells.

Despite remarkable progress over the past decade, several fundamental questions remain unresolved. Although numerous studies have investigated individual aspects of electro-chemo-mechanical coupling, a quantitative understanding of their interactions is still lacking. How can local stress, ion transport, electrochemical reactions, and fracture be quantitatively linked across different length and time scales? Existing models often focus on isolated processes and therefore cannot fully describe the coupled evolution of practical ASSLMBs. Which operando signals can reliably predict mechanical failure before an abrupt voltage collapse or internal short circuit occurs? While pressure, strain, impedance, acoustic emission, and imaging techniques have each revealed part of the degradation process, robust early-warning indicators remain elusive. Can mechanically compatible electrodes and adaptive interfaces maintain stable solid–solid contact under practically relevant stack pressures, high areal capacities, and long-term cycling? Addressing these questions will require a deeper understanding of the interplay between electrochemistry, mechanics,

and interfacial evolution, rather than continued optimization of individual materials or interfaces in isolation.

Future progress will depend on closer integration between experiments, modeling, and materials design. Experimentally validated multiphysics models that couple electrochemical reactions, ion transport, mechanics, thermal effects, and interfacial evolution are needed to establish quantitative relationships between local physicochemical processes and macroscopic battery performance. At the same time, multimodal operando characterization techniques should move beyond observing individual phenomena toward simultaneously resolving Li transport, stress evolution, chemical reactions, structural degradation, and contact evolution within buried solid–solid interfaces. Standardized testing under practically relevant conditions—including realistic stack pressures, areal capacities, current densities, temperatures, and cycling protocols—will also be essential for enabling meaningful comparisons among different materials and cell configurations and for translating laboratory-scale observations into practical cell designs.

Looking forward, the goal of electro-chemo-mechanical research should extend beyond identifying individual degradation mechanisms or developing isolated mitigation strategies. A more important objective is to establish quantitative design principles that relate material properties, interface characteristics, electrode architectures, and operating conditions to long-term mechanical and electrochemical stability. Such principles would enable the rational design of ASSLMBs based on predictive rather than empirical approaches. As advanced characterization, multiscale modeling, data-driven methods, and intelligent materials design continue to develop, electro-chemo-mechanical studies are expected to evolve from qualitative interpretation toward quantitative prediction. This transition will not only deepen our fundamental understanding of coupled degradation processes but also provide a more reliable scientific foundation for developing high-energy, mechanically robust, and commercially viable ASSLMBs.

Author Contributions: Conceptualization, E.J.C.; Investigation, Q.L.; Writing—original draft preparation, Q.L. and E.J.C.; Writing—review and editing, Y.L., Z.W., K.-Y.P., S.F. and H.K.; Visualization, Q.L. and E.J.C.; Supervision, H.K. and E.J.C.; Project administration, E.J.C.; Funding acquisition, E.J.C. Funding: This research was funded by the JST Strategic International Collaborative Research Program (SICORP; JPMJSC25E2); the GIMRT Program (202512-CRKKE-0212) of the Institute for Materials Research; and the FY2026 TUMUG Research Support Staff Program. All authors have read and agreed to the published version of the manuscript.

Funding: This research was funded by the JST Strategic International Collaborative Research Program (SICORP; JPMJSC25E2); the GIMRT Program (202512-CRKKE-0212) of the Institute for Materials Research; and the FY2026 TUMUG Research Support Staff Program.

Data Availability Statement: No new data were created or analyzed in this study. Data sharing is not applicable to this article.

Acknowledgments: The authors gratefully acknowledge the support from the Core Research Cluster for Materials Science (CRC-MS), Tohoku University.

Conflicts of Interest: The authors declare no conflict of interest.

References

1. Goodenough, J.B.; Park, K.-S. The Li-Ion Rechargeable Battery: A Perspective. *J. Am. Chem. Soc.* **2013**, *135*, 1167–1176. [CrossRef] [PubMed]
2. Manthiram, A. A Reflection on Lithium-Ion Battery Cathode Chemistry. *Nat. Commun.* **2020**, *11*, 1550. [CrossRef] [PubMed]
3. Janek, J.; Zeier, W.G. A Solid Future for Battery Development. *Nat. Energy* **2016**, *1*, 16141. [CrossRef]
4. Manthiram, A.; Yu, X.; Wang, S. Lithium Battery Chemistries Enabled by Solid-State Electrolytes. *Nat. Rev. Mater.* **2017**, *2*, 16103. [CrossRef]

5. Muzakir, M.; Manickavasakam, K.; Cheng, E.J.; Yang, F.; Wang, Z.; Li, H.; Zhang, X.; Qin, J. Inorganic Solid Electrolytes for All-Solid-State Lithium/Sodium-Ion Batteries: Recent Developments and Applications. *J. Mater. Chem. A* **2025**, *13*, 73–135. [CrossRef]
6. Sun, C.; Liu, J.; Gong, Y.; Wilkinson, D.P.; Zhang, J. Recent Advances in All-Solid-State Rechargeable Lithium Batteries. *Nano Energy* **2017**, *33*, 363–386. [CrossRef]
7. Famprikis, T.; Canepa, P.; Dawson, J.A.; Islam, M.S.; Masquelier, C. Fundamentals of Inorganic Solid-State Electrolytes for Batteries. *Nat. Mater.* **2019**, *18*, 1278–1291. [CrossRef] [PubMed]
8. Kalnaus, S.; Dudney, N.J.; Westover, A.S.; Herbert, E.; Hackney, S. Solid-State Batteries: The Critical Role of Mechanics. *Science* **2023**, *381*, eabg5998. [CrossRef] [PubMed]
9. Chen, R.; Li, Q.; Yu, X.; Chen, L.; Li, H. Approaching Practically Accessible Solid-State Batteries: Stability Issues Related to Solid Electrolytes and Interfaces. *Chem. Rev.* **2020**, *120*, 6820–6877. [CrossRef] [PubMed]
10. Janek, J.; Zeier, W.G. Challenges in Speeding up Solid-State Battery Development. *Nat. Energy* **2023**, *8*, 230–240. [CrossRef]
11. Lewis, J.A.; Tippens, J.; Cortes, F.J.Q.; McDowell, M.T. Chemo-Mechanical Challenges in Solid-State Batteries. *Trends Chem.* **2019**, *1*, 845–857. [CrossRef]
12. Wang, M.J.; Kazyak, E.; Dasgupta, N.P.; Sakamoto, J. Transitioning Solid-State Batteries from Lab to Market: Linking Electro-Chemo-Mechanics with Practical Considerations. *Joule* **2021**, *5*, 1371–1390. [CrossRef]
13. Koerver, R.; Zhang, W.; De Biasi, L.; Schweidler, S.; Kondrakov, A.O.; Kolling, S.; Brezesinski, T.; Hartmann, P.; Zeier, W.G.; Janek, J. Chemo-Mechanical Expansion of Lithium Electrode Materials—On the Route to Mechanically Optimized All-Solid-State Batteries. *Energy Environ. Sci.* **2018**, *11*, 2142–2158. [CrossRef]
14. Liu, J.; Yuan, H.; Liu, H.; Zhao, C.-Z.; Lu, Y.; Cheng, X.-B.; Huang, J.-Q.; Zhang, Q. Unlocking the Failure Mechanism of Solid State Lithium Metal Batteries. *Adv. Energy Mater.* **2022**, *12*, 2100748. [CrossRef]
15. Gu, J.; Chen, X.; He, Z.; Liang, Z.; Lin, Y.; Shi, J.; Yang, Y. Decoding Internal Stress-Induced Micro-Short Circuit Events in Sulfide-Based All-Solid-State Li-Metal Batteries via Operando Pressure Measurements. *Adv. Energy Mater.* **2023**, *13*, 2302643. [CrossRef]
16. Wang, P.; Qu, W.; Song, W.-L.; Chen, H.; Chen, R.; Fang, D. Electro–Chemo–Mechanical Issues at the Interfaces in Solid-State Lithium Metal Batteries. *Adv. Funct. Mater.* **2019**, *29*, 1900950. [CrossRef]
17. De Gol, A.; Dermenci, K.B.; Farkas, L.; Berecibar, M. Electro-Chemo-Mechanical Degradation in Solid-State Batteries: A Review of Microscale and Multiphysics Modeling. *Adv. Energy Mater.* **2024**, *14*, 2403255. [CrossRef]
18. Alsaç, E.P.; Nelson, D.L.; Yoon, S.G.; Cavallaro, K.A.; Wang, C.; Sandoval, S.E.; Eze, U.D.; Jeong, W.J.; McDowell, M.T. Characterizing Electrode Materials and Interfaces in Solid-State Batteries. *Chem. Rev.* **2025**, *125*, 2009–2119. [CrossRef] [PubMed]
19. Tan, D.H.S.; Banerjee, A.; Chen, Z.; Meng, Y.S. From Nanoscale Interface Characterization to Sustainable Energy Storage Using All-Solid-State Batteries. *Nat. Nanotechnol.* **2020**, *15*, 170–180. [CrossRef] [PubMed]
20. Xiang, Y.; Li, X.; Cheng, Y.; Sun, X.; Yang, Y. Advanced Characterization Techniques for Solid State Lithium Battery Research. *Mater. Today* **2020**, *36*, 139–157. [CrossRef]
21. Liu, Q.; Chen, Q.; Tang, Y.; Cheng, H.-M. Interfacial Modification, Electrode/Solid-Electrolyte Engineering, and Monolithic Construction of Solid-State Batteries. *Electrochem. Energy Rev.* **2023**, *6*, 15. [CrossRef]
22. Feng, X.; Fang, H.; Wu, N.; Liu, P.; Jena, P.; Nanda, J.; Mitlin, D. Review of Modification Strategies in Emerging Inorganic Solid-State Electrolytes for Lithium, Sodium, and Potassium Batteries. *Joule* **2022**, *6*, 543–587. [CrossRef]
23. Gu, J.; Liang, Z.; Shi, J.; Yang, Y. Electrochemo-Mechanical Stresses and Their Measurements in Sulfide-Based All-Solid-State Batteries: A Review. *Adv. Energy Mater.* **2023**, *13*, 2203153. [CrossRef]
24. Tian, H.-K.; Chakraborty, A.; Talin, A.A.; Eisenlohr, P.; Qi, Y. Evaluation of The Electrochemo-Mechanically Induced Stress in All-Solid-State Li-Ion Batteries. *J. Electrochem. Soc.* **2020**, *167*, 090541. [CrossRef]
25. Barai, P.; Higa, K.; Ngo, A.T.; Curtiss, L.A.; Srinivasan, V. Mechanical Stress Induced Current Focusing and Fracture in Grain Boundaries. *J. Electrochem. Soc.* **2019**, *166*, A1752. [CrossRef]
26. Wang, Y.; Liu, J.; Chen, T.; Lin, W.; Zheng, J. Factors That Affect Volume Change during Electrochemical Cycling in Cathode Materials for Lithium Ion Batteries. *Phys. Chem. Chem. Phys.* **2022**, *24*, 2167–2175. [CrossRef] [PubMed]
27. Ryu, H.-H.; Park, K.-J.; Yoon, C.S.; Sun, Y.-K. Capacity Fading of Ni-Rich $Li[Ni_xCo_yMn_{1-x-y}]O_2$ ($0.6 \leq x \leq 0.95$) Cathodes for High-Energy-Density Lithium-Ion Batteries: Bulk or Surface Degradation? *Chem. Mater.* **2018**, *30*, 1155–1163. [CrossRef]
28. Li, W.; Asl, H.Y.; Xie, Q.; Manthiram, A. Collapse of $LiNi_{1-x-y}Co_xMn_yO_2$ Lattice at Deep Charge Irrespective of Nickel Content in Lithium-Ion Batteries. *J. Am. Chem. Soc.* **2019**, *141*, 5097–5101. [CrossRef] [PubMed]
29. Kondrakov, A.O.; Schmidt, A.; Xu, J.; Geßwein, H.; Mönig, R.; Hartmann, P.; Sommer, H.; Brezesinski, T.; Janek, J. Anisotropic Lattice Strain and Mechanical Degradation of High- and Low-Nickel NCM Cathode Materials for Li-Ion Batteries. *J. Phys. Chem. C* **2017**, *121*, 3286–3294. [CrossRef]

30. Kwon, J.; Kim, J.; Lim, J.-H.; Lee, K.E.; Kang, S.-M.; Kong, Y.; Kim, D.-H.; Kim, K.-S.; Choe, G.; Jung, S.-M.; et al. Understanding Mechanical Failure Behaviours and Protocol Optimization for Fast Charging Applications in Co-Free Ni-Based Cathodes for Lithium-Ion Batteries. *Mater. Horiz.* **2025**, *12*, 1133–1143. [CrossRef] [PubMed]
31. Trevisanello, E.; Ruess, R.; Conforto, G.; Richter, F.H.; Janek, J. Polycrystalline and Single Crystalline NCM Cathode Materials—Quantifying Particle Cracking, Active Surface Area, and Lithium Diffusion. *Adv. Energy Mater.* **2021**, *11*, 2003400. [CrossRef]
32. de Biasi, L.; Schiele, A.; Roca-Ayats, M.; Garcia, G.; Brezesinski, T.; Hartmann, P.; Janek, J. Phase Transformation Behavior and Stability of LiNiO2 Cathode Material for Li-Ion Batteries Obtained from In Situ Gas Analysis and Operando X-Ray Diffraction. *ChemSusChem* **2019**, *12*, 2240–2250. [CrossRef] [PubMed]
33. Luo, J.; Dai, C.Y.; Wang, Z.; Liu, K.; Mao, W.G.; Fang, D.N.; Chen, X. In-Situ Measurements of Mechanical and Volume Change of LiCoO2 Lithium-Ion Batteries during Repeated Charge–Discharge Cycling by Using Digital Image Correlation. *Measurement* **2016**, *94*, 759–770. [CrossRef]
34. Cheng, E.J.; Taylor, N.J.; Wolfenstine, J.; Sakamoto, J. Elastic Properties of Lithium Cobalt Oxide ($LiCoO_2$). *J. Asian Ceram. Soc.* **2017**, *5*, 113–117. [CrossRef]
35. Song, J.-H.; Yu, S.; Kim, B.; Eum, D.; Cho, J.; Jang, H.-Y.; Park, S.-O.; Yoo, J.; Ko, Y.; Lee, K.; et al. Slab Gliding, a Hidden Factor That Induces Irreversibility and Redox Asymmetry of Lithium-Rich Layered Oxide Cathodes. *Nat. Commun.* **2023**, *14*, 4149. [CrossRef] [PubMed]
36. Park, K.; Zhu, Y.; Torres-Castanedo, C.G.; Jung, H.J.; Luu, N.S.; Kahvecioglu, O.; Yoo, Y.; Seo, J.T.; Downing, J.R.; Lim, H.; et al. Elucidating and Mitigating High-Voltage Degradation Cascades in Cobalt-Free $LiNiO_2$ Lithium-Ion Battery Cathodes. *Adv. Mater.* **2022**, *34*, 2106402. [CrossRef] [PubMed]
37. Thackeray, M.M. Manganese Oxides for Lithium Batteries. *Prog. Solid State Chem.* **1997**, *25*, 1–71. [CrossRef]
38. Liu, H.; Wang, J.; Zhang, X.; Zhou, D.; Qi, X.; Qiu, B.; Fang, J.; Kloepsch, R.; Schumacher, G.; Liu, Z.; et al. Morphological Evolution of High-Voltage Spinel LiNi0.5Mn1.5O4 Cathode Materials for Lithium-Ion Batteries: The Critical Effects of Surface Orientations and Particle Size. *ACS Appl. Mater. Interfaces* **2016**, *8*, 4661–4675. [CrossRef] [PubMed]
39. Thackeray, M.M. Spinel Electrodes for Lithium Batteries. *J. Am. Ceram. Soc.* **1999**, *82*, 3347–3354. [CrossRef]
40. Yamada, A.; Tanaka, M.; Tanaka, K.; Sekai, K. Jahn–Teller Instability in Spinel Li–Mn–O. *J. Power Sources* **1999**, *81–82*, 73–78. [CrossRef]
41. Tang, D.; Sun, Y.; Yang, Z.; Ben, L.; Gu, L.; Huang, X. Surface Structure Evolution of $LiMn_2O_4$ Cathode Material upon Charge/Discharge. *Chem. Mater.* **2014**, *26*, 3535–3543. [CrossRef]
42. Malik, R.; Abdellahi, A.; Ceder, G. A Critical Review of the Li Insertion Mechanisms in LiFePO4 Electrodes. *J. Electrochem. Soc.* **2013**, *160*, A3179. [CrossRef]
43. Gardiner, G.R.; Islam, M.S. Anti-Site Defects and Ion Migration in the LiFe0.5Mn0.5PO4 Mixed-Metal Cathode Material. *Chem. Mater.* **2010**, *22*, 1242–1248. [CrossRef]
44. Yu, H.; Zhang, E.; Yu, J.; Yu, S.; Fang, Y.; Chen, L.; Jiang, H.; Li, C. Relaxing the Jahn–Teller Distortion of $LiMn_{0.6}Fe_{0.4}PO_4$ Cathodes via Mg/Ni Dual-Doping for High-Rate and Long-Life Li-Ion Batteries. *J. Mater. Chem. A* **2024**, *12*, 26076–26082. [CrossRef]
45. Naik, K.G.; Vishnugopi, B.S.; Datta, J.; Datta, D.; Mukherjee, P.P. Electro-Chemo-Mechanical Challenges and Perspective in Lithium Metal Batteries. *Appl. Mech. Rev.* **2023**, *75*, 010802. [CrossRef]
46. Antolini, E. LiCoO2: Formation, Structure, Lithium and Oxygen Nonstoichiometry, Electrochemical Behaviour and Transport Properties. *Solid State Ion.* **2004**, *170*, 159–171. [CrossRef]
47. Lin, C.; Li, J.; Yin, Z.; Huang, W.; Zhao, Q.; Weng, Q.; Liu, Q.; Sun, J.; Chen, G.; Pan, F. Structural Understanding for High-Voltage Stabilization of Lithium Cobalt Oxide. *Adv. Mater.* **2024**, *36*, 2307404. [CrossRef] [PubMed]
48. Yoon, W.-S.; Chung, K.Y.; McBreen, J.; Yang, X.-Q. A Comparative Study on Structural Changes of LiCo1/3Ni1/3Mn1/3O2 and LiNi0.8Co0.15Al0.05O2 during First Charge Using in Situ XRD. *Electrochem. Commun.* **2006**, *8*, 1257–1262. [CrossRef]
49. Friedrich, F.; Strehle, B.; Freiberg, A.T.S.; Kleiner, K.; Day, S.J.; Erk, C.; Piana, M.; Gasteiger, H.A. Editors' Choice—Capacity Fading Mechanisms of NCM-811 Cathodes in Lithium-Ion Batteries Studied by X-Ray Diffraction and Other Diagnostics. *J. Electrochem. Soc.* **2019**, *166*, A3760–A3774. [CrossRef]
50. Zhang, Y.; Hao, S.; Pei, F.; Xiao, X.; Lu, C.; Lin, X.; Li, Z.; Ji, H.; Shen, Y.; Yuan, L.; et al. *Operando* Chemo-Mechanical Evolution in LiNi0.8Co0.1Mn0.1O2 Cathodes. *Natl. Sci. Rev.* **2024**, *11*, nwae254. [CrossRef] [PubMed]
51. Zhou, T.; Wang, H.; Wang, Y.; Jiao, P.; Hao, Z.; Zhang, K.; Xu, J.; Liu, J.-B.; He, Y.-S.; Zhang, Y.-X.; et al. Stabilizing Lattice Oxygen in Slightly Li-Enriched Nickel Oxide Cathodes toward High-Energy Batteries. *Chem* **2022**, *8*, 2817–2830. [CrossRef]
52. Choa, J.; Thackeray, M.M. Structural Changes of LiMn2 O 4 Spinel Electrodes during Electrochemical Cycling. *J. Electrochem. Soc.* **1999**, *146*, 3577–3581. [CrossRef]
53. Zuo, C.; Hu, Z.; Qi, R.; Liu, J.; Li, Z.; Lu, J.; Dong, C.; Yang, K.; Huang, W.; Chen, C.; et al. Double the Capacity of Manganese Spinel for Lithium-Ion Storage by Suppression of Cooperative Jahn–Teller Distortion. *Adv. Energy Mater.* **2020**, *10*, 2000363. [CrossRef]

54. Zhu, X.; Huang, A.; Martens, I.; Vostrov, N.; Sun, Y.; Richard, M.; Schülli, T.U.; Wang, L. High-Voltage Spinel Cathode Materials: Navigating the Structural Evolution for Lithium-Ion Batteries. *Adv. Mater.* **2024**, *36*, 2403482. [CrossRef] [PubMed]
55. Kim, T.; Oh, H.; Yang, S.; Lee, H.J. Unlocking 5 V-Class Lithium-Ion Batteries: Challenges and Perspectives on High-Voltage LNMO Cathodes. *ACS Appl. Energy Mater.* **2025**, *8*, 13155–13178. [CrossRef]
56. Liu, H.; Strobridge, F.C.; Borkiewicz, O.J.; Wiaderek, K.M.; Chapman, K.W.; Chupas, P.J.; Grey, C.P. Capturing Metastable Structures during High-Rate Cycling of $LiFePO_4$ Nanoparticle Electrodes. *Science* **2014**, *344*, 1252817. [CrossRef] [PubMed]
57. Zhang, X.; Van Hulzen, M.; Singh, D.P.; Brownrigg, A.; Wright, J.P.; Van Dijk, N.H.; Wagemaker, M. Direct View on the Phase Evolution in Individual LiFePO4 Nanoparticles during Li-Ion Battery Cycling. *Nat. Commun.* **2015**, *6*, 8333. [CrossRef] [PubMed]
58. Tuo, K.; Sun, C.; Liu, S. Recent Progress in and Perspectives on Emerging Halide Superionic Conductors for All-Solid-State Batteries. *Electrochem. Energy Rev.* **2023**, *6*, 17. [CrossRef]
59. Murugan, R.; Thangadurai, V.; Weppner, W. Fast Lithium Ion Conduction in Garnet-Type $Li_7La_3Zr_2O_{12}$. *Angew. Chem. Int. Ed.* **2007**, *46*, 7778–7781. [CrossRef] [PubMed]
60. Ni, J.E.; Case, E.D.; Sakamoto, J.S.; Rangasamy, E.; Wolfenstine, J.B. Room Temperature Elastic Moduli and Vickers Hardness of Hot-Pressed LLZO Cubic Garnet. *J. Mater. Sci.* **2012**, *47*, 7978–7985. [CrossRef]
61. Wolfenstine, J.; Jo, H.; Cho, Y.-H.; David, I.N.; Askeland, P.; Case, E.D.; Kim, H.; Choe, H.; Sakamoto, J. A Preliminary Investigation of Fracture Toughness of $Li_7La_3Zr_2O_{12}$ and Its Comparison to Other Solid Li-Ionconductors. *Mater. Lett.* **2013**, *96*, 117–120. [CrossRef]
62. Hu, S.; Xu, P.; De Vasconcelos, L.S.; Stanciu, L.; Ni, H.; Zhao, K. Elastic Modulus, Hardness, and Fracture Toughness of $Li_{6.4}La_3Zr_{1.4}Ta_{0.6}O_{12}$ Solid Electrolyte. *Chin. Phys. Lett.* **2021**, *38*, 098401. [CrossRef]
63. Stramare, S.; Thangadurai, V.; Weppner, W. Lithium Lanthanum Titanates: A Review. *Chem. Mater.* **2003**, *15*, 3974–3990. [CrossRef]
64. Cho, Y.-H.; Wolfenstine, J.; Rangasamy, E.; Kim, H.; Choe, H.; Sakamoto, J. Mechanical Properties of the Solid Li-Ion Conducting Electrolyte: $Li_{0.33}La_{0.57}TiO_3$. *J. Mater. Sci.* **2012**, *47*, 5970–5977. [CrossRef]
65. Cooper, C.; Sutorik, A.C.; Wright, J.; Luoto, E.A.; Gilde, G.; Wolfenstine, J. Mechanical Properties of Hot Isostatically Pressed $Li_{0.35}La_{0.55}TiO_3$. *Adv. Eng. Mater.* **2014**, *16*, 755–759. [CrossRef]
66. Yan, G.; Yu, S.; Nonemacher, J.F.; Tempel, H.; Kungl, H.; Malzbender, J.; Eichel, R.-A.; Krüger, M. Influence of Sintering Temperature on Conductivity and Mechanical Behavior of the Solid Electrolyte LATP. *Ceram. Int.* **2019**, *45*, 14697–14703. [CrossRef]
67. Chen, K.; Lang, L.; Lyu, T.; Qu, N.; Li, G.; Abu-Lebdeh, Y.; Zou, Y. Strain Rate Sensitivity of NASICON-Type Li-Ion Conductors: Competing Mechanism between Plastic Deformation and Crack Propagation. *J. Power Sources* **2026**, *666*, 239159. [CrossRef]
68. Hayashi, A.; Hama, S.; Morimoto, H.; Tatsumisago, M.; Minami, T. Preparation of Li_2S–P_2S_5 Amorphous Solid Electrolytes by Mechanical Milling. *J. Am. Ceram. Soc.* **2001**, *84*, 477–479. [CrossRef]
69. Sakuda, A.; Hayashi, A.; Takigawa, Y.; Higashi, K.; Tatsumisago, M. Evaluation of Elastic Modulus of Li_2S–P_2S_5 Glassy Solid Electrolyte by Ultrasonic Sound Velocity Measurement and Compression Test. *J. Ceram. Soc. Jpn.* **2013**, *121*, 946–949. [CrossRef]
70. McGrogan, F.P.; Swamy, T.; Bishop, S.R.; Eggleton, E.; Porz, L.; Chen, X.; Chiang, Y.; Van Vliet, K.J. Compliant Yet Brittle Mechanical Behavior of Li_2S–P_2S_5 Lithium-Ion-Conducting Solid Electrolyte. *Adv. Energy Mater.* **2017**, *7*, 1602011. [CrossRef]
71. Seino, Y.; Ota, T.; Takada, K.; Hayashi, A.; Tatsumisago, M. A Sulphide Lithium Super Ion Conductor Is Superior to Liquid Ion Conductors for Use in Rechargeable Batteries. *Energy Environ. Sci.* **2014**, *7*, 627–631. [CrossRef]
72. Deng, Z.; Wang, Z.; Chu, I.-H.; Luo, J.; Ong, S.P. Elastic Properties of Alkali Superionic Conductor Electrolytes from First Principles Calculations. *J. Electrochem. Soc.* **2016**, *163*, A67–A74. [CrossRef]
73. Yu, C.; Van Eijck, L.; Ganapathy, S.; Wagemaker, M. Synthesis, Structure and Electrochemical Performance of the Argyrodite Li_6PS_5Cl Solid Electrolyte for Li-Ion Solid State Batteries. *Electrochim. Acta* **2016**, *215*, 93–99. [CrossRef]
74. Song, S.; Shi, C.; Pakhare, A.; Sheldon, B.W.; Guduru, P.R. Investigation of the Mechanical Properties of Porous Argyrodite Sulfide Electrolytes for All-Solid-State Batteries. *ACS Appl. Energy Mater.* **2025**, *8*, 5636–5644. [CrossRef]
75. Wang, Y.; Hao, H.; Naik, K.G.; Vishnugopi, B.S.; Fincher, C.D.; Yan, Q.; Raj, V.; Celio, H.; Yang, G.; Fang, H.; et al. Mechanical Milling—Induced Microstructure Changes in Argyrodite LPSCl Solid-State Electrolyte Critically Affect Electrochemical Stability. *Adv. Energy Mater.* **2024**, *14*, 2304530. [CrossRef]
76. Kamaya, N.; Homma, K.; Yamakawa, Y.; Hirayama, M.; Kanno, R.; Yonemura, M.; Kamiyama, T.; Kato, Y.; Hama, S.; Kawamoto, K.; et al. A Lithium Superionic Conductor. *Nat. Mater.* **2011**, *10*, 682–686. [CrossRef] [PubMed]
77. Wang, Z.Q.; Wu, M.S.; Liu, G.; Lei, X.L.; Xu, B.; Ouyang, C.Y. Elastic Properties of New Solid State Electrolyte Material $Li_{10}GeP_2S_{12}$: A Study from First-Principles Calculations. *Int. J. Electrochem. Sci.* **2014**, *9*, 562–568. [CrossRef]
78. Zhao, J.; Zhao, C.; Zhu, J.; Liu, X.; Yao, J.; Wang, B.; Dai, Q.; Wang, Z.; Chen, J.; Jia, P.; et al. Size-Dependent Chemomechanical Failure of Sulfide Solid Electrolyte Particles during Electrochemical Reaction with Lithium. *Nano Lett.* **2022**, *22*, 411–418. [CrossRef] [PubMed]
79. Kim, H.; Hikima, K.; Watanabe, K.; Matsui, N.; Suzuki, K.; Obokata, S.; Muto, H.; Matsuda, A.; Kanno, R.; Hirayama, M. Mechanical Properties of $Li_{10.35}Ge_{1.35}P_{1.65}S_{12}$ with Different Particle Sizes. *Mater. Trans.* **2024**, *65*, 861–866. [CrossRef]

80. Asano, T.; Sakai, A.; Ouchi, S.; Sakaida, M.; Miyazaki, A.; Hasegawa, S. Solid Halide Electrolytes with High Lithium-Ion Conductivity for Application in 4 V Class Bulk-Type All-Solid-State Batteries. *Adv. Mater.* **2018**, *30*, 1803075. [CrossRef] [PubMed]
81. Andrews, N.L.P.; Fan, J.Z.; Forward, R.L.; Chen, M.C.; Loock, H.-P. Determination of the Thermal, Oxidative and Photochemical Degradation Rates of Scintillator Liquid by Fluorescence EEM Spectroscopy. *Phys. Chem. Chem. Phys.* **2017**, *19*, 73–81. [CrossRef] [PubMed]
82. Liu, Z.; Chien, P.-H.; Wang, S.; Song, S.; Lu, M.; Chen, S.; Xia, S.; Liu, J.; Mo, Y.; Chen, H. Tuning Collective Anion Motion Enables Superionic Conductivity in Solid-State Halide Electrolytes. *Nat. Chem.* **2024**, *16*, 1584–1591. [CrossRef] [PubMed]
83. Li, X.; Liang, J.; Chen, N.; Luo, J.; Adair, K.R.; Wang, C.; Banis, M.N.; Sham, T.; Zhang, L.; Zhao, S.; et al. Water-Mediated Synthesis of a Superionic Halide Solid Electrolyte. *Angew. Chem.* **2019**, *131*, 16579–16584. [CrossRef]
84. Ren, Y.; Sun, C.; Liu, J.; Cai, G.; Tan, X.; Zhang, C. Effect of the Mechanical Strength on the Ion Transport in a Transition Metal Lithium Halide Electrolyte: First-Principle Calculations. *Mater. Today Commun.* **2022**, *33*, 104570. [CrossRef]
85. Farzanian, S.; Vazquez Mercado, J.; Shozib, I.; Sivadas, N.; Lacivita, V.; Wang, Y.; Tu, Q.H. Mechanical Investigations of Composite Cathode Degradation in All-Solid-State Batteries. *ACS Appl. Energy Mater.* **2023**, *6*, 9615–9623. [CrossRef]
86. Park, S.H.; Naik, K.G.; Vishnugopi, B.S.; Xiao, X.; Drakopoulos, M.; Vo, N.T.; Zhong, Z.; Mukherjee, P.P.; Hatzell, K.B. Chemo-Mechanical Behavior and Stability of High-Loading Cathodes in Solid-State Batteries. *ACS Nano* **2025**, *19*, 22262–22269. [CrossRef] [PubMed]
87. Zhang, H.; Chen, Z.; Zhang, X.; Shen, Z.; Xu, F.; Wang, F. Unraveling Plating/Stripping-Induced Strain Evolution via Embedded Sensors for Predictive Failure Mitigation in Solid-State Li Metal Batteries. *Chem. Sci.* **2025**, *16*, 15697–15706. [CrossRef] [PubMed]
88. Xu, H.; Yang, S.; Li, B. Pressure Effects and Countermeasures in Solid-State Batteries: A Comprehensive Review. *Adv. Energy Mater.* **2024**, *14*, 2303539. [CrossRef]
89. Yuan, C.; Wu, J.; Zhang, W.; Han, M.; Jia, Y. Electro-Chemo-Mechanics Interplays Caused by Solid Electrolyte-Lithium Anode Interface Roughness in All-Solid-State Batteries. *J. Energy Chem.* **2025**, *108*, 495–507. [CrossRef]
90. Ahmad, Z.; Yeo, C.-D. Contact Mechanics of Solid-State Batteries. *J. Electrochem. Energy Convers. Storage* **2025**, *23*, 024703. [CrossRef]
91. Zhang, X.; Wang, Q.J.; Harrison, K.L.; Roberts, S.A.; Harris, S.J. Pressure-Driven Interface Evolution in Solid-State Lithium Metal Batteries. *Cell Rep. Phys. Sci.* **2020**, *1*, 100012. [CrossRef]
92. Lewis, J.A.; Cavallaro, K.A.; Liu, Y.; McDowell, M.T. The Promise of Alloy Anodes for Solid-State Batteries. *Joule* **2022**, *6*, 1418–1430. [CrossRef]
93. Tan, D.H.S.; Chen, Y.-T.; Yang, H.; Bao, W.; Sreenarayanan, B.; Doux, J.-M.; Li, W.; Lu, B.; Ham, S.-Y.; Sayahpour, B.; et al. Carbon-Free High-Loading Silicon Anodes Enabled by Sulfide Solid Electrolytes. *Science* **2021**, *373*, 1494–1499. [CrossRef] [PubMed]
94. Liang, J.; Bohnen, M.; Müller, R.; Leiter, R.; Fleischmann, S.; Gong, S.; Soans, M.R.; Passerini, S.; Varzi, A. Stacking Pressure-Driven Interfacial Dynamics in Anode-Free Solid-State Lithium Batteries. *Adv. Sci.* **2026**, *13*, e76888. [CrossRef] [PubMed]
95. Liu, W.; Luo, Y.; Hu, Y.; Chen, Z.; Wang, Q.; Chen, Y.; Iqbal, N.; Mitlin, D. Interrelation Between External Pressure, SEI Structure, and Electrodeposit Morphology in an Anode-Free Lithium Metal Battery. *Adv. Energy Mater.* **2024**, *14*, 2302261. [CrossRef]
96. Xu, G.; Huang, L.; Lu, C.; Zhou, X.; Cui, G. Revealing the Multilevel Thermal Safety of Lithium Batteries. *Energy Storage Mater.* **2020**, *31*, 72–86. [CrossRef]
97. Yuan, J.; Zhang, Y.; Chen, F.; Gu, Z. An Overview of Joule Heating in Energy Storage Materials and Applications. *J. Mater. Chem. C* **2024**, *12*, 14729–14753. [CrossRef]
98. Fleckenstein, M.; Bohlen, O.; Roscher, M.A.; Bäker, B. Current Density and State of Charge Inhomogeneities in Li-Ion Battery Cells with $LiFePO_4$ as Cathode Material Due to Temperature Gradients. *J. Power Sources* **2011**, *196*, 4769–4778. [CrossRef]
99. Kim, J.S.; Bong, S.; Kim, J.; Son, J.P.; Park, J.; Seo, D.H.; Jung, Y.S. Thermal Runaway in Sulfide-Based All-Solid-State Batteries: Risk Landscape, Diagnostic Gaps, and Strategic Directions. *Adv. Energy Mater.* **2025**, *15*, e03593. [CrossRef]
100. Bertrand, M.; Rousselot, S.; Aymé-Perrot, D.; Dollé, M. Compatibility Assessment of Solid Ceramic Electrolytes and Active Materials Based on Thermal Dilatation for the Development of Solid-State Batteries. *Mater. Adv.* **2021**, *2*, 2989–2999. [CrossRef]
101. Hubaud, A.A.; Schroeder, D.J.; Ingram, B.J.; Okasinski, J.S.; Vaughey, J.T. Thermal Expansion in the Garnet-Type Solid Electrolyte $(Li_{7-x}Al_{x/3})La_3Zr_2O_{12}$ as a Function of Al Content. *J. Alloys Compd.* **2015**, *644*, 804–807. [CrossRef]
102. Tobolsky, A.V. Stress Relaxation Studies of the Viscoelastic Properties of Polymers. *J. Appl. Phys.* **1956**, *27*, 673–685. [CrossRef]
103. Huang, L.; Xu, G.; Du, X.; Li, J.; Xie, B.; Liu, H.; Han, P.; Dong, S.; Cui, G.; Chen, L. Uncovering LiH Triggered Thermal Runaway Mechanism of a High-Energy $LiNi_{0.5}Co_{0.2}Mn_{0.3}O_2$/Graphite Pouch Cell. *Adv. Sci.* **2021**, *8*, 2100676. [CrossRef] [PubMed]
104. Liu, X.; Ren, D.; Hsu, H.; Feng, X.; Xu, G.-L.; Zhuang, M.; Gao, H.; Lu, L.; Han, X.; Chu, Z.; et al. Thermal Runaway of Lithium-Ion Batteries without Internal Short Circuit. *Joule* **2018**, *2*, 2047–2064. [CrossRef]
105. Feng, X.; Ouyang, M.; Liu, X.; Lu, L.; Xia, Y.; He, X. Thermal Runaway Mechanism of Lithium Ion Battery for Electric Vehicles: A Review. *Energy Storage Mater.* **2018**, *10*, 246–267. [CrossRef]

106. Zhang, X.; Huang, L.; Xie, B.; Zhang, S.; Jiang, Z.; Xu, G.; Li, J.; Cui, G. Deciphering the Thermal Failure Mechanism of Anode-Free Lithium Metal Pouch Batteries. *Adv. Energy Mater.* **2023**, *13*, 2203648. [CrossRef]
107. Yang, S.-J.; Hu, J.-K.; Jiang, F.-N.; Yuan, H.; Park, H.S.; Huang, J.-Q. Safer Solid-State Lithium Metal Batteries: Mechanisms and Strategies. *InfoMat* **2024**, *6*, e12512. [CrossRef]
108. Conforto, G.; Ruess, R.; Schröder, D.; Trevisanello, E.; Fantin, R.; Richter, F.H.; Janek, J. Editors' Choice—Quantification of the Impact of Chemo-Mechanical Degradation on the Performance and Cycling Stability of NCM-Based Cathodes in Solid-State Li-Ion Batteries. *J. Electrochem. Soc.* **2021**, *168*, 070546. [CrossRef]
109. Zheng, X.; Xue, Z.; Hao, H.; Cho, Y.; Li, Y.; Kim, C.; Czaja, P.; Lee, S.S.; Bone, S.; Spielman-Sun, E.; et al. Unravelling Electro-Chemo-Mechanical Interplay in Layered Oxide Cathode Degradation in Solid-State Batteries. *Sci. Adv.* **2025**, *11*, eady7189. [CrossRef] [PubMed]
110. Cheng, E.J.; Duan, H.; Wang, M.J.; Kazyak, E.; Munakata, H.; Garcia-Mendez, R.; Gao, B.; Huo, H.; Zhang, T.; Chen, F.; et al. Li-Stuffed Garnet Solid Electrolytes: Current Status, Challenges, and Perspectives for Practical Li-Metal Batteries. *Energy Storage Mater.* **2025**, *75*, 103970. [CrossRef]
111. Porz, L.; Swamy, T.; Sheldon, B.W.; Rettenwander, D.; Frömling, T.; Thaman, H.L.; Berendts, S.; Uecker, R.; Carter, W.C.; Chiang, Y. Mechanism of Lithium Metal Penetration through Inorganic Solid Electrolytes. *Adv. Energy Mater.* **2017**, *7*, 1701003. [CrossRef]
112. Kazyak, E.; Garcia-Mendez, R.; LePage, W.S.; Sharafi, A.; Davis, A.L.; Sanchez, A.J.; Chen, K.-H.; Haslam, C.; Sakamoto, J.; Dasgupta, N.P. Li Penetration in Ceramic Solid Electrolytes: Operando Microscopy Analysis of Morphology, Propagation, and Reversibility. *Matter* **2020**, *2*, 1025–1048. [CrossRef]
113. Wang, M.J.; Choudhury, R.; Sakamoto, J. Characterizing the Li-Solid-Electrolyte Interface Dynamics as a Function of Stack Pressure and Current Density. *Joule* **2019**, *3*, 2165–2178. [CrossRef]
114. Krauskopf, T.; Hartmann, H.; Zeier, W.G.; Janek, J. Toward a Fundamental Understanding of the Lithium Metal Anode in Solid-State Batteries—An Electrochemo-Mechanical Study on the Garnet-Type Solid Electrolyte $Li_{6.25}Al_{0.25}La_3Zr_2O_{12}$. *ACS Appl. Mater. Interfaces* **2019**, *11*, 14463–14477. [CrossRef] [PubMed]
115. Yue, F.; Wang, M.; Li, Z.; Huang, X. Strategies toward Addressing Challenges of All-Solid-State Li Metal Batteries Based on Quantitative Interpretation of the Electrochemo-Mechanical Correlation. *Energy Storage Mater.* **2024**, *69*, 103409. [CrossRef]
116. Richman, R.H.; Tennenhouse, G.J. A Model for Degradation of Ceramic Electrolytes in Na-S Batteries. *J. Am. Ceram. Soc.* **1975**, *58*, 63–67. [CrossRef]
117. Urbain, F.; Smirnov, V.; Becker, J.-P.; Lambertz, A.; Yang, F.; Ziegler, J.; Kaiser, B.; Jaegermann, W.; Rau, U.; Finger, F. Chemo-Mechanical Expansion of Lithium Electrode Materials—On the Route to Mechanically Optimized All-Solid-State Batteries. *Energy Environ. Sci.* **2016**, *9*, 145–154. [CrossRef]
118. Shi, T.; Zhang, Y.-Q.; Tu, Q.; Wang, Y.; Scott, M.C.; Ceder, G. Characterization of Mechanical Degradation in an All-Solid-State Battery Cathode. *J. Mater. Chem. A* **2020**, *8*, 17399–17404. [CrossRef]
119. Koerver, R.; Aygün, I.; Leichtweiß, T.; Dietrich, C.; Zhang, W.; Binder, J.O.; Hartmann, P.; Zeier, W.G.; Janek, J. Capacity Fade in Solid-State Batteries: Interphase Formation and Chemomechanical Processes in Nickel-Rich Layered Oxide Cathodes and Lithium Thiophosphate Solid Electrolytes. *Chem. Mater.* **2017**, *29*, 5574–5582. [CrossRef]
120. Liu, C.; Roters, F.; Raabe, D. Role of Grain-Level Chemo-Mechanics in Composite Cathode Degradation of Solid-State Lithium Batteries. *Nat. Commun.* **2024**, *15*, 7970. [CrossRef] [PubMed]
121. Lee, S.; Kim, T.; Kim, K.; Song, G.; Park, J.; Lee, M.; Jung, H.; Park, K.; Choi, S.H.; Song, J.; et al. Mechano-Electrochemical Healing at the Interphase Between $LiNi_{0.8}Co_{0.1}Mn_{0.1}O_2$ and Li_6PS_5Cl in All-Solid-State Batteries. *Adv. Energy Mater.* **2025**, *15*, 2405782. [CrossRef]
122. Kim, K.; Jun, S.; Kim, T.; Kim, J.S.; Lee, S.; Song, G.; Park, J.; Jung, Y.S.; Lee, K.T. Interfacial Degradation Mechanism of Nanostructured $LiCoO_2$ for Li_6PS_5Cl-Based All-Solid-State Batteries. *Chem. Mater.* **2024**, *36*, 5215–5227. [CrossRef]
123. Kasemchainan, J.; Zekoll, S.; Spencer Jolly, D.; Ning, Z.; Hartley, G.O.; Marrow, J.; Bruce, P.G. Critical Stripping Current Leads to Dendrite Formation on Plating in Lithium Anode Solid Electrolyte Cells. *Nat. Mater.* **2019**, *18*, 1105–1111. [CrossRef] [PubMed]
124. Swamy, T.; Park, R.; Sheldon, B.W.; Rettenwander, D.; Porz, L.; Berendts, S.; Uecker, R.; Carter, W.C.; Chiang, Y.-M. Lithium Metal Penetration Induced by Electrodeposition through Solid Electrolytes: Example in Single-Crystal $Li_6La_3ZrTaO_{12}$ Garnet. *J. Electrochem. Soc.* **2018**, *165*, A3648. [CrossRef]
125. Lewis, J.A.; Cortes, F.J.Q.; Boebinger, M.G.; Tippens, J.; Marchese, T.S.; Kondekar, N.; Liu, X.; Chi, M.; McDowell, M.T. Interphase Morphology between a Solid-State Electrolyte and Lithium Controls Cell Failure. *ACS Energy Lett.* **2019**, *4*, 591–599. [CrossRef]
126. Banerjee, A.; Wang, X.; Fang, C.; Wu, E.A.; Meng, Y.S. Interfaces and Interphases in All-Solid-State Batteries with Inorganic Solid Electrolytes. *Chem. Rev.* **2020**, *120*, 6878–6933. [CrossRef] [PubMed]
127. Zhang, W.; Schröder, D.; Arlt, T.; Manke, I.; Koerver, R.; Pinedo, R.; Weber, D.A.; Sann, J.; Zeier, W.G.; Janek, J. (Electro)Chemical Expansion during Cycling: Monitoring the Pressure Changes in Operating Solid-State Lithium Batteries. *J. Mater. Chem. A* **2017**, *5*, 9929–9936. [CrossRef]

128. Bucci, G.; Talamini, B.; Renuka Balakrishna, A.; Chiang, Y.-M.; Carter, W.C. Mechanical Instability of Electrode-Electrolyte Interfaces in Solid-State Batteries. *Phys. Rev. Mater.* **2018**, *2*, 105407. [CrossRef]
129. Rezaei, S.; Asheri, A.; Xu, B.-X. A Consistent Framework for Chemo-Mechanical Cohesive Fracture and Its Application in Solid-State Batteries. *J. Mech. Phys. Solids* **2021**, *157*, 104612. [CrossRef]
130. Yuan, C.; Wu, J.; Zhang, W.; Xu, J. Decoding Electrochemo-Mechanical Degradation in Solid-State Batteries: A Phase-Field Study toward Robust Cathode Design. *Energy Storage Mater.* **2025**, *82*, 104577. [CrossRef]
131. Ning, Z.; Li, G.; Melvin, D.L.R.; Chen, Y.; Bu, J.; Spencer-Jolly, D.; Liu, J.; Hu, B.; Gao, X.; Perera, J.; et al. Dendrite Initiation and Propagation in Lithium Metal Solid-State Batteries. *Nature* **2023**, *618*, 287–293. [CrossRef] [PubMed]
132. Cheng, E.J.; Sharafi, A.; Sakamoto, J. Intergranular Li Metal Propagation through Polycrystalline $Li_{6.25}Al_{0.25}La_3Zr_2O_{12}$ Ceramic Electrolyte. *Electrochim. Acta* **2017**, *223*, 85–91. [CrossRef]
133. Zhang, B.; Yuan, B.; Yan, X.; Han, X.; Zhang, J.; Tan, H.; Wang, C.; Yan, P.; Gao, H.; Liu, Y. Atomic Mechanism of Lithium Dendrite Penetration in Solid Electrolytes. *Nat. Commun.* **2025**, *16*, 1906. [CrossRef] [PubMed]
134. Tippens, J.; Miers, J.C.; Afshar, A.; Lewis, J.A.; Cortes, F.J.Q.; Qiao, H.; Marchese, T.S.; Di Leo, C.V.; Saldana, C.; McDowell, M.T. Visualizing Chemomechanical Degradation of a Solid-State Battery Electrolyte. *ACS Energy Lett.* **2019**, *4*, 1475–1483. [CrossRef]
135. Yildirim, C.; Flatscher, F.; Ganschow, S.; Lassnig, A.; Gammer, C.; Todt, J.; Keckes, J.; Rettenwander, D. Understanding the Origin of Lithium Dendrite Branching in $Li_{6.5}La_3Zr_{1.5}Ta_{0.5}O_{12}$ Solid-State Electrolyte via Microscopy Measurements. *Nat. Commun.* **2024**, *15*, 8207. [CrossRef] [PubMed]
136. Han, F.; Westover, A.S.; Yue, J.; Fan, X.; Wang, F.; Chi, M.; Leonard, D.N.; Dudney, N.J.; Wang, H.; Wang, C. High Electronic Conductivity as the Origin of Lithium Dendrite Formation within Solid Electrolytes. *Nat. Energy* **2019**, *4*, 187–196. [CrossRef]
137. Zhang, Y.; Motahari, S.; Woods, E.V.; Zaefferer, S.; Schweizer, P.; Zhang, Z.; Liu, Y.; Gault, B.; Roters, F.; Raabe, D.; et al. Mechanically Driven Li Dendrite Penetration in Garnet Solid Electrolyte. *Nature* **2026**, *652*, 912–918. [CrossRef] [PubMed]
138. Porz, L.; Knez, D.; Scherer, M.; Ganschow, S.; Kothleitner, G.; Rettenwander, D. Dislocations in Ceramic Electrolytes for Solid-State Li Batteries. *Sci. Rep.* **2021**, *11*, 8949. [CrossRef] [PubMed]
139. Fang, X. Mechanical Tailoring of Dislocations in Ceramics at Room Temperature: A Perspective. *J. Am. Ceram. Soc.* **2024**, *107*, 1425–1447. [CrossRef]
140. Huo, H.; Jiang, M.; Bai, Y.; Ahmed, S.; Volz, K.; Hartmann, H.; Henss, A.; Singh, C.V.; Raabe, D.; Janek, J. Chemo-Mechanical Failure Mechanisms of the Silicon Anode in Solid-State Batteries. *Nat. Mater.* **2024**, *23*, 543–551. [CrossRef] [PubMed]
141. Eckhardt, J.K.; Klar, P.J.; Janek, J.; Heiliger, C. Interplay of Dynamic Constriction and Interface Morphology between Reversible Metal Anode and Solid Electrolyte in Solid State Batteries. *ACS Appl. Mater. Interfaces* **2022**, *14*, 35545–35554. [CrossRef] [PubMed]
142. Vishnugopi, B.S.; Naik, K.G.; Kawakami, H.; Ikeda, N.; Mizuno, Y.; Iwamura, R.; Kotaka, T.; Aotani, K.; Tabuchi, Y.; Mukherjee, P.P. Asymmetric Contact Loss Dynamics during Plating and Stripping in Solid-State Batteries. *Adv. Energy Mater.* **2023**, *13*, 2203671. [CrossRef]
143. Shen, X.; Zhang, R.; Chen, X.; Cheng, X.; Li, X.; Zhang, Q. The Failure of Solid Electrolyte Interphase on Li Metal Anode: Structural Uniformity or Mechanical Strength? *Adv. Energy Mater.* **2020**, *10*, 1903645. [CrossRef]
144. Lu, Y.; Zhao, C.-Z.; Hu, J.-K.; Sun, S.; Yuan, H.; Fu, Z.-H.; Chen, X.; Huang, J.-Q.; Ouyang, M.; Zhang, Q. The Void Formation Behaviors in Working Solid-State Li Metal Batteries. *Sci. Adv.* **2022**, *8*, eadd0510. [CrossRef] [PubMed]
145. Otoyama, M.; Sakuda, A.; Hayashi, A.; Tatsumisago, M. Optical Microscopic Observation of Graphite Composite Negative Electrodes in All-Solid-State Lithium Batteries. *Solid State Ion.* **2018**, *323*, 123–129. [CrossRef]
146. Liu, H.; Jiang, W.; Chen, W.; Lin, Q.; Ren, S.; Su, Y.; Tong, R.; Zhang, Y. Dendrite Growth and Inhibition in All-Solid-State Lithium Metal Batteries: In Situ Optical Observation. *J. Mater. Chem. A* **2024**, *12*, 3575–3579. [CrossRef]
147. Athanasiou, C.E.; Fincher, C.D.; Gilgenbach, C.; Gao, H.; Carter, W.C.; Chiang, Y.-M.; Sheldon, B.W. Operando Measurements of Dendrite-Induced Stresses in Ceramic Electrolytes Using Photoelasticity. *Matter* **2024**, *7*, 95–106. [CrossRef]
148. Yadav, N.G.; Folastre, N.; Bolmont, M.; Jamali, A.; Morcrette, M.; Davoisne, C. Study of Failure Modes in Two Sulphide-Based Solid Electrolyte All-Solid-State Batteries via in Situ SEM. *J. Mater. Chem. A* **2022**, *10*, 17142–17155. [CrossRef]
149. Zhao, L.; Feng, M.; Wu, C.; Guo, L.; Chen, Z.; Risal, S.; Ai, Q.; Lou, J.; Fan, Z.; Qi, Y.; et al. Imaging the Evolution of Lithium-Solid Electrolyte Interface Using Operando Scanning Electron Microscopy. *Nat. Commun.* **2025**, *16*, 4283. [CrossRef] [PubMed]
150. Nagao, M.; Hayashi, A.; Tatsumisago, M.; Kanetsuku, T.; Tsuda, T.; Kuwabata, S. In Situ SEM Study of a Lithium Deposition and Dissolution Mechanism in a Bulk-Type Solid-State Cell with a Li_2S–P_2S_5 Solid Electrolyte. *Phys. Chem. Chem. Phys.* **2013**, *15*, 18600. [CrossRef] [PubMed]
151. Liu, X.; Zheng, B.; Zhao, J.; Zhao, W.; Liang, Z.; Su, Y.; Xie, C.; Zhou, K.; Xiang, Y.; Zhu, J.; et al. Electrochemo-Mechanical Effects on Structural Integrity of Ni-Rich Cathodes with Different Microstructures in All Solid-State Batteries. *Adv. Energy Mater.* **2021**, *11*, 2003583. [CrossRef]
152. Cao, D.; Zhang, K.; Li, W.; Zhang, Y.; Ji, T.; Zhao, X.; Cakmak, E.; Zhu, J.; Cao, Y.; Zhu, H. Nondestructively Visualizing and Understanding the Mechano-Electro-chemical Origins of "Soft Short" and "Creeping" in All-Solid-State Batteries. *Adv. Funct. Mater.* **2023**, *33*, 2307998. [CrossRef]

153. Huang, C.-J.; Oh, J.A.S.; Vicencio, M.; Hu, T.; Yang, H.; Burrow, J.N.; Song, Y.-F.; Yin, G.-C.; Shevchenko, P.; Wiaderek, K.M.; et al. X-Ray Micro-Computed Tomography for Structural Analysis of All-Solid-State Battery at Pouch Cell Level. *ACS Energy Lett.* **2025**, *10*, 3459–3470. [CrossRef] [PubMed]
154. Fathiannasab, H.; Ghorbani Kashkooli, A.; Li, T.; Zhu, L.; Chen, Z. Three-Dimensional Modeling of All-Solid-State Lithium-Ion Batteries Using Synchrotron Transmission X-Ray Microscopy Tomography. *J. Electrochem. Soc.* **2020**, *167*, 100558. [CrossRef]
155. Dixit, M.B.; Park, J.-S.; Kenesei, P.; Almer, J.; Hatzell, K.B. Status and Prospect of in Situ and *Operando* Characterization of Solid-State Batteries. *Energy Environ. Sci.* **2021**, *14*, 4672–4711. [CrossRef]
156. Ishiguro, N.; Totsuka, T.; Uematsu, H.; Sekizawa, O.; Yamamoto, K.; Iriyama, Y.; Takahashi, Y. Comprehensive Operando Visualization of the Electrochemical Events in the Cathode/Anode Layers in Thin-Film-Type All-Solid-State Lithium-Ion Batteries. *ACS Appl. Energy Mater.* **2023**, *6*, 8306–8315. [CrossRef]
157. Cao, D.; Zhang, Y.; Ji, T.; Zhu, H. In Operando Neutron Imaging Characterizations of All-Solid-State Batteries. *MRS Bull.* **2023**, *48*, 1257–1268. [CrossRef]
158. Liang, S.; Sun, Y.; Cheng, Y.; Roth, S.V.; Müller-Buschbaum, P.; Cao, L.; Peng, J.; Wang, S.; Sun, X.; Wang, C. Probing All-Solid-State Batteries with Real-Time Synchrotron and Neutron Techniques. *Adv. Energy Mater.* **2026**, *16*, e04045. [CrossRef]
159. Rao, R.P.; Sharma, N.; Peterson, V.K.; Adams, S. Formation and Conductivity Studies of Lithium Argyrodite Solid Electrolytes Using In-Situ Neutron Diffraction. *Solid State Ion.* **2013**, *230*, 72–76. [CrossRef]
160. Gao, L.; Pan, J.; Di, L.; Zhu, J.; Wang, L.; Gao, S.; Zou, R.; Kang, L.; Han, S.; Zhao, Y. Neutron Diffraction for Revealing the Structures and Ionic Transport Mechanisms of Antiperovskite Solid Electrolytes. *Chin. J. Struct. Chem.* **2023**, *42*, 100048. [CrossRef]
161. Bak, S.-M.; Shadike, Z.; Lin, R.; Yu, X.; Yang, X.-Q. In Situ/Operando Synchrotron-Based X-Ray Techniques for Lithium-Ion Battery Research. *NPG Asia Mater.* **2018**, *10*, 563–580. [CrossRef]
162. Cao, D.; Sun, X.; Li, F.; Bak, S.; Ji, T.; Geiwitz, M.; Burch, K.S.; Du, Y.; Yang, G.; Zhu, H. Understanding Electrochemical Reaction Mechanisms of Sulfur in All-Solid-State Batteries through Operando and Theoretical Studies. *Angew. Chem. Int. Ed.* **2023**, *62*, e202302363. [CrossRef] [PubMed]
163. Otoyama, M.; Ito, Y.; Hayashi, A.; Tatsumisago, M. Raman Imaging for $LiCoO_2$ Composite Positive Electrodes in All-Solid-State Lithium Batteries Using Li_2S–P_2S_5 Solid Electrolytes. *J. Power Sources* **2016**, *302*, 419–425. [CrossRef]
164. Ahmed, R.A.; Ebechidi, N.; Reisya, I.; Orisekeh, K.; Huda, A.; Bello, A.; Oyewole, O.K.; Soboyejo, W.O. Pressure-Induced Interfacial Contacts and the Deformation in All Solid-State Li-Ion Batteries. *J. Power Sources* **2022**, *521*, 230939. [CrossRef]
165. Otoyama, M.; Terasaki, N.; Takeuchi, T.; Okumura, T.; Kuratani, K. Visualization of Local Strain Distributions in All-Solid-State Batteries with Silicon Negative Electrodes Using Digital Image Correlation for Operando/In Situ Microscopy Images. *ChemElectroChem* **2025**, *12*, e202400616. [CrossRef]
166. Albero Blanquer, L.; Marchini, F.; Seitz, J.R.; Daher, N.; Bétermier, F.; Huang, J.; Gervillié, C.; Tarascon, J.-M. Optical Sensors for Operando Stress Monitoring in Lithium-Based Batteries Containing Solid-State or Liquid Electrolytes. *Nat. Commun.* **2022**, *13*, 1153. [CrossRef] [PubMed]
167. Lee, C.; Kim, J.Y.; Bae, K.Y.; Kim, T.; Jung, S.-J.; Son, S.; Lee, H.-W. Enhancing Electrochemomechanics: How Stack Pressure Regulation Affects All-Solid-State Batteries. *Energy Storage Mater.* **2024**, *66*, 103196. [CrossRef]
168. Wan, J.; Song, Y.-X.; Chen, W.-P.; Guo, H.-J.; Shi, Y.; Guo, Y.-J.; Shi, J.-L.; Guo, Y.-G.; Jia, F.-F.; Wang, F.-Y.; et al. Micromechanism in All-Solid-State Alloy-Metal Batteries: Regulating Homogeneous Lithium Precipitation and Flexible Solid Electrolyte Interphase Evolution. *J. Am. Chem. Soc.* **2021**, *143*, 839–848. [CrossRef] [PubMed]
169. Papakyriakou, M.; Lu, M.; Liu, Y.; Liu, Z.; Chen, H.; McDowell, M.T.; Xia, S. Mechanical Behavior of Inorganic Lithium-Conducting Solid Electrolytes. *J. Power Sources* **2021**, *516*, 230672. [CrossRef]
170. Sheng, O.; Zheng, J.; Ju, Z.; Jin, C.; Wang, Y.; Chen, M.; Nai, J.; Liu, T.; Zhang, W.; Liu, Y.; et al. In Situ Construction of a LiF-Enriched Interface for Stable All-Solid-State Batteries and Its Origin Revealed by Cryo-TEM. *Adv. Mater.* **2020**, *32*, 2000223. [CrossRef] [PubMed]
171. Liu, Y.; Ju, Z.; Zhang, B.; Wang, Y.; Nai, J.; Liu, T.; Tao, X. Visualizing the Sensitive Lithium with Atomic Precision: Cryogenic Electron Microscopy for Batteries. *Acc. Chem. Res.* **2021**, *54*, 2088–2099. [CrossRef] [PubMed]
172. Minnmann, P.; Schubert, J.; Kremer, S.; Rekers, R.; Burkhardt, S.; Ruess, R.; Bielefeld, A.; Richter, F.H.; Janek, J. Editors' Choice—Visualizing the Impact of the Composite Cathode Microstructure and Porosity on Solid-State Battery Performance. *J. Electrochem. Soc.* **2024**, *171*, 060514. [CrossRef]
173. Jeong, M.; Naik, K.G.; Zheng, Y.; Suk, W.J.; Vishnugopi, B.S.; Lin, L.; Puthusseri, D.; Chuang, A.C.; Okasinski, J.S.; Sakamoto, J.; et al. Operando Investigation on the Role of Densification and Chemo-Mechanics on Solid-State Cathodes. *Adv. Energy Mater.* **2024**, *14*, 2304544. [CrossRef]
174. Sharma, S.; Santiago, A.; Martinez-Ibañez, M.; Gerard, M.; Kumar, A.S.; De Castro, O.; Wirtz, T.; Eswara, S. Operando Visualization of Li Distribution in Solid-State Batteries Using Focused Ion Beam-Secondary Ion Mass Spectrometry Imaging. *Electrochim. Acta* **2025**, *536*, 146728. [CrossRef]

175. Xu, L.; Le Houx, J.; Kachkanov, V.; Zhang, J.; Wullich, R.N.; Fankhauser, M.; Löffel, K.; Schmidt, T.J.; El Kazzi, M. Operando X-Ray Computed Tomography Reveals the Role of Interfacial Nucleation Nanolayers in Suppressing Mechanical Failure in Zero-Excess Lithium All-Solid-State Batteries. *Small* **2026**, *22*, e12284. [CrossRef] [PubMed]
176. Duan, J.; Fuchs, T.; Mogwitz, B.; Minnmann, P.; Zuo, T.-T.; Henss, A.; Janek, J. Solid Electrolyte Cracking Due to Lithium Filament Growth and Concept of Mechanical Reinforcement—An Operando Study. *Mater. Today* **2023**, *70*, 33–43. [CrossRef]
177. Gao, H.; Ai, X.; Wang, H.; Li, W.; Wei, P.; Cheng, Y.; Gui, S.; Yang, H.; Yang, Y.; Wang, M.-S. Visualizing the Failure of Solid Electrolyte under GPa-Level Interface Stress Induced by Lithium Eruption. *Nat. Commun.* **2022**, *13*, 5050. [CrossRef] [PubMed]
178. Kazyak, E.; Wang, M.J.; Lee, K.; Yadavalli, S.; Sanchez, A.J.; Thouless, M.D.; Sakamoto, J.; Dasgupta, N.P. Understanding the Electro-Chemo-Mechanics of Li Plating in Anode-Free Solid-State Batteries with Operando 3D Microscopy. *Matter* **2022**, *5*, 3912–3934. [CrossRef]
179. Sadd, M.; Xiong, S.; Bowen, J.R.; Marone, F.; Matic, A. Investigating Microstructure Evolution of Lithium Metal during Plating and Stripping via Operando X-Ray Tomographic Microscopy. *Nat. Commun.* **2023**, *14*, 854. [CrossRef] [PubMed]
180. Han, S.Y.; Lee, C.; Lewis, J.A.; Yeh, D.; Liu, Y.; Lee, H.-W.; McDowell, M.T. Stress Evolution during Cycling of Alloy-Anode Solid-State Batteries. *Joule* **2021**, *5*, 2450–2465. [CrossRef]
181. Cho, J.H.; Kim, K.; Chakravarthy, S.; Xiao, X.; Rupp, J.L.M.; Sheldon, B.W. An Investigation of Chemo-Mechanical Phenomena and Li Metal Penetration in All-Solid-State Lithium Metal Batteries Using In Situ Optical Curvature Measurements. *Adv. Energy Mater.* **2022**, *12*, 2200369. [CrossRef]
182. Cheng, E.J.; Oyama, R.; Abe, T.; Kanamura, K. High-Voltage All-Solid-State Lithium Metal Batteries Prepared by Aerosol Deposition. *J. Eur. Ceram. Soc.* **2023**, *43*, 2033–2038. [CrossRef]
183. Jiang, H.; Xu, X.; Guo, Q.; Wang, H.; Zheng, J.; Zhu, Y.; Jiang, H.; Kapitanova, O.O.; Volkov, V.S.; Wang, J.; et al. Electro-Chemo-Mechanical Design of Polymer Matrix in Composited $LiNi_{0.8}Co_{0.1}Mn_{0.1}O_2$ Cathode Endows Solid-State Batteries with Superior Performance. *J. Energy Chem.* **2023**, *78*, 277–282. [CrossRef]
184. Oh, H.; Jeong, U.; Choi, J.; Lim, J.; Kim, J.T.; Shin, H.-J.; Im, J.; Gong, H.-W.; Ahn, J.-P.; Lee, Y.M.; et al. Bimodal Composite Cathodes Advancing the Chemo-Mechanical Integrity and Kinetics for All-Solid-State Batteries. *ACS Energy Lett.* **2026**, *11*, 2103–2114. [CrossRef]
185. Moradi, S.; Zahiri, B.; Braun, P.V. Cathode Chemomechanics Controls Li Metal Solid-State Battery Performance under Low Stack Pressures. *Nat. Commun.* **2025**, *16*, 9266. [CrossRef] [PubMed]
186. Hu, Z.; Gao, P.; Ju, S.; Li, Y.; Zhang, T.; Lu, C.; Huang, T.; Liu, P.; Lv, Y.; Guo, M.; et al. Dynamic Volume Compensation Realizing Ah-Level All-Solid-State Silicon-Sulfur Batteries. *Nat. Commun.* **2025**, *16*, 3979. [CrossRef] [PubMed]
187. Sharafi, A.; Kazyak, E.; Davis, A.L.; Yu, S.; Thompson, T.; Siegel, D.J.; Dasgupta, N.P.; Sakamoto, J. Surface Chemistry Mechanism of Ultra-Low Interfacial Resistance in the Solid-State Electrolyte $Li_7La_3Zr_2O_{12}$. *Chem. Mater.* **2017**, *29*, 7961–7968. [CrossRef]
188. Nie, B.; Lee, S.W.; Wang, T.-W.; Liu, T.; Li, J.; Sun, H. Unveiling Multifunctional Synthetic Boundaries for Enhanced Mechanical and Electrochemical Performance in Densified Thick Composite Electrodes. *Nat. Commun.* **2025**, *16*, 9489. [CrossRef] [PubMed]
189. Yu, Z.; Gan, C.; Song, S.; Guduru, P.; Kim, K.-S.; Sheldon, B.W. Dendrite Suppression in Garnet Electrolytes via Thermally Induced Compressive Stress. *Joule* **2026**, *10*, 102232. [CrossRef]
190. Shi, K.; Wan, Z.; Yang, L.; Zhang, Y.; Huang, Y.; Su, S.; Xia, H.; Jiang, K.; Shen, L.; Hu, Y.; et al. In Situ Construction of an Ultra-Stable Conductive Composite Interface for High-Voltage All-Solid-State Lithium Metal Batteries. *Angew. Chem.* **2020**, *132*, 11882–11886. [CrossRef]
191. Fu, K.; Gong, Y.; Liu, B.; Zhu, Y.; Xu, S.; Yao, Y.; Luo, W.; Wang, C.; Lacey, S.D.; Dai, J.; et al. Toward Garnet Electrolyte–Based Li Metal Batteries: An Ultrathin, Highly Effective, Artificial Solid-State Electrolyte/Metallic Li Interface. *Sci. Adv.* **2017**, *3*, e1601659. [CrossRef] [PubMed]
192. Becker, J.; Schuster, L.; Kremer, S.; Fuchs, T.; Janek, J. Microstructure of Electrodeposited Lithium and Its Evolution during Cycling When Using Metal Interlayers in "Anode-Free" Solid-State Batteries. *Energy Environ. Sci.* **2026**, *19*, 2367–2380. [CrossRef]
193. Cheng, E.J.; Shoji, M.; Abe, T.; Kanamura, K. Ionic Liquid-Containing Cathodes Empowering Ceramic Solid Electrolytes. *iScience* **2022**, *25*, 103896. [CrossRef] [PubMed]
194. Ye, Y.; Zhu, X.; Meng, N.; Lian, F. Largely Promoted Mechano-Electrochemical Coupling Properties of Solid Polymer Electrolytes by Introducing Hydrogen Bonds-Rich Network. *Adv. Funct. Mater.* **2023**, *33*, 2307045. [CrossRef]
195. Lei, W.; Jiao, X.; Yang, S.; Ajdari, F.B.; Salavati-Niasari, M.; Feng, Y.; Yin, J.; Ungar, G.; Song, J. Temperature and Stress-Resistant Solid State Electrolyte for Stable Lithium-Metal Batteries. *Energy Storage Mater.* **2022**, *49*, 502–508. [CrossRef]
196. Wang, X.; Zeng, W.; Hong, L.; Xu, W.; Yang, H.; Wang, F.; Duan, H.; Tang, M.; Jiang, H. Stress-Driven Lithium Dendrite Growth Mechanism and Dendrite Mitigation by Electroplating on Soft Substrates. *Nat. Energy* **2018**, *3*, 227–235. [CrossRef]
197. Kwon, Y.H.; Woo, S.; Jung, H.; Yu, H.K.; Kim, K.; Oh, B.H.; Ahn, S.; Lee, S.; Song, S.; Cho, J.; et al. Cable-Type Flexible Lithium Ion Battery Based on Hollow Multi-Helix Electrodes. *Adv. Mater.* **2012**, *24*, 5192–5197. [CrossRef] [PubMed]
198. Bao, Y.; Liu, H.; Zhao, Z.; Ma, X.; Zhang, X.; Liu, G.; Song, W. Toward Flexible Embodied Energy: Scale-Inspired Overlapping Lithium-Ion Batteries with High-Energy-Density and Variable Stiffness. *Adv. Funct. Mater.* **2023**, *33*, 2301581. [CrossRef]

199. Weng, W.; Sun, Q.; Zhang, Y.; He, S.; Wu, Q.; Deng, J.; Fang, X.; Guan, G.; Ren, J.; Peng, H. A Gum-Like Lithium-Ion Battery Based on a Novel Arched Structure. *Adv. Mater.* **2015**, *27*, 1363–1369. [CrossRef] [PubMed]
200. Gao, C.; Ma, J.; Li, W.; Qiu, J.; Wang, S. Structure Engineering-Enabled Multi-Direction-Reconfigurable, Soft, Rechargeable Lithium-Ion Battery with Tissue-Compliance Low Modulus and High Performance. *Energy Storage Mater.* **2023**, *63*, 103031. [CrossRef]
201. Wei, J.; Deebansok, S.; He, X.; Wang, Q.; Waritanant, T.; Geng, Z.; Li, Y.; Gautam, M.; Luo, G.; Zhang, Y.; et al. 3D Printing in Lithium Battery Manufacturing: Opportunities, Challenges, and Perspectives. *Mater. Sci. Eng. R Rep.* **2026**, *170*, 101211. [CrossRef]
202. Butler, K.T.; Davies, D.W.; Cartwright, H.; Isayev, O.; Walsh, A. Machine Learning for Molecular and Materials Science. *Nature* **2018**, *559*, 547–555. [CrossRef] [PubMed]
203. Wang, A.Y.-T.; Murdock, R.J.; Kauwe, S.K.; Oliynyk, A.O.; Gurlo, A.; Brgoch, J.; Persson, K.A.; Sparks, T.D. Machine Learning for Materials Scientists: An Introductory Guide toward Best Practices. *Chem. Mater.* **2020**, *32*, 4954–4965. [CrossRef]
204. Cheng, E.J.; Hong, M.; Zeng, Z.; Liu, C.; Wang, Q.; Jane, M.; Badilita, V.; Costa, C.M.; Lanceros-Méndez, S.; Li, Y.; et al. Breaking Bottlenecks in Solid Electrolyte Discovery with Large Artificial Intelligence Models. *arXiv* **2026**. [CrossRef]
205. Lombardo, T.; Duquesnoy, M.; El-Bouysidy, H.; Årén, F.; Gallo-Bueno, A.; Jørgensen, P.B.; Bhowmik, A.; Demortière, A.; Ayerbe, E.; Alcaide, F.; et al. Artificial Intelligence Applied to Battery Research: Hype or Reality? *Chem. Rev.* **2022**, *122*, 10899–10969. [CrossRef] [PubMed]
206. Hu, Q.; Lu, J.; Hui, J.; Rao, Z.; Ren, Y.; Wang, H. Artificial Intelligence-Driven Development in Rechargeable Battery Materials: Progress, Challenges, and Future Perspectives. *Adv. Funct. Mater.* **2025**, *35*, e08438. [CrossRef]
207. Zhang, H.; Xu, X.; Li, X.-L.; Gao, X. Applications of Generative Artificial Intelligence in Battery Research: Current Status and Prospects. *Acta Phys.-Chim. Sin.* **2025**, *41*, 100115. [CrossRef]
208. Wu, J.; Yao, R.; Wang, K.; Sun, Z.; Wang, J.; Wang, Y.; Hu, J.; Xiong, S. Prior-Knowledge-Driven Machine Learning Modeling for Electro-Chemo-Mechanical Failure of Solid-State Electrolyte. *J. Energy Chem.* **2025**, *111*, 119–128. [CrossRef]
209. Wang, Z.; Zeier, W.G.; You, F. Toward AI Ecosystems for Electrolyte and Interface Engineering in Solid-State Batteries. *Sci. Adv.* **2025**, *11*, eaea0638. [CrossRef] [PubMed]
210. Liu, C.; Liu, X.; Sun, C. Progress on Halide Solid State Electrolytes: Structural Regulation, Interfacial Engineering, and Machine Learning Driven Paradigms. *ACS Energy Lett.* **2026**, *11*, 6142–6165. [CrossRef]
211. Niu, C.; Liu, D.; Lochala, J.A.; Anderson, C.S.; Cao, X.; Gross, M.E.; Xu, W.; Zhang, J.-G.; Whittingham, M.S.; Xiao, J.; et al. Balancing Interfacial Reactions to Achieve Long Cycle Life in High-Energy Lithium Metal Batteries. *Nat. Energy* **2021**, *6*, 723–732. [CrossRef]
212. Ahmad, Z.; Xie, T.; Maheshwari, C.; Grossman, J.C.; Viswanathan, V. Machine Learning Enabled Computational Screening of Inorganic Solid Electrolytes for Suppression of Dendrite Formation in Lithium Metal Anodes. *ACS Cent. Sci.* **2018**, *4*, 996–1006. [CrossRef] [PubMed]
213. Choi, E.; Jo, J.; Kim, W.; Min, K. Searching for Mechanically Superior Solid-State Electrolytes in Li-Ion Batteries via Data-Driven Approaches. *ACS Appl. Mater. Interfaces* **2021**, *13*, 42590–42597. [CrossRef] [PubMed]
214. Hu, T.; Xu, L.; Dai, F.; Zhou, G.; Fu, F.; Wang, X.; Li, L.; Ai, X.; Xu, S. Impact of Amorphous LiF Coating Layers on Cathode-Electrolyte Interfaces in Solid-State Batteries. *Adv. Funct. Mater.* **2024**, *34*, 2402993. [CrossRef]
215. Zhu, J.; Fang, R.; Jiao, J.; Peng, K.; Ihuaenyi, R.C.; Bazant, M.Z.; Li, W. (Invited) Revisiting Electrochemical Methods with Electro-Chemo-Mechanical Coupling and AI. *ECS Meet. Abstr.* **2026**, *MA2026-01*, 133. [CrossRef]
216. Merchant, A.; Batzner, S.; Schoenholz, S.S.; Aykol, M.; Cheon, G.; Cubuk, E.D. Scaling Deep Learning for Materials Discovery. *Nature* **2023**, *624*, 80–85. [CrossRef] [PubMed]
217. Szymanski, N.J.; Rendy, B.; Fei, Y.; Kumar, R.E.; He, T.; Milsted, D.; McDermott, M.J.; Gallant, M.; Cubuk, E.D.; Merchant, A.; et al. An Autonomous Laboratory for the Accelerated Synthesis of Inorganic Materials. *Nature* **2023**, *624*, 86–91. [CrossRef] [PubMed]
218. Zeni, C.; Pinsler, R.; Zügner, D.; Fowler, A.; Horton, M.; Fu, X.; Wang, Z.; Shysheya, A.; Crabbé, J.; Ueda, S.; et al. A Generative Model for Inorganic Materials Design. *Nature* **2025**, *639*, 624–632. [CrossRef] [PubMed]

Disclaimer/Publisher's Note: The statements, opinions and data contained in all publications are solely those of the individual author(s) and contributor(s) and not of MDPI and/or the editor(s). MDPI and/or the editor(s) disclaim responsibility for any injury to people or property resulting from any ideas, methods, instructions or products referred to in the content.